CutFEM for EEG and MEG source analysis and optimized multi-channel transcranial direct current stimulation

Inauguraldissertation zur Erlangung des Doktorgrades der
Naturwissenschaften
- Dr. rer. nat. -
im Fachbereich Mathematik und Informatik der
Mathematisch-Naturwissenschaftlichen Fakultät der Universität Münster
als interdisziplinäre Promotion in Zusammenarbeit mit der Medizinischen
Fakultät

vorgelegt von :

Tim-René Erdbrügger
aus Bielefeld

Münster, 2024

Dekan:	Prof. Dr. Arthur Bartels
Erstgutachter:	Prof. Dr. Christian Engwer
Zweitgutachter:	Prof. Dr. Carsten H. Wolters
Drittgutachter:	PD Dr. med. Stefan Rampp
Tag der mündlichen Prüfung:	
Tag der Promotion:	

Abstract

The accurate estimation of the generators of neural signals measured by electro- and magnetoencephalography (EEG/MEG) data and the subsequent electric stimulation of these generators are critical for many medical and scientific applications. This estimation, or source analysis, basically consists of two parts, a forward and an inverse problem. In the EEG/MEG forward problem, a current source is placed into the brain and the resulting electric potentials and magnetic fields at the sensors are computed. A solution to the inverse problem determines the source configuration that matches the measured data. In transcranial electric stimulation, we are interested in an electrode configuration that injects an optimal current into a target within the brain.

The forward problem requires knowledge of the volume conduction effects in the human head. It can be solved using finite element methods (FEM). This thesis focuses on a finite element approach called CutFEM. Cut-FEM is intended to facilitate the transition from an MRI-based segmentation to a computational mesh. In the first half of this thesis, we present Cut-FEM, its integration into EEG/MEG and tDCS, and analyze its performance in simplified spherical models. CutFEM yields accurate results compared against (quasi-)analytical solutions and outperforms other finite element approaches.

The second part focuses on applying CutFEM-based forward solutions to realistic data sets in both a somatosensory group study of n = 19 subjects and two epilepsy patients who have several anatomical deviations, making their forward modeling particularly challenging. Forward solutions based on established competing methods are computed for comparison. In the group study, CutFEM shows preferable results concerning fit to the measured data, proximity to a source estimation based on an anatomical atlas, and sensitivity to quasi-radial source contributions.

For the epilepsy patients, we find large differences between different forward models. Again, we observe a heightened sensitivity to quasi-radial source orientations in realistic forward models.

One of the patients proceeded with multi-channel optimized transcranial direct current stimulation based on forward modeling with a classical finite element approach. We found trends in seizure reduction and modification of interictal activity.

Acknowledgements

I would like to thank all the people who helped me in creating this thesis over the past years:

Contents

List of Figures

List of Tables

Chapter 1

Introduction

Electroencephalography (EEG) and magnetoencephalography (MEG) have become widespread tools for the non-invasive measurement of human brain activity (Michel and Murray, 2012). Their greatest strength is their high temporal resolution. Both modalities feature sensors located outside the head, either directly on the scalp or surrounding it. These sensors measure the change in electric potential and magnetic field induced by active neurons. Their sampling rate allows the detection of changes in the range of less than a millisecond.

However, compared to modalities such as functional magnetic resonance imaging (fMRI), their spatial resolution, i.e. the reconstruction of which neural source is active, can be challenging. This can be due to low signal strength, uncertainties about the volume conduction properties, and the overlap of an unknown number of simultaneously active sources, and noise artefacts in the data (Puce and Hämäläinen, 2017).

Still, EEG/MEG source reconstruction is an active research area and recent studies have shown that it may add valuable information for applications such as epilepsy diagnosis and surgery (Rampp et al., 2019).

Another application for EEG/MEG source reconstruction is the target definition for transcranial electric stimulation (TES). In TES, one places stimulation electrodes onto the scalp and injects an electric current aimed at either exciting or inhibiting neural activity at a pre-determined location. The placement of these electrodes can be performed in a normalized way, based primarily on anatomical information. Alternatively, personalized stimulation montages can be created. A target within the brain can be identified, for example through EEG/MEG source reconstruction, f-MRI, or other modalities. An optimization over possible electrode placement and injection patterns is performed to reach the maximal stimulation strength that can also take the direction of current flow into account (Dmochowski et al., 2011; Khan et al., 2019).

These are the principal topics for this thesis, EEG/MEG source reconstruction and optimized transcranial electric stimulation using direct current (tDCS). More precisely, our focus is the mathematical aspects of forward modeling. In EEG/MEG, forward modeling refers to placing a hypothetical neural source into an electric volume conductor model of the human head and simulating the signals that the sensors would measure given this source. Inverse modeling then refers to the identification of a set of forward simulated sources that best matches measured sensor data. Forward and inverse problem together form the process of source analysis (Mosher, Leahy, and Lewis, 1999b).

In tDCS, one can similarly first forward simulate the current density based on hypothetical stimulation electrodes and then optimize for a specific target.

Whether it is forward modeling for EEG, MEG, or tDCS, all three require the solution of a partial differential equation (PDE). We will describe how to derive these equations in Chapter 2. In Chapter 3, we then focus on how to solve these PDEs using the finite element method (FEM). In the fourth chapter, we introduce the main addition of this thesis, the cut finite element method (CutFEM) to MEG and tDCS. It is based on level sets as tissue surfaces, and splits the mesh generation necessary for FEM into two parts, thus allowing for a more accurate representation of challenging anatomical details than other meshing approaches. For EEG, a CutFEM implementation was first described in Nüßing, 2018; Erdbrügger et al., 2023, an MEG implementation has been described in Erdbrügger et al., 2024. How to create the level sets necessary for CutFEM is part of Chapter 5, where we also describe the pipeline used for the creation of other forward solutions used throughout this thesis.

In the second part of this thesis, we want to apply CutFEM and compare it to other forward modeling approaches, starting with multi-layered sphere scenarios in Chapter 6. Here, (quasi-)analytical solutions are available as references, giving us clear feedback about the accuracy of the correctness of the forward models. Moving to more realistic geometries in Chapter 7, we analyze an n = 19 group study of somatosensory evoked potentials and fields. Without analytical solutions, we turn to metrics such as residual variance, proximity to an anatomical atlas-based reference, and sensitivity profiles to varying source orientations to assess the reliability of our source reconstructions.

The remaining two chapters focus on the source estimation and subsequent electric stimulation of two epileptic patients. Both subjects are challenging in terms of forward modeling due to anatomical defects such as cranial, surgical resection areas, and liquor-filled cysts.

Reconstruction results and optimized tDCS-caps are presented in Chapter 9. Chapter 10 focuses on the stimulation outcome of a two-week tDCS stimulation of one of the two patients.

Chapter 2

Neurophysiological Background and Mathematical Modeling

In this chapter, we give a short introduction to the electric fields generated by neural activity, how to measure them using Electro- and Magnetoencephalography (EEG/MEG), and how they can be modulated by transcranial stimulation. As stated in the introduction, one focus of this thesis is to identify the parts of the brain responsible for the measured signals. For this source reconstruction, we need to model the volume conduction in the human head, derived from the Maxwell equations as a partial differential equation (PDE).

Transcranial direct current stimulation (tDCS) is a closely related task. In EEG we measure a signal at the scalp and then reconstruct its generators, whereas in tDCS we use superficial electrodes to stimulate these generators. Optimizing the positioning of the electrodes to maximize the stimulation effect in a specific region again requires knowledge of the heads conductive properties, solving a PDE.

EEG/MEG measurements and tDCS stimulation are both safe, non-invasive, and, except for the MEG, cheap to conduct, making them ideal methods for both scientific and clinical applications.

2.1 Electromagnetic activity of the brain

The human brain consists of two types of cells. Approximately 100 billion Neurons transmit signals, and ten times as many glial cells provide support for the neurons (Herculano-Houzel, 2009). Neurons have three main parts: Dendrites, Axons, and the cell body, the soma (Kirschstein and Köhling, 2009). Dendrites receive incoming signals and relay them to the soma, where it is summated and, given sufficient strength, transmitted along the axon to other neurons.

Action potential and postsynaptic potential

At rest, there is a resting potential of -70 mV along the neuron's membrane measured against the extracellular space surrounding it. It is maintained by the presence of charged ions, potassium inside, and sodium outside. Potassium can freely pass the membrane to enter from extracellular space to the axon, but it cannot leave the axon. Sodium on the other hand is actively carried out of the axon, leading to chemical concentration gradients along the

membrane. If the membrane is sufficiently depolarized by an incoming signal from the soma, voltage-gated channels open to allow the influx of sodium into the neuron leading to a polarity reversal. The sodium channels close on their own while potassium channels open, leading to the outflow of potassium and repolarization of the membrane. In the absence of chemical gradients, the axon is insensitive to a renewed depolarization until a potassium-sodium pump restores the gradient. The entire process takes less than 2 ms time.

A second type of potential is induced where dendrites connect to other neurons, forming synapses. A signal, often an action potential, passing through a synapse to (the postsynaptic) dendrite is characterized by the influx of either positively or negatively charged ions that then lead to a current inside the dendrite moving away from the synapse and leading to an extracellular return current of ions with opposite polarity. If the inflowing ions have a positive charge, the dendrite is depolarized and by extension also the soma, possibly leading to an action potential along the axon. A negative inflow hyperpolarizes the postsynaptic dendrites and thus inhibits signal propagation. Postsynaptic potentials last for a duration of multiple milliseconds.

Generators of EEG and MEG

The question to which extent each kind of neural activity contributes to the EEG and MEG is difficult to answer and still open to debate (Thio and Grill, 2023). A single potential of a single neuron is too weak to be picked up by extracranial sensors. While action potentials are stronger than postsynaptic potentials, their short duration of less than 2 ms limits the number of possible simultaneous action potentials, reducing their combined strength. Additionally, two nearby neurons whose axons or dendrites point in opposite directions would cancel out just as an excitatory and an inhibitory postsynaptic potential with aligned dendrite orientation would. To reach a measurable strength, we thus need a population of at least 10,000 neurons (Murakami and Okada, 2006a) firing simultaneously and in approximately the same direction. Fortunately, about 70 to 85 percent (Wang et al., 2018) of the mammalian brain consists of so-called pyramidal neurons. These, in particular those in the fifth layer of the cortex, are characterized by a long apical dendrite that is oriented outwards from the soma to the surface of the cortex. See Figure 2.1. for a description. The postsynaptic potentials generated in the dendrites of these neurons are considered to be the primary generator of the electric and magnetic activity measurable by EEG and MEG. Apical dendrites also motivate the dipole model for neural sources. However, recent simulations based on neuron models claim that the contribution of action potentials may be as high as 20 percent (Thio and Grill, 2023).

Sensors for electric potentials and magnetic fields

An EEG measures neural activity as potential differences between electrodes. These metal electrodes are connected to a voltmeter and an amplifier, allowing measurements in the μV-range. While it is possible to place invasive electrodes directly onto the brain (Palmini, 2006), we focus on the non-invasive
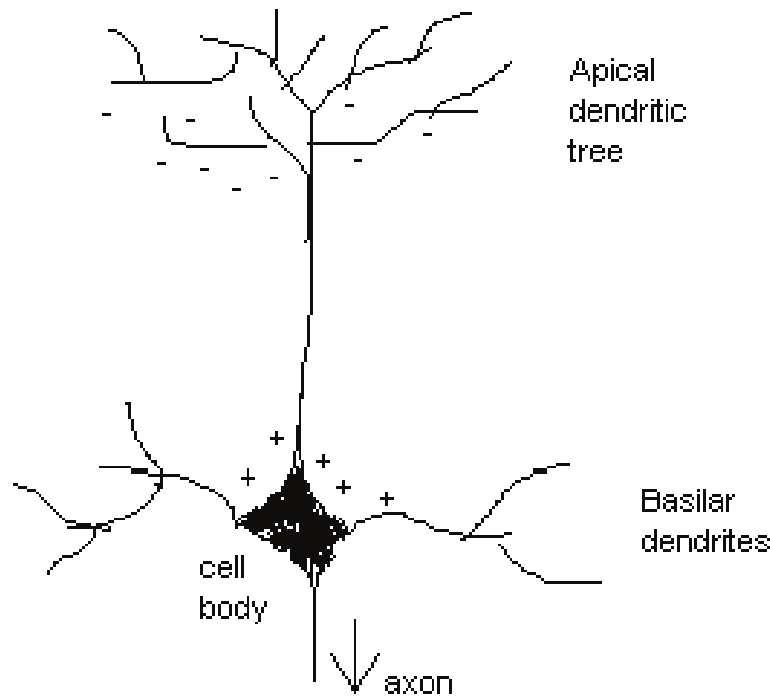
FIGURE 2.1: A pyramidal cell and the extracellular electric potential generated by an excitatory input. Taken from Salvetti and Wilamowski, 2008
.

measurement at the surface of the scalp. Here, typical voltages from brain activity range between 10-100 μV (Aurlien et al., 2004). The positioning of the electrodes is standardized, typically following a 10-20 (21 electrodes) or 10-10 (81 electrodes) system. 10 or 20 refers to the placement of one electrode every 10 or 20 percent of the distance between certain anatomical landmarks near nose, ears and back of the head (Nomenclature, 1991).

The magnetic field induced by a population of neurons typically ranges in the order of 10-1000 fT. Measuring such tiny fields (the earth's magnetic field is about 25-65 mT) requires a magnetically shielded room as well as highly sensitive sensors. These sensors or coils measure the flux of the magnetic field through the sensor surface. Coils may be arranged in several ways. The data that was measured and evaluated is based on coils that are oriented radially to the head surface. Coils are arranged in pairs, one several centimeters closer to the head than the other. The difference between the fields picked up by them forms a gradiometer, reducing low-frequency measurement noise present in the chamber. Additional coils are placed at a higher distance to the head for the same reason. Typical sensors are superconducting quantum interference devices (SQUIDS) (Cohen, 1972a) or optically pumped magnetometers (OPM) (Boto et al., 2017). SQUIDS are the more established sensor type but they are expensive to cool as their superconducting properties are only present at very low temperatures while OPMs can operate at room temperature. In this work, we focus on data measured by SQUIDS. See Figure 2.2. for a typical configuration of electrode and SQUID positions.
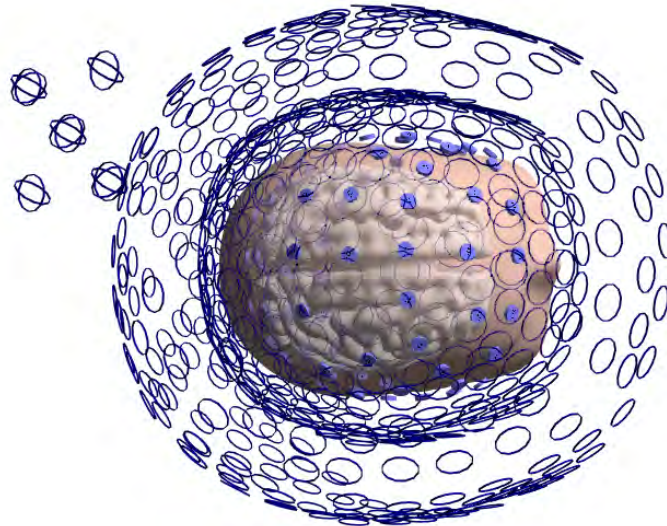
FIGURE 2.2: Typical electrode and SQUID position setup. The unfilled circles depict single coils, note that there is an inner and an outer ring of coils. Coils not in those two rings are reference coils. Electrode positions are marked by filled blue circles located on the scalp surface.

.

Effects of transcranial electric Stimulation

Transcranial direct current stimulation (tDCS) is currently used in a wide array of clinical applications ranging from pain disorders, and Parkinson's disease to depression, epilepsy, or schizophrenia (Lefaucheur et al., 2017). It has also been shown to modulate performance in sports (Edwards et al., 2017) and memory tasks (Hoy et al., 2013). The basic mechanism underlying tDCS is closely related to the resting membrane potential. A set of two or more electrodes, called anodes and cathodes depending on their polarity, are placed on the scalp to apply a current inside the brain. If this current is not aligned with the neuron's membrane, it is either depolarized or hyperpolarized. The current, typically less than 4 mA (Lefaucheur et al., 2017), is not strong enough to induce action potentials on its own but rather increases or decreases the neuron's sensitivity to incoming stimuli, i.e. its excitability. Through long-term potentiation, these stimulation effects can persist even after the stimulation is over. While the underlying mechanism is not fully understood, it is assumed that tDCS does not induce neuroplasticity on its own, but rather modulates the existing, endogenous plasticity of the brain (Kronberg et al., 2017). This may be different in transcranial magnetic stimulation, where the induced currents are strong enough to create action potentials. The orientation of the current is important, as an electric field parallel to the neuron's membrane will not affect the resting membrane potential. In practice, many studies use simple setups by identifying a brain region of interest and then placing either the anode over the target for excitatory stimulation or the cathode for inhibitory stimulation (Thair et al., 2017). The assumption behind this is that the weak fields induced by tDCS primarily affect the gyral crown and lip. This has the advantage of avoiding complex anatomical models but may lead to unexpected stimulation outcomes. An increase in stimulation duration could lead to inhibitory outcomes from anodal stimulation (Monte-Silva et al., 2013) and cathodal stimulation results conversely may become

excitatory (Batsikadze et al., 2013). Alternatively, the stimulation montage can be based on both a target location and an orientation, simultaneously optimizing the intensity and orientation of the electric field applied (Khan et al., 2022). The EEG/MEG data however is based primarily on dendritic activity, while tDCS affects all parts of the neuron, dendrites, soma, and axons. In (Rahman et al., 2013), it was shown that cathodal stimulation results in electric fields both radial and tangential to the cortical surface. Radial fields, corresponding in orientation to the apical dendrite of the pyramidal cells, facilitate the polarization of the soma of the pyramidal neurons, motivating the choice of EEG/MEG reconstructions as tDCS targets. Tangential fields in turn were found to primarily stimulate those axons and their terminals that are oriented parallel to the cortical surface, with the resulting stimulation effects potentially canceling each other due to differences in axon orientation.

2.2 Forward modeling

In EEG/MEG source reconstruction, we are interested in finding the cortical generator of a signal measured at our sensor positions. This task can be split into two separate parts: The forward and inverse problem (Mosher, Leahy, and Lewis, 1999b). The forward problem places a fixed hypothetical source into the brain and simulates the electric potential/magnetic field that would be measured at the sensor positions. The inverse problem then lies in identifying a best-fitting source or configuration of sources based on the forward simulations. In tDCS we are faced with a similar set of problems (Fernández-Corazza, Turovets, and Muravchik, 2020). Here, the target in the brain is externally provided, for example as the result of source reconstruction. TDCS forward modeling then simulates the current density vector at the target location induced by a set of hypothetical stimulation electrodes. The inverse problem again focuses on finding an optimal configuration, this time of stimulation electrodes, not neural sources.

We will start with the EEG forward problem and explore how it is related to the other two. Inverse algorithms will be introduced in later chapters where necessary but the focus of this thesis is on forward modeling.

Maxwell equations and the EEG forward problem

As we saw in the previous section, neural activity is electric in nature, the propagation of the fields it induces are therefore governed by the Maxwell equations: In the frequency spectrum of neural signals (<1000 Hz), time derivatives may be neglected and a quasi-static approximation may be used (Hämäläinen et al., 1993). Further, the relation between electric displacement field D and electric field E is given by $\epsilon_0 \epsilon_r E = D$, where ϵ_0, ϵ_r are the electric permittivity of the vacuum and the relative permittivity. For diamagnetics such as the human body, the magnetization field H is given by $H = B/\mu_0$. B is the magnetic field, μ_0 is the magnetic permeability of the vacuum which is assumed to be identical to that in human tissue.

Now let the charge density be denoted by ρ, the current density by J. Then, following Hämäläinen et al., 1993, Maxwell's equations are stated as

$$\nabla \cdot E = \frac{\rho}{\epsilon_0 \epsilon_r} \tag{2.1}$$

$$\nabla \cdot B = 0 \tag{2.2}$$

$$\nabla \times E = 0 \tag{2.3}$$

$$\nabla \times B = \mu_0 J. \tag{2.4}$$

Equation (1.3) implies that the electric field is rotation-free and can therefore be written as the gradient of a scalar potential u. In other words, $E = -\nabla u$, where u is called the electric potential. Further, we can split the current density J into a primary current j^p that represents neural activity, and secondary return currents that depend on the head's electric conductivity σ, yielding $J = j^p + \sigma E = -\sigma \nabla u$.

Inserting the split current density into (1.4) and taking the divergence on both sides yields

$$\nabla \cdot rot(B) = \nabla \cdot \mu_0 (j^p - \sigma \nabla u)$$

$$\iff \nabla \cdot \sigma \nabla u = \nabla \cdot j^p.$$

We used that the divergence of the curl is zero and replaced the electric field with the negative gradient of the electric potential. Following Munck and Peters, 1993, we arrive at the EEG forward problem:

Definition 2.1. *The EEG forward problem*
Let $\Omega \subset \mathbb{R}^3$ denote a sufficiently smooth head domain, σ the 3×3 symmetric, positive definite conductivity tensor. The EEG forward problem is then stated as finding the electric potential $u : \Omega \to \mathbb{R}$, such that

$$\nabla \cdot \sigma \nabla u = \nabla \cdot j^p \textbf{ in } \Omega \tag{2.5}$$

$$< \sigma \nabla u, n >= 0 \textbf{ on } \partial\Omega. \tag{2.6}$$

Here n is the outer unit normal. The boundary condition states that the air is not conductive. The solution to the forward problem is governed by two principal components. The conductivity tensor σ and the primary current j^p. The potential is at this point only defined up to a constant.

The conductivity tensor varies significantly from tissue to tissue. Throughout this thesis, we will distinguish up to 6 different compartments with conductivity values based on Acar, Acar, and Makeig, 2016: gray matter (0.33 S/m), white matter (0.14 S/m), cerebrospinal fluid (CSF, 1.49 S/m), skull compacta (0.0042 S/m), skull spongiosa (3.6x skull compacta Akhtari et al., 2002), scalp (0.43 S/m). The skull conductivities can also be individually calibrated using both EEG- and MEG data (Aydin et al., 2014; Schrader et al., 2020). The varying conductivity is the reason why we need accurate anatomical information, e.g. from magnetic resonance imaging (MRI).

As mentioned in the previous section, neural activity can be modeled as a mathematical point dipole. More precisely, the primary current j^p originating

from a source located at $x_0 \in \Omega$ is given by the Dirac delta distribution δ.

$$j^p := M\delta_{x_0}$$

$M \in \mathbb{R}^3$ is the dipole moment. If we return to the neuron model from the beginning, M represents the direction and strength in which the primary current is flowing, following the apical dendrite which is oriented normally to the cortical surface.

Note that δ is not a function in the classical sense, but a distribution. This means that δ_{x_0} is not evaluated at a point $x \in \Omega$ but rather that δ_{x_0} maps functions from a test function space, typically $C_c^\infty(\Omega)$ to their value at x_0. In other words,

$$\delta_{x_0} : C_c^\infty(\Omega) \to \mathbb{R}, \ \xi \mapsto \xi(x_0).$$

Another typical notation is $\delta_{x_0}(\xi) = \int \xi \delta_{x_0} \, dx = \xi(x_0)$. However, this definition is not entirely accurate as δ_{x_0} is not a function on Ω and the integral in the middle is therefore not properly defined. When we use δ in the right-hand side of equation (1.5), the equation now has to be understood in a distributional sense, i.e. that it holds when evaluated against any test function ξ.

$$\int_\Omega \nabla \cdot \sigma \nabla u \xi \, dx = \int_\Omega \nabla M \delta_{x_0} \xi \, dx$$

The derivatives of distributions are defined in a way that maintains the partial integration rule:

$$D^\alpha \delta_{x_0}(\xi) = (-1)^{|\alpha|} \delta_{x_0}(D^\alpha \xi).$$

For the MEG forward problem, we return to the Maxwell equations (Hämäläinen et al., 1993). As $\nabla \cdot B = 0$, we can write B as the curl of a magnetic vector potential, $B = \nabla \times A$. From (1.4) and Coulombs gauge it then follows that

$$\nabla \times B = \mu_0 J \Rightarrow \nabla(\nabla \times A) = \mu_0 J \Rightarrow -\nabla^2 A = \mu_0 J.$$

A can therefore be written as the solution to the Poisson equation:

$$A(x_0) = \frac{\mu_0}{4\pi} \int_\Omega \frac{J(x)}{||x_0 - x||_2} \, dx. \tag{2.7}$$

Applying $B = \nabla \times A$ and the quotient rule, we end up with the law of Biot-Savart (Hämäläinen et al., 1993):

$$B(x_0) = \frac{\mu_0}{4\pi} \int_\Omega J(x) \times \frac{x_0 - x}{||x_0 - x||_2^3} \, dx. \tag{2.8}$$

Again splitting primary and secondary current yields the MEG forward problem:

Definition 2.2. *The MEG forward problem*
Let $\Omega \subset \mathbb{R}^3$ denote the sufficiently smooth head domain, σ the 3×3 symmetric, positive definite conductivity tensor. The MEG forward problem is then stated as calculating the magnetic field B based on a neural source j^p at a location x_0 outside

the human head.

$$B(x_0) = B^p(x_0) - B^s(x_0), \tag{2.9}$$

where

$$B^p(x_0) = \frac{\mu_0}{4\pi} \int\limits_{\Omega} j^p(x) \times \frac{x_0 - x}{||x_0 - x||_2^3} \, dx, \tag{2.10}$$

$$B^s(x_0) = \frac{\mu_0}{4\pi} \int\limits_{\Omega} \sigma(x) \nabla u(x) \times \frac{x_0 - x}{||x_0 - x||_2^3} \, dx. \tag{2.11}$$

Here, u refers to the solution to the EEG forward problem for the same current source j^p, head model Ω, and conductivity tensor σ. B^p is called the primary, B^s the secondary magnetic field.

Splitting primary and secondary current has two advantages. First, we see that EEG and MEG forward problems are intrinsically connected, allowing us to compute the MEG forward problem from the EEG forward problem without having to solve another PDE.

Secondly, the primary magnetic field does not depend on the conductivity σ and can be calculated analytically. Following Sarvas, 1987, we get

$$B^p(x_0) = \frac{\mu_0}{4\pi} M \cdot \frac{x_0 - x}{||x_0 - x||_2^3}. \tag{2.12}$$

M is again the moment vector of the point dipole.

Finally, we will look at the tDCS forward problem. Here, we are interested in finding the electric field or current density induced by a set of stimulation electrodes located at $\partial\Omega$, the scalp. In this thesis we assume point electrodes, therefore we can again use the Dirac delta distribution to model the injection pattern I. See Hyvönen, 2004, for an introduction to complete electrode models. Otherwise, the same considerations regarding quasi-staticness as in the EEG case apply, yielding the tDCS forward problem (Johnson, 1997).

Definition 2.3. *The tDCS forward problem*
Let $\Omega \subset \mathbb{R}^3$ denote a sufficiently smooth head domain, σ the 3×3 symmetric, positive definite conductivity tensor. The tDCS forward problem is then stated as calculating the electric potential u such that

$$\nabla \cdot \sigma \nabla u = 0 \textit{ in } \Omega \tag{2.13}$$

$$< \sigma \nabla u, n > = I \textit{ on } \partial\Omega. \tag{2.14}$$

$$u = 0 \textit{ on } \Gamma_D \tag{2.15}$$

I denotes the injected current from an anode at location $x_a \in \partial\Omega$ and a cathode at location $x_c \in \partial\Omega$, i.e. $I = \delta_{x_a} - \delta_{x_c}$. Note again that using distributions here means that the entire equation has to be read in a distributional sense.
$u = 0$ on $\Gamma_D \subset \partial\Omega$ ensures the uniqueness of the solution (Wagner et al., 2016).

$I = \delta_{x_a} - \delta_{x_c}$ is a base scenario from which current patterns with more stimulation electrodes can be obtained by superposition. In practice, we often use up to 8 stimulation electrodes.

Note that the quantity of interest in tDCS is typically either the electric field E or the current density $-\sigma \nabla u$, not u itself.

Note the similarities between EEG and tDCS forward problems. We will exploit these and the connection to the MEG forward problem later to reduce computation times. First, however, we will investigate ways to solve the forward problems.

2.3 Quasi-analytical solutions and boundary element method

Throughout this thesis, we are primarily interested in solving the forward problems in definitions 1-3 via the finite element method (FEM). To investigate the accuracy of our FEM approaches and to serve as a comparison, we need different solution approaches.

(Quasi-)analytical solutions to all three problems can be calculated either directly or via series expansion arguments (Munck, Peters, et al., 1993; Sarvas, 1987; Ferree, Eriksen, and Tucker, 2000). However, this is only possible for simplified geometries, such as multi-layer sphere models. While these models are only rough approximations of a real human head, they contain much of its complexity. Different tissue layers such as scalp, skull, cerebrospinal fluid (CSF), and brain can be modeled with realistic thicknesses and conductivities. (Quasi-)analytical solutions in multi-layer sphere models are the most objective initial benchmark we have to test and validate new methods to solve the forward problems.

In realistic head models, such benchmarks are no longer possible. Wherever we use realistic head models in this thesis, we will therefore compare solutions from several different numerical approaches. CutFEM and a reference finite element approach will be introduced in the next two chapters. For EEG and MEG, we will additionally use the boundary element method (BEM) as additional comparison.

The following is a brief sketch of how to solve the EEG forward problem using BEM. It is based on Kybic et al., 2005.

As the name suggests, BEM operates on the tissue surfaces only. We assume N nested compartments Ω_i, separated by interfaces S_j. By Ω_{N+1} we denote the air surrounding the head. The conductivity σ_i is assumed to be constant on each tissue.

For a function $g : \mathbb{R}^3 \to \mathbb{R}$, we define the interface jump $[g]_j = g_{S_j}^- - g_{S_j}^+$, where

$$g_{S_j}^{\pm}(r) = \lim_{\alpha \to 0^{\pm}} g(r + \alpha n)$$

for $r \in S_j$ and n is the outer unit normal at r. This leads to a modified EEG forward problem

$$\sigma_i \Delta u = f \ \text{ on } \Omega_i$$

$$\Delta u = 0 \ \text{ on } \Omega_{N+1}$$

$$[u]_j = [\sigma \partial_n u]_j = 0 \ \text{ on } S_j$$

The added jump equations enforce a continuity of the electric potential and the current density vector over interfaces S_j.

We can now setup an individual, homogeneous PDE for each Ω_i:

$$\sigma_i \Delta v_i = f|_{\Omega_i}.$$

By convolution with the Green's function

$$G(r) = \frac{1}{4\pi||r||_2},$$

solutions are obtained as $v_i = -f|_{\Omega_i} * G$. Notably, $\Delta v_i = -f|_{\Omega_i}$ on the entirety of $\mathbb{R}^3$, hence v_i is harmonic ($\Delta v_i = 0$) on $\mathbb{R}^3/\bar{\Omega}_i$.

Given these homogeneous solutions, we now define harmonic helper functions

$$V_s = u - \sum_{i=1}^{N} \frac{v_i}{\sigma_i},$$

$$V_d = u - \sum_{i=1}^{N} v_i.$$

It can be shown that $[V_s]_j = [\partial_n V_d]_j = 0$. Hence, V_s is a single-layer potential and V_d a so-called double layer potential. These functions lead to two different, independent ways of solving the EEG forward problem. A third method, the symmetric BEM, contains elements of both the single- and the double-layer potential approach by introducing one helper function V_i per compartment:

$$V_i = \begin{cases} u - \frac{v_i}{\sigma_i} & \text{in } \Omega_i \\ \frac{-v_i}{\sigma_i} & \text{else} \end{cases}$$

The principal idea behind all these three BEM approaches is now identical. As the helper functions are harmonic, a fundamental theorem for harmonic functions can be applied, yielding integral equations either for the helper functions or directly for the electric potential u and current density $-\sigma\nabla u$ (Nédélec, 2001). These surface integrals are then solved using collocation/Galerkin approaches by triangulating the tissue surfaces.

The resulting linear equations systems are dense when compared to those from the finite element method, limiting the computationally feasible resolution of the triangulation. Established MEG/EEG BEM toolboxes therefore often focus on 3 tissues (skin, skull, brain) only (Gramfort et al., 2011). Fast multipole approaches aim at alleviating this limitation and enable a larger number of distinct tissues (Makarov et al., 2020). The symmetric BEM has been shown to yield superior results when compared with single-/double-layer potential approaches and will therefore be used throughout this thesis.

In this chapter, we investigated neural sources in the brain, the electric and magnetic fields the produce and how they can in turn be stimulated transcranially. We then described how to derive the respective forward problems for EEG/MEG/tDCS from the Maxwell equations and gave a short outline how they can be solved in spherical and three-layer models. The next chapter will focus on more complex geometries.

Chapter 3

Weak formulations and the finite element method

In the previous chapter, we derived the partial differential equations associated with the forward problems of EEG, MEG, and tDCS. We also saw that for simplified geometries there exist quasi-analytic solutions. For more complex geometries, we mentioned the boundary element method (BEM) which will serve for comparison later.

In this chapter, we give a short introduction to solving the forward problems that were derived in the previous chapter using the finite element method (FEM). First, the underlying framework of weak derivatives and Sobolev spaces will be introduced and subsequent weak formulations for our forward problems will be derived. We will further discuss the existence and uniqueness results of these equations.

Secondly, we will introduce FEM as an approach to solve the weak formulations from the first section and derive the corresponding linear equation systems.

Finally, we will investigate how transfer matrices can be used to reduce computational effort and how all three forward problems can be reduced to essentially solving the same PDE.

3.1 Weak derivatives, existence, and uniqueness

Initially, the forward problems for EEG/MEG and tDCS were stated in a classical sense. The equation was understood to hold point-wise. However, when using Dirac distributions as right-hand sides the equations can only be read in a distributional sense, by evaluation against test functions. Defining weak derivatives goes in a similar direction, their motivation stems from the integration by parts formula, we follow the introduction outlined in Evans, 2022.

Let $\Omega \subset \mathbb{R}^d, u \in C^1(\Omega), \phi \in C_c^\infty(\Omega)$. Then we have

$$\int_\Omega u \frac{\partial \phi}{\partial x_i} \, dx = - \int_\Omega \frac{\partial u}{\partial x_i} u. \ \text{ for all } i \in \{1,..,d\}$$

Boundary terms disappear as ϕ is zero on $\partial\Omega$.

More generally, let $\alpha \in \mathbb{N}^d$ be a multi-index. Then we have for $u \in C^n(\Omega)$

$$\int_\Omega u D^\alpha \phi \, dx = (-1)^{|\alpha|} \int_\Omega D^\alpha u \phi \, dx.$$

This equation must hold when u is at least $k = |\alpha|$ times continuously differentiable. However, it may be true for a larger class of functions, motivating an extension/weakening of the classical concept of differentiability.

Definition 3.1. *Weak derivatives*
    Let $\Omega \subset \mathbb{R}^d$, $\alpha \in \mathbb{N}^d$ be a multi-index and $u, v \in L^1(\Omega)$ Then v is called the α-th weak derivative of u if

$$\int_\Omega u D^\alpha \phi \, dx = (-1)^{|\alpha|} \int_\Omega v \phi \, dx \ \text{ for all } \phi \in C_c^\infty(\Omega). \tag{3.1}$$

It can be shown that the weak derivative is unique and, if a classical derivative also exists and is continuous, the two coincide. If we further demand that both u and the weak derivative lie in $L^2(\Omega)$, we end up with a Hilbert space, leading to the definition of a class of Sobolev spaces.

Definition 3.2. *Sobolev Space*
    Let the above settings hold, $k \in \mathbb{N}$. Then the Sobolev space $H^k(\Omega)$ defined as

$$H^k(\Omega) := \{u \in L^2(\Omega) : \forall |\alpha| \le k \ \exists v \in L^2(\Omega) : v \text{ is the weak derivative of } u\} \tag{3.2}$$

is a Hilbert space with associated scalar product and norm

$$||u||_{H^k}^2 = <u, u>_{H^k} := \sum_{|\alpha| \le k} ||D^\alpha u||_{L^2}^2. \tag{3.3}$$

An exemplary function that has a weak, but not a strong derivative, is $f(x) = |x|$. When solving our PDEs, we will look for solutions in Sobolev spaces. The main advantage of doing so lies in the fact that existence and uniqueness result from functional analysis such as the following Lax-Milgram theorem can be used.

Theorem 3.1. *Lax-Milgram theorem*
    Let $(<\cdot, \cdot>, V)$ be a Hilbert space, $a : V \times V \to \mathbb{R}$ a bilinear form, $l : V \to \mathbb{R}$ a bounded, linear functional. If for any $v_1, v_2 \in V$

$$(i): \ \exists C_1 > 0 : |a(v_1, v_2)| \le C_1 ||v_1|| ||v_2|| \ \ \text{(continuity)} \tag{3.4}$$

$$(ii): \ \exists C_2 > 0 : C_2 ||v_1||^2 \le a(v_1, v_1) \ \ \text{(coercivity)}, \tag{3.5}$$

then there exists exactly one $u \in V$ such that

$$a(u, v) = l(v) \ \forall v \in V. \tag{3.6}$$

Proof. See Evans, 2022. $\square$

Now we can return to our forward problems and derive weak formulations in the setting of Sobolev spaces. Note that as the MEG solution can be directly computed from the EEG solution, we only need to derive versions for EEG and tDCS.

3.1.1 Weak EEG forward problem

For the EEG, we first introduce the Sobolev space with zero mean:

$$H_*^1(\Omega) := \{u \in H^1(\Omega) : \int_\Omega u \, dx = 0\}.$$

This restriction is necessary for the EEG problem to have a unique solution. Physically, since the electric potential is only defined up to a constant. Mathematically, to show the coercivity of the upcoming bilinear form.

Starting with equation (1.5), multiplication with a test function $v \in H_*^1(\Omega)$ and integrating over Ω yields

$$\int_\Omega \nabla \cdot \sigma \nabla u v \, dx = \int_\Omega \nabla \cdot j^p v \, dx.$$

After integration by parts and applying (1.6), we end up with the weak EEG forward problem:

Definition 3.3. *The weak EEG/MEG forward problem*
Find $u \in H_*^1(\Omega)$ such that

$$a(u,v) = l(v) \quad \forall v \in H_*^1(\Omega), \tag{3.7}$$

with

$$a(u,v) = \int_\Omega \sigma \nabla u \cdot \nabla v \, dx, \tag{3.8}$$

$$l(v) = \int_\Omega f v \, dx. \tag{3.9}$$

Note that we substituted $\nabla \cdot j^p$ with a function f to avoid the singularity in the weak forward problem. In the coming pages, we will explore three so-called source models: Approaches to choose f in a manner that approximates $\nabla \cdot j^p$ while maintaining sufficient regularity.

The full subtraction approach

The first one splits the conductivity into two parts, a constant part, and one that is zero near the source.

Definition 3.4. *The full subtraction approach*
Let $\Omega^\infty \subset \Omega$ be a small domain with constant conductivity $\sigma(x) = \sigma^\infty \ \forall \ x \in \Omega^\infty$ containing the source position x_0. Then both the conductivity and the electric potential can be split into a so-called infinity part and a correction part: Let $x \in \Omega$, then

$$\sigma(x) = \sigma^\infty + \sigma^c(x) \tag{3.10}$$

$$u(x) = u^\infty(x) + u^c(x). \tag{3.11}$$

Applying this split to the EEG forward problem yields two equations: One for the infinity potential that depends on the singularity and one for the correction potential, that disappears on Ω^∞ and only requires the infinity potential.

$$\nabla \cdot \sigma^\infty \nabla u^\infty = \nabla \cdot j^p \ \text{ in } \ \mathbb{R}^3. \tag{3.12}$$

Note that this equation is over the entire $\mathbb{R}^3$, not only over Ω as σ^∞ is assumed to be constant everywhere.

The second PDE is stated as:

$$-\nabla \cdot \sigma \nabla u^c = \nabla \cdot \sigma^c \nabla u^\infty \ \ in \ \ \Omega \tag{3.13}$$

$$\sigma \nabla u^c \cdot n = -\sigma \nabla u^\infty \cdot n \ \ on \ \ \partial\Omega. \tag{3.14}$$

The infinity potential can be calculated analytically (Wolters et al., 2008; Sarvas, 1987). For the correction potential, we can again move to a weak formulation with corresponding bilinear form $a(\cdot, \cdot)$ and functional $l(\cdot)$. Wolters et al., 2008 show that the bilinear form is continuous and coercive in $H^1_*(\Omega)$. Note that the second equation no longer has a singularity in it. Therefore, $l(\cdot)$ lies in $H^1_*(\Omega)$ and the equation fulfills the requirements of Lax-Milgram. Recent developments have led to the local subtraction approach (Höltershinken et al., 2023), improving computation times while maintaining a solid mathematical understanding.

The St. Venant source model

Another approach is the St. Venant or blurred dipole approach (Buchner et al., 1997; Wolters et al., 2007).

Definition 3.5 (The St. Venant source model)**.** *In the St. Venant method, the dipolar source term is substituted by an appropriate set of N monopoles located at $x_i \in \Omega, i \in \{1, ..., N\}$.*

$$\rho = \sum_{i=1}^{N} q_i \delta_{x_i}.$$

The positions are fixed, determined by the finite element mesh that will be set up in the following sections. Usually, the x_i will be located within the gray matter. The monopole strengths q_i are selected in a manner such that a certain selection of the first $M \in \mathbb{N}$ moments of the dipolar distribution and the monopole distribution are identical: Let $l \in \mathbb{N}, l < M$, the l-th centered moment is then defined as

$$S_l(f) = \int_\Omega (x - x_0)^l f(x) dx.$$

Then $S_l(\rho) = \sum_i q_i (x_i - x_0)^l$. $S_l(\nabla \cdot M\delta_{x_0}) = 1$, if $l = 1$ and 0 else.

The difference between $S_l(\rho)$ and $S_l(\nabla \cdot j^p)$ can then be minimized over the q_i's where the exact definition of the minimization functional depends on the type of Venant approach, see e.g. Buchner et al., 1997; Vorwerk, 2016; Nüßing, 2018; Vorwerk et al., 2019. Similar to the subtraction approach, it can be shown that there exists a unique solution if the dipole is approximated using a monopole distribution (Hanrath, 2019).

The partial integration approach

Finally, we will investigate the partial integration approach (Lew et al., 2009b). Note that by the definition of the derivative of the Dirac delta distribution we have

$$\nabla \cdot M\delta_{x_0} v = -M\delta_{x_0} \nabla v,$$

for test functions $v \in C_c^\infty(\Omega)$. This approach has certain advantages: First, it is not an approximation. The term on the right can easily be evaluated for a wide array of functions v and if you read the EEG forward problem in a distributional sense then this is simply how the right-hand side is defined. However, the v we choose in FEM is not necessarily differentiable or even continuous as we will see in the coming sections. We therefore have to make sure that it is at least smooth in an area around the source location x_0.

We have derived a weak formulation for the EEG forward problem and investigated ways to model the singularity of our neural source in three different ways, each with its own advantages and disadvantages. By extension we have therefore also dealt with the MEG forward problem, leaving only the tDCS forward problem.

3.1.2 The tDCS forward problem

TDCS is somewhat different from the EEG problem as the singularity is located on the boundary, not inside the volume conductor. Here, we do not solve an auxiliary problem like in the EEG case. Rather, existence and uniqueness can be shown directly for the singular equations (Frank, 03/2022). To do so, we need a link between Sobolev spaces and the delta distributions. First, we extend our definition of Sobolev spaces $H^s(\Omega)$ to arbitrary real values of s, by making use of an intrinsic relation between weak differentiability and Fourier transformations:

Let $u \in L^1(\mathbb{R}^n)$. The Fourier transform is then defined as

$$F : L^1(\mathbb{R}^n) \to C_0(\mathbb{R}^n), \quad F(u)(y) = 2\pi^{-n/2} \int_{\mathbb{R}^n} u(x) e^{-ixy} dy \qquad (3.15)$$

Secondly, we denote by $S(\mathbb{R}^n)$ the space of rapidly declining functions or Schwartz space

$$S(\mathbb{R}^n) = \{\phi \in C^\infty(\mathbb{R}^n) \mid \forall \alpha, \beta \in \mathbb{N}^n : \sup |x^\alpha D^\beta \phi(x)| < \infty\}.$$

Given the definitions of the Fourier transform and the dual of Schwartz space S', it can be shown that for $m \in \mathbb{N}$

$$H^m(\mathbb{R}^n) = \{u \in S'(\mathbb{R}^n) : (1 + ||y||^2)^{m/2} Fu(y) \in L^2(\mathbb{R}^n)\}. \qquad (3.16)$$

The above spaces can be restricted to $\Omega \subset \mathbb{R}^n$. Note that the set on the right-hand side is sensible for all $m \in \mathbb{R}$, giving us an according extension of H^m for arbitrary $m \in \mathbb{R}$. With respect to the delta distributions, it can be shown that

$$\delta \in H^{-3/2-\epsilon}(\Omega), \quad \delta \in H^{-1-\epsilon}(\partial\Omega) \; \forall \, \epsilon > 0.$$

We now have the necessary function spaces in which a solution to the tDCS forward problem exists:

Theorem 3.2 (Existence and uniqueness for tDCS forward problem). *Let* $x_a, x_c \in \partial\Omega$, $I = \delta_{x_a} - \delta_{x_c}$ *and* $\epsilon > 0$. *Then the tDCS forward problem for point*

electrodes lies in finding a $u \in H^{1/2-\epsilon}(\Omega) \cap H^1_{loc}(\Omega)$:

$$\int_\Omega \sigma \nabla u \cdot \nabla v \, dx = 0 \quad \forall v \in C^\infty_c(\Omega), \tag{3.17}$$

$$< \sigma \nabla u, n >= I \quad on \; \partial\Omega. \tag{3.18}$$

It has a unique solution.

Proof. See Frank, 03/2022. $\square$

Note that for more regular current injection patterns $I \in H^{-1/2}_*(\partial\Omega)$, such as the complete electrode model, existence and uniqueness can be shown using Lax-Milgram, see e.g. Wagner et al., 2016.

Using Sobolev spaces and weak derivatives we have redefined our forward problems in a setting in which the existence of unique solutions can be proved. Now we can proceed and investigate a numerical method to solve these equations.

3.2   The finite element method

The solutions to the equations that were stated above are in infinite-dimensional spaces V. In order to solve them numerically, we approximate the solutions in finite-dimensional spaces V_h, where h characterizes the resolution of our approximation, in a way the dimensionality of V_h. The principle behind finite element modeling lies in the setup of V_h. The basic idea is to discretize the head domain Ω into a tesselation, a set of simple polygonal elements. On these elements, we define a set of basic trial functions that span up V_h. A triple of mesh element, trial functions and associated degrees of freedom is called a finite element. Different finite element approaches vary in the way that these trial functions are set up, if $V_h \subset V$, then the discretization is considered conforming. In this section, we will introduce FEM by means of a conforming, continuous Galerkin (CG-)FEM. The section mainly follows the introduction in Braess, 2007. CutFEM, which will be introduced in the next chapter, belongs to the non-conforming FEM.

We start by introducing tesselations:

Definition 3.6. *Tesselation*

Let $\Omega \subset \mathbb{R}^3$. A tesselation or mesh of Ω is a set $\mathcal{T}_h(\Omega) = \{E_0, ..., E_m - 1\}$ of disjunct, convex polytopes $E_i \subset \Omega$ such that

$$\bigcup_{i=0}^{m-1} \bar{E}_i = \bar{\Omega}.$$

The tesselation is called admissible for FEM if $\bar{E}_i \cap \bar{E}_j$ consists either of a single common vertex, a common edge, or a common face. This implies that there are no hanging nodes.

Tesselations are characterized by a mesh resolution parameter h associated with the shape and diameter of the elements of $\mathcal{T}_h$. By $h_T = diam(T), T \in \mathcal{T}_h$, we define the diameter of T and by $h = max_{T \in \mathcal{T}} h_T$ the maximal diameter in

$\mathcal{T}_h$. The diameter alone is not enough to characterize the mesh resolution, hence we assess the shape as well: $\mathcal{T}_h$ is called shape-regular if there is a $\mathcal{K} > 0$ such that for any $T \in \mathcal{T}$ we find a circle with radius r_T contained within T such that

$$r_T \leq h_T / \mathcal{K}.$$

Now that we have a proper discretization of Ω, we can proceed and define a function space V_h associated with it. Remember that V_h is supposed to be a subspace of $H^1(\Omega)$. The functions should be associated with the mesh elements and their integration over the mesh elements should be simple. Hence we choose the continuous piece-wise polynomial functions of order $k \in \mathbb{N}$.

Definition 3.7. *Finite element space*

$$V_h^k := \{v_h \in C^0(\bar{\Omega}) : v_h|_T \in P^k \forall T \in \mathcal{T}_h\}. \tag{3.19}$$

Note that we only choose polynomial functions for tetrahedral mesh elements. In the case of hexahedral elements, we choose $P^k = Q^k$, the space of multilinear functions of order up to k instead. For conforming finite element approaches in this thesis, we will only look at $k = 1$ and omit the superscript in V_h^1. As basis functions for V_h, we choose a Lagrange basis $\{\phi_i\}_{i \leq N}$ on the N vertices $x_i, i \leq N$ of our tesselation, fulfilling

$$\phi_i(x_j) = \begin{cases} 1, & i = j \\ 0 & i \neq j. \end{cases}$$

The first-order Lagrangian basis functions are also called hat functions as they peak with value 1 at their respective node x_i and decrease to 0 when moving towards neighboring nodes x_j. For higher-order lagrangian bases, we can select additional equidistant nodes on each mesh element. Any function $v_h \in V_h$ can therefore be written as $v_h = \sum_i c_i \phi_i$. The number of basis functions is the number of degrees of freedom (DoF) in our model.

With this function space, we can now discretize our weak forward problems, starting again with the EEG. Inserting u_h into (2.7) yields one equation per basis function, i.e.

$$a(u_h, \phi_i) = l(\phi_i) \, \forall \, i \leq N.$$

Writing these equations in matrix-shape, we obtain the discretized EEG forward problem:

Definition 3.8. *The discrete EEG forward problem*

Let $\Omega \subset \mathbb{R}^n$ be our head domain, $\mathcal{T}_h$ a tesselation of Ω and V_h the first order lagrangian nodal basis on $\mathcal{T}_h$. Then the discrete EEG forward problem is stated as finding $u_h = \sum_i u_i \phi_i \in V_h$ such that

$$A\mathbf{u} = b, \tag{3.20}$$

where $A \in \mathbb{R}^{N \times N}$, with

$$a_{ij} = \int \sigma \nabla \phi_i \nabla \phi_j \, dx.$$

A is called the stiffness matrix. $\mathbf{u} \in \mathbb{R}^N$ is the coefficient vector that characterizes u_h. The right-hand side b depends primarily on the source model, for partial integration

we get

$$b_i^{Pi} = -M \cdot \nabla \phi_i(x_0).$$

For the Venant approach, we obtain

$$b_i^V = \sum_j q_j \phi_i(x_j),$$

where the q_j are the monopole loads and x_j their vertex locations. x_0 is as always the source position, M the dipole moment.

The subtraction approach solves a different problem associated with the correction potential u^c but can be derived in a similar manner.

Note that the right-hand side from the partial integration model is constant on each element $T \in \mathcal{T}_h$ if first-order polynomials are selected. The solution to (2.20) will therefore be identical for each $x_0 \in T$, limiting the accuracy of the method by the mesh resolution.

Both the Venant and partial integration approach yield sparse right-hand sides, allowing for a fast and efficient calculation of solutions. The full subtraction approach leads to a dense right-hand side vector and is therefore impractical for realistic head models with millions of DoFs. Recently, a local version of the subtraction has been developed, leading to a sparse right-hand side while maintaining the well-understood mathematical background of the full subtraction approach (Höltershinken et al., 2023).

For the MEG, the discrete version of the secondary magnetic field can simply be calculated from the discrete EEG version.

Definition 3.9. *The discrete MEG forward problem*
Let $u_h = \sum_i c_i \phi_i$ be the solution to (2.20). Then the secondary magnetic field B^s is given by

$$B^s(x) = \sum_i c_i \frac{\mu_0}{4\pi} \int_\Omega \sigma \nabla \phi_i \times \frac{y-x}{||y-x||^3} \, dy = <\mathbf{u}, S_x>, \qquad (3.21)$$

with

$$(S_x)_i = \frac{\mu_0}{4\pi} \int_\Omega \sigma \nabla \phi_i \times \frac{y-x}{||y-x||^3} \, dy.$$

Calculating the secondary magnetic field at a sensor location x outside Ω can therefore be interpreted as applying a functional S_x on the discretization of Ω to the electric potential u_h.

Both the discrete equations for EEG and MEG suffer from the fact that a new coefficient vector $\mathbf{u}$ for the electric potential has to be calculated for each source position x_0 and moment vector M. For realistic head models, the number of possible source positions goes into the tens of thousands, making a direct computation for each source infeasible. This can be alleviated by introducing the concept of transfer matrices (Munck, Wolters, and Clerc, 2012; Gençer and Acar, 2004; Wolters, Grasedyck, and Hackbusch, 2004).

Transfer matrices for EEG and MEG

In this section, we want to investigate efficient ways of calculating the electric potential and magnetic field for a large number of different source positions

x_0. We make use of the fact that we are only interested in the potential/field values at the sensor positions. Starting with the MEG, inserting (2.20) into (2.21) we obtain

$$B^s(x) = S_x u = S_x A^{-1} b =: T_x b.$$

Now we can solve for T, yielding

$$A T_x^t = S_x^t,$$

where we used that A is symmetric. The advantage of solving for T_x rather than solving for u lies in the fact that T_x does not depend on the source term b. Rather than having a separate equation for each source term b, we can now solve once for T_x and then perform one multiplication $T_x b$ per source term to obtain the secondary magnetic field strengths. T_x depends on the sensor position x so we have one equation per sensor. Combining the vectors $(T_x)_x$ into one matrix, we obtain the MEG transfer matrix T^{MEG}. Calculating $B^s(x)$ is then a computationally cheap matrix-vector multiplication that has to be performed once per dipole. We gather the set of all outputs in a so-called lead field matrix $L^{MEG} \in \mathbb{R}^{s \times l}$, where s is the number of sensors and l the number of dipoles.

An almost identical procedure can be performed for the EEG. Note again that we are only interested in evaluating the electric potential at a set of pre-defined electrode positions. Recall that the electric potential states voltage differences between the electrode positions and is therefore only defined up to a constant. Here, we will focus on the potential difference between two electrodes, an active electrode at x_a that is measured against a reference electrode at x_r. Evaluating

$$u_h(x_a) - u_h(x_r) = \sum_i c_i (\phi_i(x_a) - \phi_i(x_r)) = \; <u, R_{a,r}>$$

with

$$(R_{a,r})_i = \phi_i(x_a) - \phi_i(x_r) \tag{3.22}$$

again motivates the definition of a sensor functional. Identical to the MEG case we can now set up a transfer matrix T^{EEG} by solving

$$A T_{a,r}^t = R^t$$

for each electrode pair. Again, the electric potential is calculated by multiplying with the vector b, and the result for all dipoles is stored as the EEG lead field matrix L^{EEG}. Note that EEG potentials are only defined up to a constant, we therefore typically apply common average referencing and subtract the across-sensor mean. $L_{i,k}^{EEG}$ then states the electric potential difference between the i-th sensor and the across-sensor average given the k-th dipole at unit strength.

We stated ways to efficiently compute the electric potential and secondary magnetic fields using transfer matrices. In the next section, we will investigate the discrete tDCS forward problem and how it is related to the EEG transfer matrix.

EEG and tDCS: Helmholtz reciprocity

In contrast to the EEG equation, the tDCS forward problem still consists of two parts. To apply the finite element method, we still need to combine the two. When applying the Gauß divergence theorem to the left-hand side, we obtain

$$\int_\Omega \sigma \nabla u \cdot \nabla v \, dx = \int_{\partial\Omega} I v_h \, dS = v_h(x_a) - v_h(x_c) \; \forall v_h \in V_h.$$

Similar as in the EEG/MEG case, this yields a linear equation system

$$A\mathbf{u} = b,$$

where A is again the same matrix as in the EEG/MEG case and

$$b_i = \phi_i(x_a) - \phi_i(x_c).$$

Hence, the discrete tDCS forward problem is identical to solving the transfer matrix problem in EEG. This relationship between EEG and tDCS has also been characterized as Helmholtz reciprocity (Vallaghé, Papadopoulo, and Clerc, 2009; Rush and Driscoll, 1969).

Theorem 3.3. *Helmholtz Reciprocity*
Let u be the solution to the EEG forward problem for a source at x_0 and moment M, and w the solution to the tDCS forward problem for two point electrodes at x_a, x_c. Then

$$u(x_a) - u(x_c) = M \cdot \nabla w(x_0).$$

In other words, the potential difference between two electrodes induced by a point dipole at x_0 can be calculated from the electric field induced by two stimulation electrodes. The left-hand side can easily be calculated for a wide array of source positions x_0 and moments M.

In this chapter, the foundations for numerically solving the bioelectromagnetic forward problems were laid. We introduced weak derivatives and Sobolev spaces for two reasons. First, to obtain a functional analytic framework in which the existence and uniqueness of solutions could be proved. Secondly, the resulting integral equations can be solved using the also introduced finite element method.

Finally, it was shown that the EEG and MEG forward problem can be thought of as applying a sensor function to the EEG solution u_h. Using transfer matrices, we can shift the computational load from one PDE per neural source to one PDE per sensor. Finally, we have seen that all three forward problems give rise to the same stiffness matrix A and how the EEG transfer matrix and the solution to the tDCS forward problem coincide.

Given these results and in particular the short introduction to the finite element method, we can now proceed to investigate short-comings of existing mesh generation for FEM, and how they motivate the use of unfitted finite element methods such as CutFEM, which will be introduced in the next chapter.

Chapter 4

A cut finite element method

Before introducing the cut finite element method, we will investigate reasons why there is room for yet another way to solve the bioelectromagnetic forward problems.

Up to now, we have seen quasi-analytic solutions yielding accurate reference solutions, yet they are only available for simple spherical geometries (Sarvas, 1987; Munck, van Dijk, and Spekreijse, 1988). We briefly touched upon basic boundary element methods (BEM), which lead to densely populated equation systems, limiting the feasible number of degrees of freedom (DoF) and thus the resolution of the head model. Additionally, BEM is not a volumetric method, hence anisotropic compartments are unavailable. However, recently fast multipole methods have been developed to alleviate these concerns (Makarov et al., 2020).

The conforming finite element method (FEM) that we explored in the final parts of the previous chapter offers both sparse stiffness matrices and the volumetric mesh underlying FEM can accommodate tissue anisotropies. FEM allows for highly accurate head models with millions of DoFs at reasonable computational costs (Lew et al., 2009a; Vorwerk et al., 2014).

There is however a caveat. The tesselation/mesh that FEM operates on assumes that each of its elements is completely contained within one tissue compartment, i.e. σ is constant on each element. The compartment boundaries are therefore represented by the boundary of the mesh elements and this representation may not entirely coincide with the tissue boundaries obtained from MRI segmentation. 3D mesh elements are typically either hexahedrons or tetrahedrons. Both of these options have certain advantages but also limitations.

We start by looking at hexahedrons. Segmentation results often come in the shape of binary maps, i.e. voxelized images in which each voxel either has a value of 0 or 1, depending on whether the voxel is considered inside or outside the respective compartment. Each voxel can be identified as one hexahedron, making for a straightforward meshing process. However, due to their cubic structure, the boundary of a hexahedral mesh will have a staircase pattern while the tissues in the human head, in particular the cortical folds, are innately curved. This staircase pattern can be reduced by shifting boundary vertices either inward or outward but the resulting mesh cannot be fully smooth as can be seen in Wolters et al., 2007. Additionally, hexahedral meshes may suffer from skull leakages. In areas where the skull is very thin this may lead to meshes with only one diagonal layer of skull hexahedrons, resulting in scalp and brain hexahedrons that share a vertex. This shared vertex constitutes a hole/leak in the skull. Such leakages can be alleviated

by using discontinuous Galerkin (DG) type methods (Engwer and Nüßing, 2017). These however massively increase the number of degrees of freedom without providing additional mesh resolution.

Tetrahedra on the other hand are much better suited to represent curved structures. They are typically created from surface triangulations (Windhoff, Opitz, and Thielscher, 2013; Nielsen et al., 2018). While their boundary representation can in theory be more accurate than that of hexahedrons, creating a tetrahedral mesh is significantly more complicated. The quality of a finite element approximation using a tetrahedral mesh is strongly dependent on the regularity of the individual tetrahedrons. Pointy and in particular blunt elements may lead to numerical errors (Shewchuk, 2002). For head model generation, this is particularly relevant for thin or vanishing areas, for example where the brain touches the inner skull. Here, the cerebrospinal fluid separating the skull and brain becomes thinner and thinner before vanishing. Modeling such CSF compartments in a robust and automated way is not easily achievable using tetrahedral mesh generators. Therefore, most FEM toolboxes for EEG/MEG/tDCS that employ tetrahedral meshes post-process the segmentation results to ensure that the tissues are nested: white matter is fully surrounded by gray matter, which is entirely coated in CSF and so on.

The central motivation for CutFEM is therefore to create a FEM-based computational framework that accurately represents the segmentation results by integrating the strengths of hexahedrons and tetrahedrons. We will now proceed with the meshing process in CutFEM.

4.1   A two-stage mesh generation

We recall that in the classical FEM described in the previous chapter, the mesh serves two purposes. The elements of the tesselation define the support of the basis functions that span the finite-dimensional trial function space V_h, in which we search for an approximate solution. Additionally, the tissue compartments are also represented by the elements, as each element belongs to exactly one tissue.

In CutFEM, these two properties are decoupled by introducing a 2-stage meshing process. First, a fundamental/background mesh $\mathcal{T}_h$ is created. It contains no information concerning the head domain Ω other than $\Omega \subset \mathcal{T}_h$. Typically, $\mathcal{T}_h$ is a tesselation of uniform, simple elements, either tetrahedrons (Burman, 2010) or hexahedrons, which will be used throughout the following chapters.

Here, an initial space of trial functions $\hat{V}_h$ with lagrangian basis is defined in the same manner as for the classical FEM from the previous chapter. In the second step, the mesh is adapted to the tissue compartments Ω_i, $\bigcup_i \Omega_i = \Omega$. We do so by defining level set functions $\phi_i : \Omega \to \mathbb{R}$, one for each compartment. The ϕ_i have a simple structure, satisfying

$$\phi_i(x) \begin{cases} < 0, & x \in \Omega_i \\ = 0, & x \in \partial\Omega_i \\ > 0, & x \notin \bar{\Omega}_i. \end{cases}$$

the zero-set of ϕ_i therefore defines the boundary of the $i-$th compartment. This level set is now used to cut the elements of $\mathcal{T}_h$ into smaller pieces that conform to the compartments. In essence, two approximation steps are performed. At first, the level set function ϕ may belong to an arbitrary function class. It is approximated by a multi-linear function ϕ_h, meaning that we evaluate ϕ at a set of predetermined locations and fit a multi-linear function to these values. In practice, the resolution of this multi-linear function is limited by the resolution of our segmentation input. If our MRI has a 1x1x1 mm resolution, we essentially have one value per cubic centimeter. This value is then interpreted as the signed distance of the center of the voxel to the zero-level of ϕ_h. The second step then lies in applying a topology preserving marching cubes (TPMC, Engwer and Nüßing, 2017) algorithm to the mesh and ϕ_h, replacing each element $E_j \in \mathcal{T}_h$ by a set of simple polygons $\{E_{j_k}\}_k$, that conform to the zero-line of ϕ_h. These so-called snippets serve the second purpose of the mesh, representing the tissue compartments. Each snippet E_{j_k} belongs to one compartment alone, we can therefore approximate $\Omega_i \approx \hat{\Omega}_i := \{E_{j_k} : E_{j_k}$ belongs to $\Omega_i\}$. The snippets inside one element that belong to the same compartment form a cut cell. The mesh consisting of the snippets is called the cut mesh.

The cut mesh is created iteratively and TPMC is applied once per level set function. First, the fundamental mesh is cut by the first level set function denoting the boundary of the first tissue, resulting in the first stage of the cut mesh. This cut mesh is then cut by the second level set and so on. The entire process can then be repeated to further refine the cut mesh and improve the approximation. The limit here is the resolution of the level set function. For sphere models, we could calculate level sets of arbitrary resolution but in practice, the segmentation result is based on voxelized images that typically have a resolution of no more than 1x1x1 mm. Refining the cut mesh is e.g. relevant when we use a 2 mm background mesh and have a 1x1x1 mm voxel resolution.

To recapitulate, each background mesh element may contain sections of multiple compartments. The background elements are then split into multiple cut cells made up of snippets that conform to the tissues present inside the element.

Next, we define an individual trial function space for each compartment as a restriction of $\hat{V}_h$.

$$V_{h_i} := \{v\chi_{\hat{\Omega}_i} : v \in \hat{V}_h\} \tag{4.1}$$

Here, χ is the indicator function. In other words, we take the full trial function space and cut it off at the boundary of Ω_i, giving rise to the name Cut-FEM.

The full trial function space is then defined as the direct sum of the subspaces

$$V_h := \bigoplus_i V_{h_i}.$$

Note that when defining the langrangian basis one vertex corresponds to one trial function. In CutFEM, a single vertex can correspond to multiple trial functions, one per tissue in the adjacent elements. This may seem surprising at first as the physical location of the node is only inside one compartment.
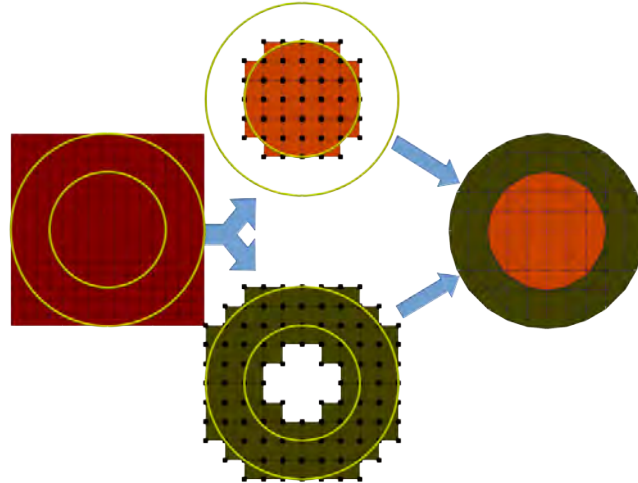
FIGURE 4.1: Schematic overview of the Cut finite element method. Left: fundamental mesh and level sets for two spherical compartments. Center: Submeshes and trial functions for each compartment. Black dots represent trial functions of the respective submeshes. Right: Cut mesh representation created by TPMC. The green and orange colors represent the areas that the trial functions from the previous step are restricted to. Modified from Erdbrügger et al., 2024

Another way to think of the trial functions in CutFEM is by defining submeshes. Each submesh consists of all fundamental elements that contain cut cells of the respective compartment. Each submesh then receives a full set of lagrangian trial functions, cut off at the compartment boundary. These submeshes then naturally overlap but the trial functions of separate compartments only share the boundaries.

See Figure 4.1. for a schematic overview of CutFEMs meshing process. Separating the definition of trial function spaces and head geometry has several advantages. First, the level set function can be created from a variety of segmentation results. Its simple structure imposes no requirements such as nested compartments as is the case for tetrahedrons.

The freedom we have in choosing snippets ensures that the boundary can be approximated accurately. We can also choose to have a low-resolution fundamental mesh with higher-order trial functions while maintaining a high-resolution representation of the head geometry, an option we will explore later on.

Additionally, the fact that we use the same vertex for multiple trial functions implies that CutFEM has an inherently higher density of DoFs near interfaces, automatically spending additional computational resources in areas of high geometric complexity.

It may seem surprising at first that we do not define the trial functions on the snippets. The reason for that is two-fold. First, there are no requirements on the shape of the snippets or how they are connected. The cut mesh contains an arbitrary mix of tetrahedrons and hexahedrons, including hanging nodes, i.e. vertices that are on a corner of one adjacent element and on the face/edge of another. The standard continuous Galerkin from the previous chapter is no longer applicable here and we would have to turn to methods such as Discontinuous Galerkin (DG). DG assigns an individual set of trial functions to each element, cutting them off at the element boundary. DG on

the cut mesh would lead to an unfeasible increase in the total number of DoFs and thus computation time. Second, each fundamental element may be split into dozens of snippets with potentially tiny volumes.

4.2 CutFEM forward problem and Nitsche coupling

The previous section was dedicated to the motivation behind CutFEM, its meshing process, and the associated trial function space. The coming pages are concerned with the mathematical treatment of the discontinuities in V_h.

Rather than thinking of the entire head as one domain, we consider it as the union of disjunct, open subsets of $\mathbb{R}^3$, i.e. $\Omega = \bigcup_i \Omega_i$. We define

$$\Gamma := \bigcup \partial \Omega_i \backslash \partial \bar{\Omega} \tag{4.2}$$

as the internal skeleton of Ω that contains the interfaces between tissues but excludes the scalp surface. The boundary $\partial \Omega_i$ is in practice also approximated by $\partial \bar{\Omega}_i$. For the sake of clarity, we will no longer distinguish between Ω_i and its cut cell approximation in the future.

As mentioned, we use $V_h = \bigoplus V_{h_i}$. Each function $v_h \in V_h$ is therefore well-defined within each of the open sets Ω_i. However, on the internal skeleton Γ it has one value for each adjacent compartment. We define $v_h^i = v_h|_{\Omega_i}$ and quantify the jump of v_h and ∇v_h at an interface location $x \in \partial \Omega_i \cap \Omega_j, i \neq j$ as

$$[\![v_h]\!] = n_i v_h^i + n_j v_h^j,$$

$$[\![\nabla v_h]\!] = <n_i, v_h^i> + <n_j, v_h^j>. \tag{4.3}$$

Here, n_i is the outer unit normal on $\partial \Omega_i$. Therefore, $n_i = -n_j$. Note that the jump of a scalar function is vector-valued, while the jump of a vector-valued function is a scalar. This way of defining jumps will be convenient when deriving the weak CutFEM forward problem. It also allows us to include two necessary requirements in our forward problem. We want both the electric potential and the current density to be jump-free, i.e.

$$[\![u]\!] = 0 \ \text{ on } \ \Gamma \tag{4.4}$$

$$[\![\sigma \nabla u]\!] = 0 \ \text{ on } \ \Gamma. \tag{4.5}$$

The first condition implies continuity of the electric potential over tissue compartments and is fulfilled by default in classical continuous Galerkin, the second is a flux conservation property for the current density. In other words, there may be no current leakage over Γ.

Our CutFEM EEG forward problem then initially lies in finding the electric potential u such that

$$\nabla \cdot \sigma \nabla u = \nabla \cdot j^p \ \textbf{in} \ \Omega \tag{4.6}$$

$$<\sigma \nabla u, n >= 0 \ \textbf{on} \ \partial \bar{\Omega} \tag{4.7}$$

$$[\![u]\!] = 0 \ \text{ on } \ \Gamma \tag{4.8}$$

$$[\![\sigma \nabla u]\!] = 0 \ \text{ on } \ \Gamma. \tag{4.9}$$

In essence, we now have a Poisson-type equation with both exterior and interior boundary Neumann conditions and an interior boundary Dirichlet condition.

Before deriving weak formulations, we define two mesh-dependent helper functions: a weighted and a skew-weighted average. Let E_i, E_j be two cut cells sharing an interface, meaning two cut cells in the same fundamental mesh element. Let

$$\omega_E = \frac{\delta_{E_i}}{\delta_{E_i} + \delta_{E_j}}, \ \delta_{E_i} = n_i^t \sigma^i n_i,$$

where σ^i is the conductivity tensor from compartment i and n_i is again the outer unit normal on $\partial\Omega$. The weighted and skew-weighted averages are then stated as

$$\{v_h\} = \omega_E v_h^i + \omega_J v_h^j$$

$$\{v_h\}^* = \omega_J v_h^i + \omega_E v_h^j.$$

It can be shown that

$$[\![uv]\!] = [\![u]\!]\{v\}^* + \{u\}[\![v]\!],$$

see Nüßing, 2018. Returning to the left-hand-side of (3.6), multiplying with a trial function $v_h \in V_h$ and integrating over Ω, we obtain

$$\int_\Omega \nabla \cdot \sigma \nabla u_h v_h \, dx = -\int_\Omega \sigma \nabla u_h \nabla v_h \, dx + \sum_i \int_{\partial\Omega_i} <\sigma \nabla u_h^i, n_i> v_h^i \, dS. \quad (4.10)$$

Here, we also substituted u for our finite dimensional approximation $u_h \in V_h$.

The integrals over $\partial\Omega_i$ either disappear on the scalp surface or appear twice on interfaces between two compartments, yielding

$$\sum_i \int_{\partial\Omega_i} <\sigma \nabla u_h^i, n_i> v_h^i \, dS = \int_\Gamma \sum_i <\sigma \nabla u_h^i, n_i> v_h^i + \sum_j <\sigma \nabla u_h^j, n_j> v_h^j \, dS$$

$$= \int_\Gamma [\![\sigma \nabla uv]\!] \, dS = \int_\Gamma [\![\sigma \nabla u_h]\!]\{v_h\}^* + \{\sigma \nabla u_h\}[\![v_h]\!] \, dS = \int_\Gamma \{\sigma \nabla u_h\}[\![v_h]\!] \, dS.$$

The above considerations include both Neumann conditions (3.7) and (3.9). To include the Dirichlet condition (3.8), several options exist. We could enforce the conditions strongly by restricting our trial function space V_h to functions that satisfy $[\![v]\!] = 0$ on Γ as was done in Vallaghé and Papadopoulo, 2010. Another way would be to reformulate the problem to a minimization problem with a Lagrangian multiplier (Johnson and Tezduyar, 1999).

The approach we choose here is called Nitsche-coupling, following the work from Nitsche, 1971. As mentioned, CutFEM and discontinuous Galerkin methods share similarities in their definition of trial function spaces. What is known as Nitsche-coupling in CutFEM is similar to interior penalty Galerkin in DG (Di Pietro and Ern, 2012). Hence, we will make use of certain scaling parameters established in DG. We note that $[\![u_h]\!] = 0$

implies that

$$\pm \int_\Gamma \{\sigma \nabla v_h\} [\![u_h]\!] \, dS = 0,$$

$$\alpha \nu_k \int_\Gamma \frac{\hat{\sigma}}{\hat{h}} [\![u_h]\!] [\![v_h]\!] \, dS = 0.$$

We define $\hat{\sigma} = \frac{2\delta_i \delta_j}{\delta_i + \delta_j}$, where $\delta_i = n_i^t \sigma_i n_i$ following Di Pietro and Ern, 2012, $\nu_k = k(k + d - 1)$ scales the penalty term by the polynomial degree of our trial functions (Epshteyn and Rivière, 2007) and $\alpha > 0$ is a free parameter.

Returning to (3.10), we obtain

$$a(u_h, v_h) = - \int_\Omega \sigma \nabla u_h \nabla v_h \, dx + \int_\Gamma \{\sigma \nabla u_h\} [\![v_h]\!] \, dS$$

$$\pm \int_\Gamma \{\sigma \nabla v_h\} [\![u_h]\!] + \alpha \nu_k \int_\Gamma \frac{\hat{\sigma}}{\hat{h}} [\![u_h]\!] [\![v_h]\!] \, dS.$$

The first added term ensures that our final bilinear form is (non-) symmetric in u_h, v_h. A sufficiently large $\alpha > 0$ balances the weighted averages to enforce coercivity (Erik Burman and Peter Hansbo, 2012). If we chose the non-symmetric version, coercivity does not depend on the size of α, but the resulting stiffness matrix is no longer symmetric.

4.3 Ghost-penalty stabilization

Before we state the full EEG/tDCS forward problem for CutFEM, small/misshapen cut cells must be addressed. We stated previously that the snippets may have arbitrary shapes as they only serve as an integration domain. This holds with one exception. If the interface between two tissues almost coincides with an element boundary in the fundamental mesh, one of the resulting cut cells may then have almost zero volume, i.e. consisting only of tiny snippets. Then the entire set of DoFs for that cut cell operates only on that tiny volume, deteriorating the condition number of the stiffness matrix and therefore the numerical stability and computational performance of the algorithm.

To alleviate this, another penalty term is added, stabilizing the derivatives of the trial functions. We define by

$$\hat{\Gamma} = \bigcup \{\partial E_i : E_i \in \mathcal{T}_h, E_i \cap \Gamma \neq 0\} \tag{4.11}$$

the internal skeleton of the fundamental mesh, restricted to those elements that are cut by an interface. Note the difference between Γ and $\hat{\Gamma}$. Where Γ operates on tissue interfaces, $\hat{\Gamma}$ operates strictly on the boundary of the fundamental mesh elements. By adding the penalty term

$$a^G(u_h, v_h) = \gamma_G \sum_{j \leq k} \int_{\hat{\Gamma}} \hat{h} [\![\sigma \partial_n^j u_h]\!] [\![\partial_n^j v_h]\!] \, dS, \tag{4.12}$$

we couple the derivatives of the DoFs of one cut cell to its neighboring cut cells up to the order k that corresponds to the order of our trial functions. Note that this term is no longer consistent with our actual forward problem. The free parameter γ_G has therefore to be chosen carefully. Large enough to stabilize the method but small enough that it does not distort the solution too much. Imagine two neighboring cut cells, one with a small and one with a larger volume. The DoFs in the larger one will be almost unaffected by the added penalty. Stiffness matrix entries associated with DoFs from the smaller cut cell will be dominated by the ghost penalty term. We therefore fixated the boundary values of our trial function and its derivatives up to order k. As the trial function is a kth order polynomial, we therefore fixated the function's behavior inside the entire small cut cell. In other words, the approximation from the larger cut cell is extrapolated onto the smaller one.

Performing the coupling in this manner has several advantages over aggregated methods, where small cut cell contributions are added to larger ones (Badia, Verdugo, and Martín, 2017). One, we do not have to set a strict threshold for which cut cell is considered too small. Additionally, the stabilization is transitory in the sense that if a small cut cell is only surrounded by other small cut cells, these are in turn stabilized by their neighbors. So long as we have sufficiently large cut cells at some point in all directions, each small cut cell will be stabilized. However, in practice, such a scenario would probably be a segmentation artifact.

A central advantage of the ghost penalty stabilization is that it renders the condition number of the stiffness matrix independent of the way the level set cuts the fundamental mesh (Burman, 2010). Another way to think of the impact of the ghost penalty stabilization is to consider the overlapping parts of the trial functions that were cut off at the compartment boundaries. It can be shown that the ghost penalty ensures coercivity not only over the physical domain Ω but also over the overlapping off-cuts (Burman, 2010).

For first-order trial functions the ghost penalty term is straightforward to implement, for higher order, we use the following modification from Preuß, 2018. Let C_1, C_2 be two cut cells sharing a fundamental element border F. A trial function v_h has a dent at the border F, where we transition from one set of non-zero polynomial basis functions to another. Rather than transitioning from one set of basis functions to another, we can also extrapolate the polynomial functions from C_1 onto C_2, denoted by $\hat{v}_h^1$. Similarly, $\hat{v}_h^2$ denotes the basis from C_2 extrapolated onto C_1. Then in Preuß, 2018, it was shown that

$$\int_F \hat{h} [\![\sigma \partial_n^j u_h]\!] [\![\partial_n^j v_h]\!] \, dS \geq 2C ||u_h - \hat{v}_h^2||_{C_1} + ||\hat{u}_h^2 - v_h||_{C_2},$$

for some constant $C > 0$ that only depends on the shape of the fundamental mesh and k. These extrapolated functions give us a unified way of computing a^G for polynomials of arbitrary degree k.

The final EEG CutFEM forward problem is then stated as

Definition 4.1. *CutFEM EEG forward problem*
   Let $\Omega = \bigcup_i \Omega_i$ be an open subset of $\mathbb{R}^n$, σ the 3×3 symmetric, positive definite conductivity tensor.

The weak CutFEM EEG forward problem is then stated as calculating the electric potential $u_h \in V_h$ such that

$$a(u_h, v_h) + a^G(u_h, v_h) = l(v_h) \quad \forall v \in V_h, \tag{4.13}$$

with

$$l(v) = \int_\Omega f v \, dx.$$

This again leads to a linear equation system $A^{Cut}\mathbf{u} = b$, with

$$A^{Cut}_{i,j} = -\int_\Omega \sigma \nabla \phi_i \nabla \phi_j \, dx + \int_\Gamma \{\sigma \nabla \phi_i\} [\![\phi_j]\!] \, dS$$

$$\pm \int_\Gamma \{\sigma \nabla \phi_j\} [\![\phi_i]\!] + \alpha \nu_k \int_\Gamma \frac{\hat{\sigma}}{\hat{h}} [\![\phi_i]\!] [\![\phi_j]\!] \, dS + \gamma_G \sum_{j \leq k} \int_{\hat{\Gamma}} \hat{h} [\![\sigma \partial_n^j \phi_i]\!] [\![\partial_n^j \phi_j]\!] \, dS$$

The functions ϕ_i, ϕ_j are the basis functions from V_h.

CutFEM does not change the applicability of transfer matrix approaches, hence the tDCS and MEG problems can be solved using A^{Cut} in the same manner as was stated in the previous section. Note that the transfer matrix approaches as we use them here assume symmetric A-matrices, which does not hold when using the non-symmetrical CutFEM version.

There is a range of approximation property results for CutFEM in various settings for different types of PDEs, stating the aforementioned coercivity, estimates for how well functions can be approximated in the discontinuous trial function space, optimal convergence with respect to mesh size, and a-posteriori error estimates for $||u - u_h||$. Yet most of these results have regularity requirements such as $u \in H^2(\Omega)$, which we do not have due to the singularities present in both EEG/MEG and tDCS forward problems. We therefore do not explicitly state these results here but refer the reader to Burman, 2010; Erik Burman and Peter Hansbo, 2012; Burman et al., 2015; Sticko, 2018.

A note on source models

The source models we introduced in the previous chapter can easily be modified for CutFEM. For the Venant and partial integration approach we have to evaluate $v_h, \nabla v_h$ either at the location of the source or at a set of monopole positions. So long as these are not located on the internal skeleton Γ, the resulting right-hand side vectors remain well-defined. For the Venant approach, we have to decide where to place the monopoles that approximate the source term. As the fundamental mesh may have a rather low resolution, selecting its vertices as locations for the monopoles may be unstable. Rather, the locations are selected based on a second-order Gauss-Legendre quadrature rule over the gray matter cut-cells of all fundamental elemtents that surround the source position. The definitions for b from the previous sections therefore remain valid for CutFEM. For the full subtraction, identical considerations lead to a separate equation for the correction potential u^c.

CutFEM and discontinuous Galerkin

As mentioned, the Nitsche penalty in CutFEM is similar to the interior penalty methods in discontinuous Galerkin. Where CutFEM performs the cut-off at the tissue boundary, DG methods do so at the element boundary. Implemented into DUNEuro is another approach that combines the two, the unfitted discontinuous Galerkin approach (UDG) (Nüßing et al., 2016). It performs the same cut-off as CutFEM, but the underlying trial function space on the fundamental mesh is that of a discontinuous Galerkin method. Also, no ghost penalty is applied, but small cut cells are scaled to a bounding box that contains them. We will compare CutFEM and UDG in the next chapter.

4.4   Conclusion

This concludes the theory and motivation of CutFEM. In the coming chapters, we will discuss how to turn segmentation results into level sets and investigate CutFEM's performance in a set of gradually more realistic head models, from symmetric multi-layer sphere models to epilepsy patients with multiple tissue defects.

Chapter 5

Head model creation

Before proceeding with numerical investigations in both spherical and realistic head models, we want to give a brief overview of how the hexahedral CG-meshes and the level sets for CutFEM that are used throughout this thesis are created.

5.1 MRI data and segmentation output

The anatomical information for the realistic head models both in the group study in Chapter 7 as well as the epilepsy patients in the final chapters is acquired from MRI images. The only exception here is one of the epilepsy patients whose skull was modeled using computer tomography.

For both subject groups, we measure T1- and T2-weighted (T1w/T2w) MRIs. The MR sequences can be found in the respective chapters. T1 images, in particular MP-RAGE sequences, are excellent for distinguishing gray and white matter (Brant-Zawadzki, Gillan, and Nitz, 1992), but both the skull and the cerebrospinal fluid (CSF) have the same dark color, making their interface difficult to segment accurately. On T2 images, the CSF appears bright while both the brain and skull are dark, making it excellent for segmenting the inner skull surface (Nielsen et al., 2018).

By segmentation, we refer to the process of distinguishing between the different tissues present in the MRI. The algorithms used for segmentation differ and can be based on Fuzzy C-means clustering (Chuang et al., 2006), image registration (Ashburner and Friston, 2005), level-sets (Wang et al., 2011), or recently also deep learning (Akkus et al., 2017). There is also a host of toolboxes such as SPM12 (Ashburner et al., 2014), CAT12 (Gaser et al., 2022), FSL (Jenkinson et al., 2002), or Freesurfer (Fischl, 2012) that perform the segmentation step in an automated fashion. Our focus is not on validating or comparing different segmentation algorithms or toolboxes but rather on the integration of a segmentation output into our numerical finite element approach. This output may be provided in the shape of level sets/signed distance functions, tissue probability maps (TPM), binary maps, or surface triangulations. While level sets or signed distance functions are the most convenient for integration into CutFEM, they are not a default output option of any of the above-mentioned toolboxes.

TPMs assign to each voxel of the MRI one number per tissue, typically ranging between 0 and 1, which can be interpreted as the probability that that voxel is e.g. gray matter. As tissue surfaces run through voxels, the value can also be understood as the proportion of that voxel that belongs to the gray matter compartment.

Binary maps state for each voxel whether the voxel belongs to a compartment or not. They can be created by thresholding TPMs, i.e. determining that all voxels with a value higher than e.g. 0.4. belong to compartment x. Binary maps are ideal for creating hexahedral FEM meshes as each voxel can then be interpreted as one hexahedron. Shifting interface nodes then reduces the edgy staircase pattern of hexahedral meshes, leading to an isoparametric, geometry-adapted hexahedral FEM (Wolters et al., 2007).

Surface triangulations can be created e.g. through surface evolution techniques, where one starts with a spherical surface that is then deformed to match the desired tissue surface (Fischl, 2012). Alternatively, the edges of a binary map can be triangulated and subsequently smoothed. Tetrahedral meshes are often created from surface triangulations but can also be created by triangulating hexahedrons (He, Rezaei, and Pursiainen, 2020).

If the segmentation output is not a level set, we have to transform it accordingly. For tissue probability maps, ranging between 0 and 1, we can set a threshold x that is considered the zero-level. This means that the cut through a voxel with the value x will run through the center of that voxel. Contrast that with binary maps, where the thresholding implied that the entire voxel would be considered as inside.

5.2   Level set creation and smoothing

Recall that our level set function is approximated by a multi-linear function that is determined by its values at each voxel center. Therefore, a level set suitable for CutFEM is an array of tuples that determine for each voxel center the signed distance to the tissue surface.

We will now go through the previously stated segmentation outputs and outline how to transform them into level sets.

TPMs are an early and somewhat unrefined segmentation output. They may be noisy and suffer to a lesser extent also from the same staircase effect as binary maps. However, they are the most faithful to the anatomical MRI data. Applying a smoothing algorithm both reduces noise and removes the staircase pattern. The issue with smoothing however, and that applies to the smoothing of all segmentation outputs, is that brain and CSF both have very thin areas, with thicknesses of only a few voxels. In particular, the CSF between two gyral folds or the branching of white matter into a gyral crown are susceptible to smoothing algorithms such as Gaussian or median kernel filters. To smoothen TPMs in an edge-preserving manner, we therefore use an anisotropic diffusion filter based on Perona and Malik, 1990. Binary maps can be turned into smooth signed distance functions by applying an anti-aliasing algorithm such as Whitaker, 2000. The anti-aliasing also reduces the edgy staircase pattern. For surface triangulations, simple algorithms exist to extract signed distance functions from them, the one we used can be found at `https://github.com/christopherbatty/SDFGen`. It is probably more reasonable to apply smoothing to the surface triangulations than to the subsequent level set.

In Figure 5.1., you can see a sagittal slice of the gray matter representation of final FEM meshes, with level sets created from tissue probability maps, level sets from binary maps, a geometry-adapted hexahedral FEM,

a tetrahedral model created with the SimNIBS CHARM toolbox (Saturnino et al., 2019; Thielscher, Antunes, and Saturnino, 2015) as well as the original T1- and T2-weighted MRI slices. The subject was a healthy 27-year-old male. Voxel resolution is 1x1x1 mm, the same as for all MRIs considered in this thesis. The MRIs were recorded using a 3 Tesla MagnetomTrio Scanner with a 32-channel head coil built by Siemens (Siemens, Munich, Germany). The T1w was acquired from a fast gradient-echo pulse sequence (TFE) with water-selective excitation to avoid fat shift (TR/TE/FW = 2300/3.51 ms/8°, pre-pulse inversion with TI = 1.1 s). The T2 was measured using a turbo spin echo pulse sequence (TR/TE/FA = 3200/408 ms/90°).

The MRIs were segmented using CAT12 (Gaser et al., 2022) with default parameters. The tissue probability maps were thresholded at a value of 0.2. The T1 was used for the distinction between gray and white matter, and the T2 to delineate the CSF/gray matter interface. The geometry-adapted hexahedral mesh was then created with a node-shift of 0.33 using the SIMBio Vgrid toolbox `http://www.mrt.uni-jena.de/simbio`. The binary map level set was anti-aliased in ITK (Yoo et al., 2002) to a maximum RMS-change value of 1e-7. The TPM-based level set was also thresholded at a value of 0.2 and then smoothed using the Matlab function *imdiffusefilt* with a gradient threshold of 1.9 and 2 iterations. The SimNIBS Charm pipeline was run with default parameters.

Notice the clear white matter/gray matter contrast in the T1 image and the contrast between gray matter/CSF in the T2 image. Two different defects can be seen to different extents in all 4 FEM meshes. First, an inflated gray matter pushes the CSF out of the sulci. This is most present in the anti-aliased level sets created from binary segmentations and least in the tetrahedral mesh, where there may even be an overestimation of CSF. Secondly, fine white matter branches do not reach up to the gyral crowns. This effect is very pronounced in the tetrahedral mesh, where also the white matter in the cerebellum is represented very coarsely.

Overall the level set based on tissue probability maps is in this comparison the most faithful representation of the anatomical MRI data. This may be because all other approaches use binary maps. The transition from TPM to binary map marks a loss of information that, in the subsequent smoothing, may lead to additional inaccuracy. We will therefore use TPMs to create gray and white matter masks for our realistic volume conductor models. Note however that this comparison is by no means complete. Smoothing is heavily parameter-dependent and it may be that the presented defects differ significantly when switching subjects or optimizing the smoothing/segmentation parameters. The presented algorithms only serve as an orientation on how one might create level sets usable for CutFEM.

5.3   Three- and six-compartment realistic head models

In the previous section, we stated how to create the level sets needed for CutFEM. Now, we want to focus on how to properly recombine the outputs for different tissues into fully realistic head models.

The MRIs that are used for the realistic models all have a voxel resolution of 1x1x1 mm. Hence, all our models, including spherical ones, are scaled to
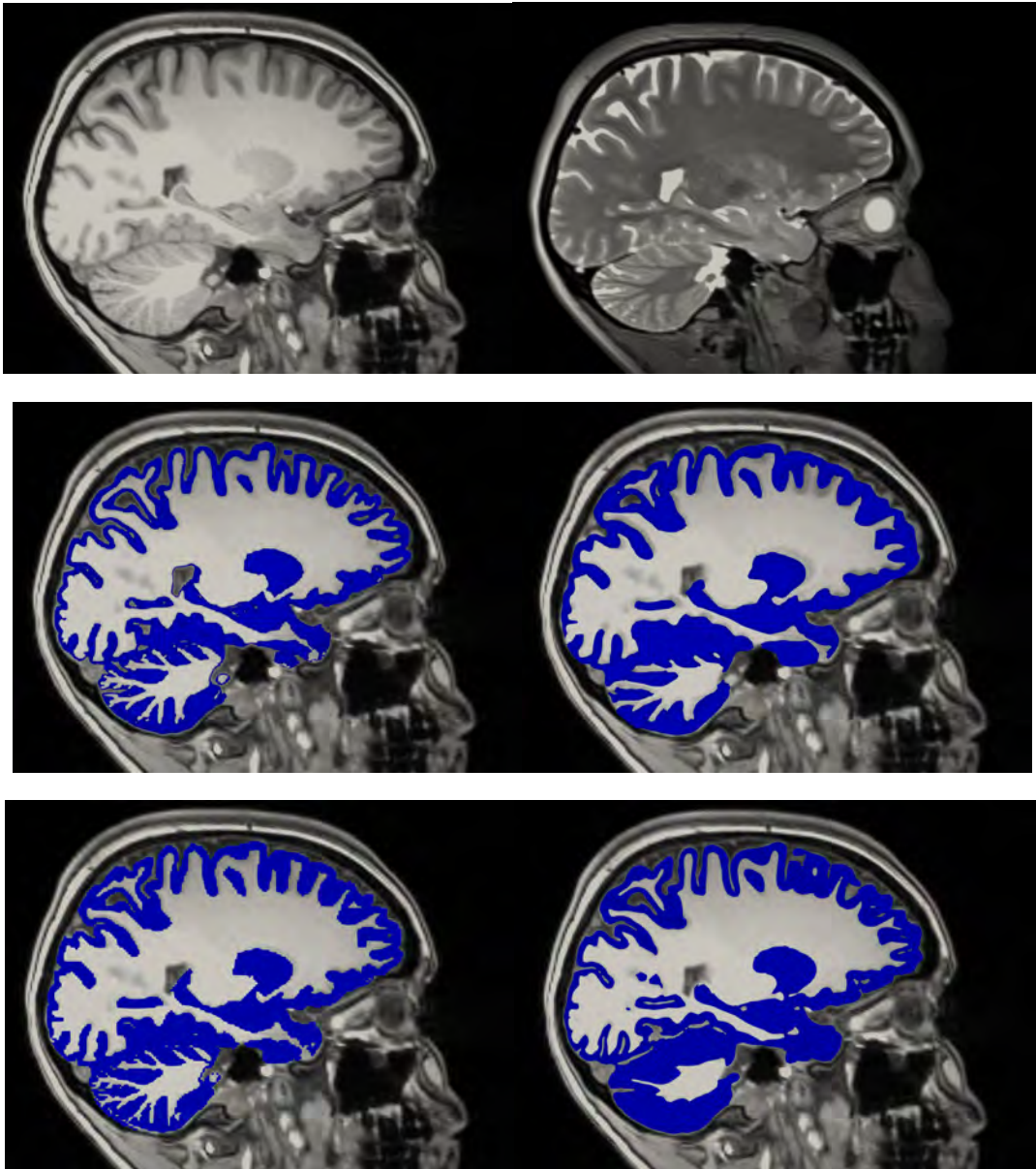
FIGURE 5.1: Sagittal T1w and T2w MRI scans and gray matter representations in different finite element meshes. Top row: T1-weighted MRI on the left and T2-weighted MRI on the right. Center row: CutFEM model created with level sets based on tissue probability maps (left) and binary maps (right). Bottom row: Geometry adapted hexahedral mesh on the left and SimNIBS Charm (Thielscher, Antunes, and Saturnino, 2015) tetrahedral mesh on the right.

approximately 1 mm resolution. For CutFEM, this means that when we use a 2 mm background mesh we refine the cut mesh once, and twice, if a 4 mm mesh is selected. The hexahedral models will have an initial side-length of 1 mm and tetrahedral meshes an average volume of 0.33 mm^3 per element. In this thesis, tetrahedral meshes are only used for the spherical models, while hexahedral models will always to some degree include MRI segmentation results.

In the chapters with realistic models, we will usually compare a six-compartment CutFEM model, a six-compartment geometry-adapted hexahedral FEM model, and a three-compartment boundary element method (BEM) model. We start by describing the head model generation process for the hexahedral FEM. It is based on Antonakakis et al., 2019; Aydin et al., 2014.

The six compartments we distinguish between are scalp, skull compacta [SC], skull spongiosa [SS], CSF, gray matter [GM], and white matter [WM]. They are based on the T1 and T2 images. The T2 is registered onto the T1 using FSL FLIRT (Jenkinson et al., 2002), and the tissue segmentation is done using CAT12 (Gaser et al., 2022). The T1 is used for gray matter, white matter, and scalp while CSF and skull compacta are segmented from the T2. The spongiosa mask was created by performing Otsu thresholding (Otsu, 1979) on the skull compacta mask that was eroded by 2 mm. Overlap of the skull and CSF or the brain tissues was removed and unrealistic holes within the masks were detected and filled using the *imfillfunction* in MATLAB. Segmentation holes and tiny fragments of the skull or scalp were removed using Matlab internal functions. Following the recommendations of Lanfer et al., 2012, the model was cut 4 cm below the skull using an axial plane. From the segmentations, geometry-adapted hexahedral meshes with a node shift of 0.33 were created (Wolters et al., 2007).

The CutFEM level sets for gray and white matter are based on tissue probability maps of the T1. Using TPMs for the skull was considered too unreliable, as thin skull areas with low contrast, especially near the temples often lead to unrealistic cranial holes in the level sets. Instead, we use the binary skull mask that was also used for the hexahedral model as a basis for our level set creation. To avoid empty spaces inside the cranium, the CSF level set is also based on a binary mask that contains the entire inside of the skull. Note that this process ensures an accurate pial and inner skull surface. For the scalp, no significant differences between TPM-based and binary map-based level sets were observed. We therefore used the binary map from the hexahedral model as the applied hole filling eliminates the possibility of empty spaces between the skull and scalp. Exemplary coronal slices of the hexahedral FEM and the CutFEM model can be seen in Figure 5.2.

For the BEM model, skin, skull, and brain surfaces have to be specified. They were created from the 6-compartment model to ensure maximum comparability between the methods. The brain was defined as the union of gray matter, white matter, and CSF, and the skull as the union of compacta and spongiosa. Surfaces are extracted using the fieldtrip (Oostenveld et al., 2011) function *ft_prepare_mesh*.
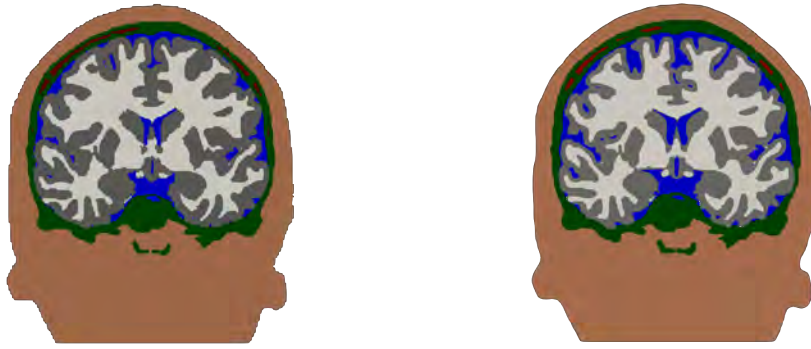
FIGURE 5.2: Realistic six-compartment geometry-adapted hexahedral FEM (left) and CutFEM model (right). Tissues include white matter (white), gray matter (gray), cerebrospinal fluid (blue), skull compacta (green), skull spongiosa (red), and scalp (brown).

5.4   Calculating CutFEM lead fields in DUNEuro

As mentioned, CutFEM is implemented into DUNEuro, see Schrader, 2022 for a detailed installation description. Alternatively, collaborations with other software toolboxes such as Brainstorm exist (Medani et al., 2023). The pipeline to create the six-compartment hexahedral FEM lead fields, the skull conductivity calibration, and the tDCS optimization has been uploaded to Zenodo, see `https://zenodo.org/doi/10.5281/zenodo.11066431`. It covers descriptions and code ranging from MRI registration, segmentation, anisotropic white matter tensors, source space creation, sensor-to-head registration, mesh generation, lead field generation, skull conductivity calibration, and subsequent D-CMI-based tDCS optimization.

Additionally, updated configuration files for the installation of DUNEuro can also be found on Zenodo, as well as an exemplary script to create level sets and CutFEM lead fields. The level set creation script deviates from the description in Chapter 4 in one detail. Rather than using anti-aliasing for the creation of the skull and scalp mask, the script uses diffusion anisotropy smoothing as well. This was done to keep the level set creation contained in MATLAB. The resulting differences were negligible in two test cases.

We demonstrated the creation of level sets based on realistic anatomical data. As shown, level sets can be created from a variety of segmentation inputs, highlighting CutFEM's versatility as any combination of tissue probability maps, binary segmentations, and surface triangulations can be used. In particular, the use of tissue probability maps shows promise in modeling details in the millimeter range.

CutFEM allows for arbitrarily touching skull and brain surfaces, accurately modeling the vanishing CSF. As the brain moves inside the skull depending on whether the subject sits, or lies supine/prone, we can therefore consider the positioning of a subject during EEG/MEG measurement as a parameter in our analysis. In Justin K. Rice et al., 2013, it is stated that the CSF thickness in occipital areas, measured in the MRI, differs by thirty percent when moving from supine to prone positioning. Recorded occipital EEG amplitudes changed by up to eighty percent.

Chapter 6

Numerical sphere model studies

The previous chapters have motivated CutFEM and described the process of creating suitable level set functions. In this chapter, we calculate FEM-based EEG/MEG lead field matrices and tDCS current densities for spherical head models. As mentioned in Chapter 2, spherical head models have the advantage of the existence of (quasi-)analytical solutions that serve as reference solutions. While they are only inaccurate approximations of the human head and its tissues, they are still widely used for the initial validation of new forward modeling approaches (Cuartas Morales et al., 2019; Mosher, Leahy, and Lewis, 1999a).

The comparisons we perform here have three dimensions. First, we distinguish between two sphere models, one concentric multi-layer sphere model and another that includes semi-realistic brain tissues. Secondly, we calculate forward solutions for EEG, MEG, and tDCS, and lastly, the numerical methods to solve the forward problems will be CutFEM and CG-FEM in addition to the quasi-analytic reference solution.

6.1 Concentric and semi-realistic sphere models

Our basic spherical head model consists of four concentric layers, including skin, skull, cerebrospinal fluid (CSF), and brain. Radii and standardized electric conductivities for the four layers can be found in table 6.1.

In addition to the concentric sphere model, we extracted realistic gray and white matter from the same 27-year-old subject mentioned in the last section of the previous chapter. A minimal bounding sphere of CSF with a radius of 91.03 mm and additional scalp and skull layers of 6 mm thickness each were placed around the brain tissues, resulting in a total of 5 layers. Skin and skull use standard conductivities, but the 3 inner layers, white matter, gray matter, and CSF were assigned the same conductivity value. From a volume

	Concentric spheres		Semi-realistic spheres	
	Radii (mm)	S/m	Radii (mm)	S/m
White	-	-	-	0.33
Gray	78	0.33	-	0.33
CSF	80	1.79	82.63	0.33
Skull	86	0.01	88.63	0.01
Skin	92	0.43	94.63	0.43

TABLE 6.1: Radii and conductivities for sphere models
Radii and conductivities for 4-layer concentric sphere and semi-realistic 5-layer sphere models.

conduction perspective, we therefore only have a concentric 3-layer sphere model where we also have quasi-analytical reference solutions.

For comparison, we use a geometry-adapted hexahedral model with a node shift of 0.33 (Wolters et al., 2007). The CutFEM level sets for gray and white matter are calculated from tissue probability maps, and the sets for the spherical CSF, skull, and scalp layer are based on Anti-aliasing (Whitaker, 2000).

This additional model is another step towards the realistic head model. For CutFEM, it is interesting for two reasons. First, the level sets in the standard sphere model can be calculated analytically, up to arbitrary precision. In this semi-realistic sphere model, we can investigate whether our process of creating tissue probability maps based on level set functions interferes with the accuracy of our numerical solution. Additionally, the standard sphere model has a large brain area where the fundamental cells are not cut by level sets. We can therefore investigate whether CutFEM incurs instabilities when almost all fundamental cells are cut and stabilized, as is the case in a realistic head model.

EEG/MEG

As sensor locations, we place 200 evenly spaced electrodes onto the scalp and 256 evenly spaced MEG coils at a distance of 18 mm around the outermost sphere. For the MEG the orientation of the coils is of importance, hence we compute the flux of the secondary magnetic field in all three spatial directions, yielding a total of 768 MEG channels. As EEG/MEG source locations, we place 50000 uniformly spread points into the brain compartment. The semi-realistic sphere model uses 16686 sources located inside the gray matter compartment and spaced 2 mm apart. From the literature, it is known that errors for all modalities increase for decreasing distance to the next conductivity jump (Wolters et al., 2008). Hence, we group the sources by eccentricity. An eccentricity of 0 implies that the source is at the center of the sphere model, a value of 1 means that the source is on the brain/CSF interface. Physiologically, the cortical gray matter has a thickness of 1-4 mm (Fischl and Dale, 2000). The pyramidal cells which are primarily responsible for the EEG/MEG fields are located in layer 5 of the gray matter. Hence, the most realistic sources have a distance of 1-2 mm from the closest conductivity jump, corresponding to an eccentricity of 0.96-0.98 in our model.

In addition to grouping sources by eccentricity, we have to distinguish them by source orientation. In the MEG, a dipole moment that points radially outward from the sphere induces no magnetic field outside the volume conductor, hence we only consider tangentially oriented MEG sources. For the EEG, we distinguish between radial and tangential sources.

Quasi-analytical solutions for the EEG are computed in fieldtrip (Oostenveld et al., 2011) based on the formulas derived in Munck, Peters, et al., 1993. The MEG reference solutions are based on Sarvas, 1987. As error measures, we use the relative difference measure (RDM) and the magnitude error (MAG). For analytical and numerical solutions $u_{ana}, u_{num} \in \mathbb{R}^s$, they are defined as

$$RDM(u_{ana}, u_{num}) := 50 \left\| \frac{u_{num}}{||u_{num}||_2} - \frac{u_{ana}}{||u_{ana}||_2} \right\|_2, \qquad (6.1)$$

$$MAG(u_{ana}, u_{num}) := 100(\frac{||u_{num}||_2}{||u_{ana}||_2} - 1). \tag{6.2}$$

The MAG measures differences in total signal strength in percent. However, it is blind to differences in the signal distribution across channels. The RDM ignores amplitude differences by normalizing the signals and then comparing their across-channel difference in signal distribution. It is normalized to values between 0 and 100.

tDCS

For tDCS we employ the same sphere models but only use two electrodes at opposite sites of the spheres. With tDCS, we are not limited to evaluating the electric field at gray matter locations but can investigate the spread of errors throughout the entire head model. For the semi-realistic model, this means that we can trace whether errors accumulate near interfaces irrespective of the eccentricity.

Quasi-analytic solutions are calculated from Ferree, Eriksen, and Tucker, 2000. As point-wise error measures, we quantify the angle and the magnitude difference between quasi-analytical and numerical electric field vectors.

$$MAG(E_{ana}, E_{num}) =:= 100(\frac{||u_{num}||_2}{||u_{ana}||_2} - 1), \tag{6.3}$$

$$ANGLE(E_{ana}, E_{num}) := acos(\frac{< u_{num}, u_{ana} >}{||u_{num}|| \cdot ||u_{ana}||} \tag{6.4}$$

FEM models

The level set functions for the standard concentric sphere model are calculated directly as distance to the center of the sphere minus the radius of the respective tissue. The gray and white matter level sets in the semi-realistic case are calculated from tissue probability maps, see the previous chapter for more information. For Cutfem, we use two variants for both sphere models. A 2 mm fundamental mesh with first-order trial functions and a 4 mm resolution with second-order functions. The 2 mm model has been refined once, and the 4 mm model twice to simulate a 1 mm MRI resolution. For the second-order trial functions, we additionally distinguish between partial integration and Venant lead field matrices.

For comparison in the concentric sphere model, we additionally calculate a lead field from a 4 mm unfitted discontinuous Galerkin approach and a tetrahedral mesh with an average element size of $0.3 \, mm^3$ volume. In the semi-realistic case, we compute a lead field from a 1 mm geometry adapted hexahedral mesh with 0.33 node-shift.

Degrees of Freedom and the number of cut cells/mesh elements can be found in Table 6.2. We see that a 2 mm first-order CutFEM uses a similar number of DoFs as a 4 mm second-order CutFEM/first-order UDG approach. We use a higher number of DoFs in the CG approaches to match the post-refinement mesh resolution of CutFEM/UDG. All calculations are performed using the DUNEuro toolbox (Schrader, 2022).

		DoF	Elements/Cut cells	Snippets
	Tetrahedral FEM	1,714,016	10,697,673	-
Concentric spheres	CutFEM Q1	636,560	521,935	2,957,877
	CutFEM Q2	732,927	77,512	3,236,136
	UDG	620,096	77,512	3,236,136
	Hexahedral FEM	4,651,409	4,551,183	-
Semi-realistic spheres	CutFEM Q1	986,769	660,723	5,565,445
	CutFEM Q2	1,170,340	123,250	6,882,743

TABLE 6.2: Number of degrees of Freedom, cut cells and snippets for Cut-FEM. DoF and mesh element numbers for hexahedral/tetrahedral meshes.

6.2 Results in the concentric multi-layer sphere model

EEG

EEG RDM and MAG errors for both radial and tangential source orientations can be found in Figure 6.1. We see that for all three CutFEM variants (first order trial functions with venant source model, second order with both venant and partial integration) all error categories remain below 1 percent MAG and 0.5 percent RDM. The UDG in turn reaches outlier values of more than 3.1 percent RDM and 9.44 percent MAG. The maximal errors resulting from the tetrahedral FEM approach are 2.32 percent RDM and 2.42 percent MAG. The absolute differences between the different CutFEM approaches are small but in the physiologically most relevant eccentricity categories 0.96-0.98, the second-order CutFEM approach with the partial integration approach yields 10.1 percent lower average MAGs and 22.7 percent lower average RDMs than when using the venant source model. Switching from first-order CutFEM with Venant source model to second-order CutFEM with partial integration source model reduces MAGs by 18.5 percent and RDMs by 52.5 percent. Differences between radial and tangential source orientations are negligible.

MEG

The MEG results can be found in Figure 6.2. Note that we only investigate the error of the secondary part magnetic field as the primary is calculated directly. Also, only tangential source orientations are considered as radial sources would produce neither primary nor secondary B-field components at the sensors. Qualitatively, the same statements as for the EEG hold. The UDG in turn reaches outlier values of more than 8 percent RDM and 10 percent MAG. The maximal errors resulting from the tetrahedral FEM approach are 2.15 percent RDM and 3.07 percent MAG. The main difference to the EEG is that UDG now performs worse than tetrahedral FEM also in the eccentricity groups from 0.96- 0.98.

tDCS

For tDCS, we split the errors in angle and Magnitude errors. The advantage we have in tDCS is that in our error analysis, we are not bound to the gray matter source positions, but can also investigate the error distribution in other tissue compartments. The results can be seen in Figure 6.3. Absolute magnitude errors for first-order CutFEM stay below 5 percent in the
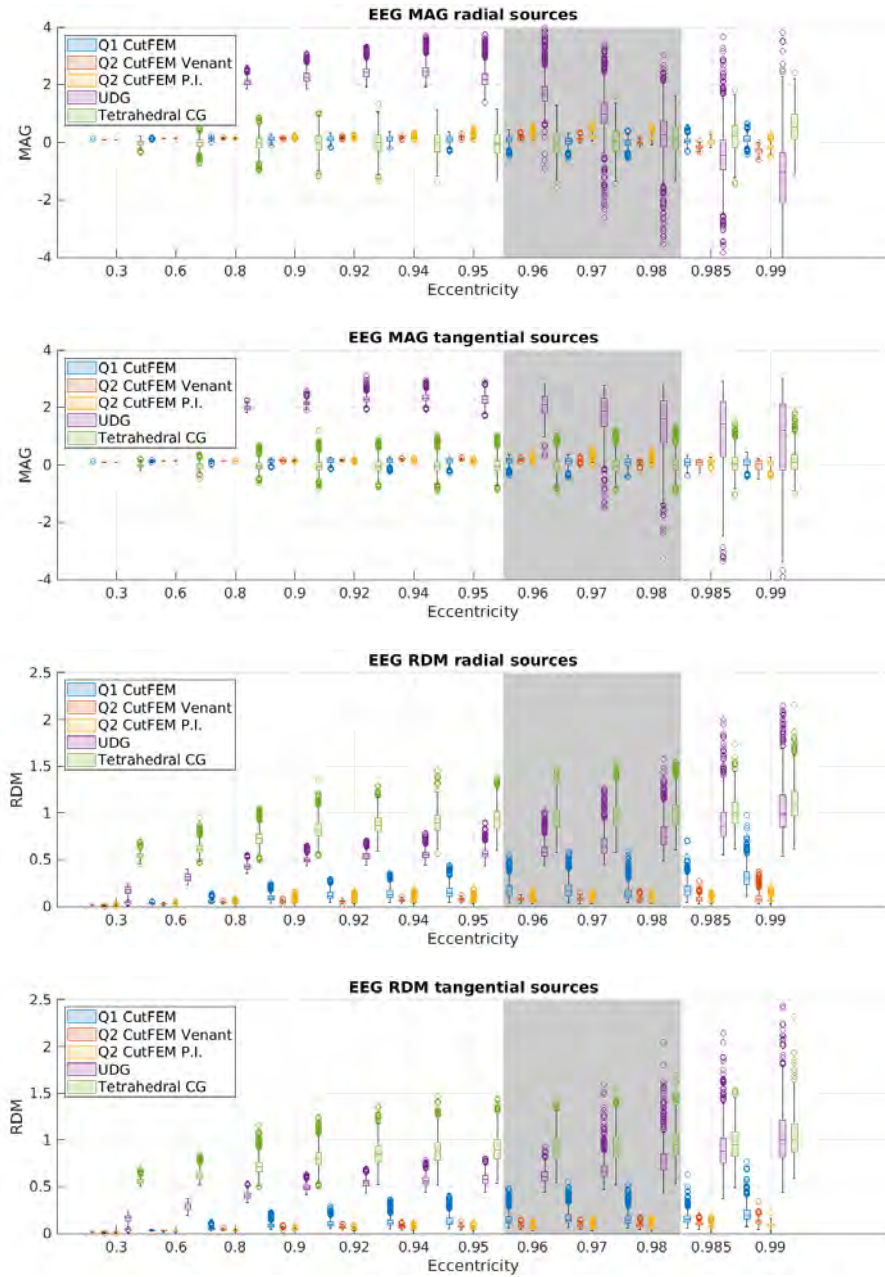
FIGURE 6.1: EEG errors in a concentric sphere model. From top to bottom: MAG errors for radial sources, MAG errors for tangential sources, RDM for radial sources, RDM for tangential sources. Errors are grouped by proximity to conductivity jump (eccentricity). Separate boxplots for first order CutFEM with Venant source model, second order CutFEM with both Venant and partial integration, unfitted discontinuous Galerkin with Venant source model, and tetrahedral CG method with Venant.

FIGURE 6.2: MEG errors in a concentric sphere model. From top to bottom: MAG errors for tangential sources, RDM for tangential sources. Errors are grouped by proximity to conductivity jump (eccentricity). Separate boxplots for first order CutFEM with Venant source model, second order CutFEM with both Venant and partial integration, unfitted discontinuous Galerkin with Venant source model, and tetrahedral CG method with Venant.

FIGURE 6.3: TDCS errors in a concentric sphere model. From top to bottom: MAG errors, Angles. Errors are grouped by proximity to conductivity jump (eccentricity) for brain targets, or compartment. Separate boxplots for first order CutFEM, second order CutFEM, unfitted discontinuous Galerkin, and tetrahedral CG.

eccentricity groups 0.96-0.98, but reach up to 10 percent in CSF and skull compartments. The angles between numerical and analytical current density vectors also remain below 5 degrees in the brain and below 10 in the CSF and skull. UDG is again outperformed by the tetrahedral FEM. Tetrahedral FEM and first-order CutFEM perform similarly, with CutFEM featuring on average 49.8 percent lower angles and 26.4 percent lower Magnitude errors. This trend however decreases for higher eccentricities and for CSF and skull, both methods perform similarly. Second-order CutFEM outperforms all other methods throughout all eccentricity groups. Its angles remain comfortably below 2 degrees and brain magnitude errors below 3 percent.

Moving forward to our semi-realistic sphere model, 2 simplifications to our study are made. Second order CutFEM so clearly outperforms UDG at 4 mm fundamental mesh resolution that we no longer consider UDG in the semi-realistic scenario. Also, we no longer feature second-order CutFEM with the Venant source model as it was slightly outperformed by the partial integration version.

6.3   Results in the semi-realistic sphere model

In the semi-realistic sphere model, our source space is limited to the realistic gray matter compartment. As we have a three-layer volume conductor here, the first conductivity jump is the brain-skull-interface. This greatly reduces the number of points in the higher eccentricity groups as there are only a few places where realistic gray matter and the spherical skull layer intersect. Hence, all 205 points with eccentricity equal to or larger than 0.98 were combined into one group. Note that with this study, our interest is not primarily in the behavior at high eccentricities, but rather whether the use of realistic level sets deteriorates our numerical accuracy in CutFEM.

MEG

We start with the MEG, the results can be found in Figure 6.4. Overall, most results from the previous section also hold here. First-order CutFEM is slightly outperformed by second-order and slightly outperforms the continuous Galerkin FEM approach that uses geometry-adapted hexahedrons in this scenario. Median errors differ slightly when compared to the 4-layer sphere model from the previous section. CutFEM Q1 relative error increases are less than 43 percent, Q2 CutFEM less than 39 across all eccentricity groups, and RDM/MAG. CutFEM RDM and MAG both stay below 1 percent for both first and second-order trial functions. Noticeably, there are more and higher outlier values in lower eccentricity groups, where before error values typically ranged below 0.1 percent RDM/MAG. This is however also the case for the hexahedral FEM approach, where RDMs reach up to 2.5 percent.

tDCS

As mentioned before, we can investigate the error dynamic throughout the volume conductor. This is visualized over a grayscale image of the volume conductor in Figure 6.5. For all three methods, high angles of 5 degrees or more can only be observed in the skull layer. In the brain, angles reach their

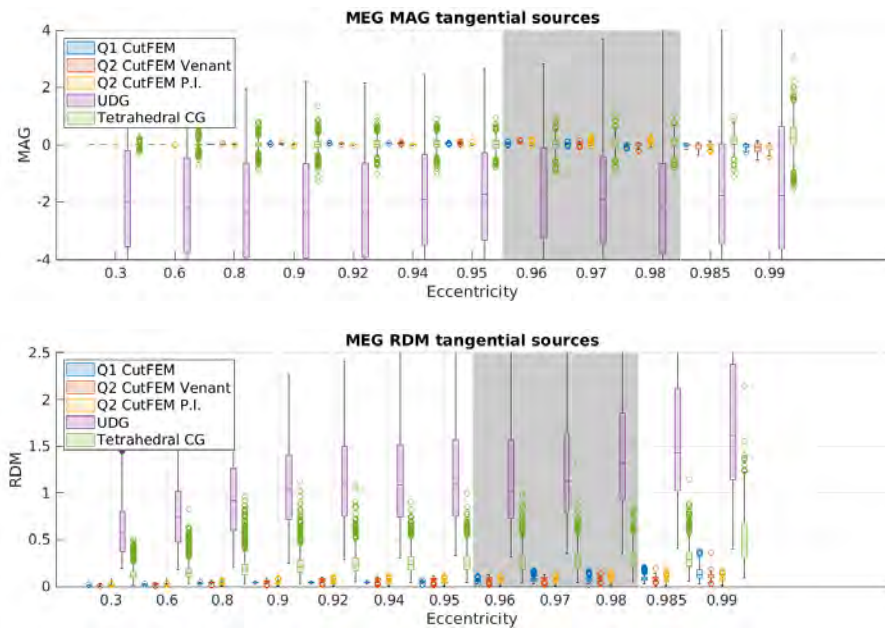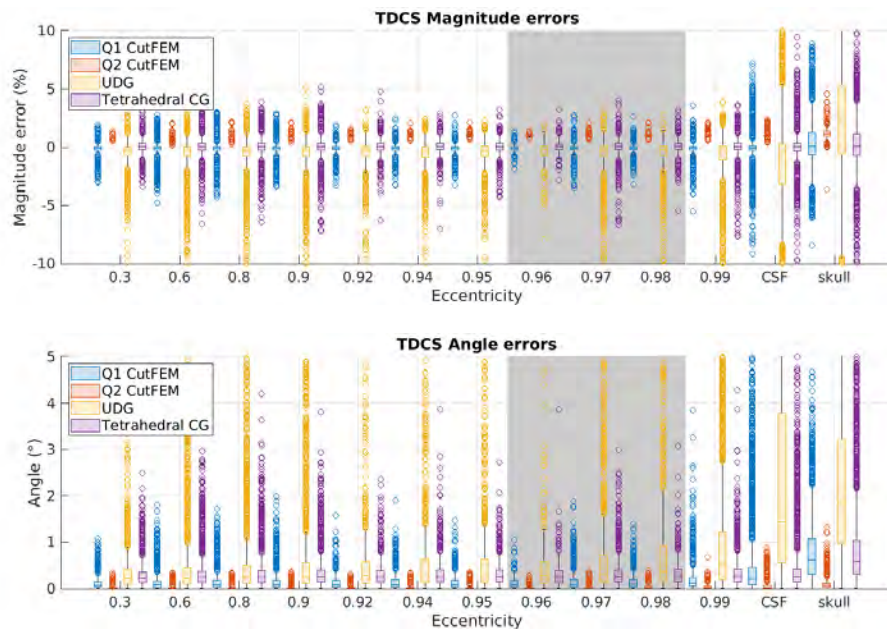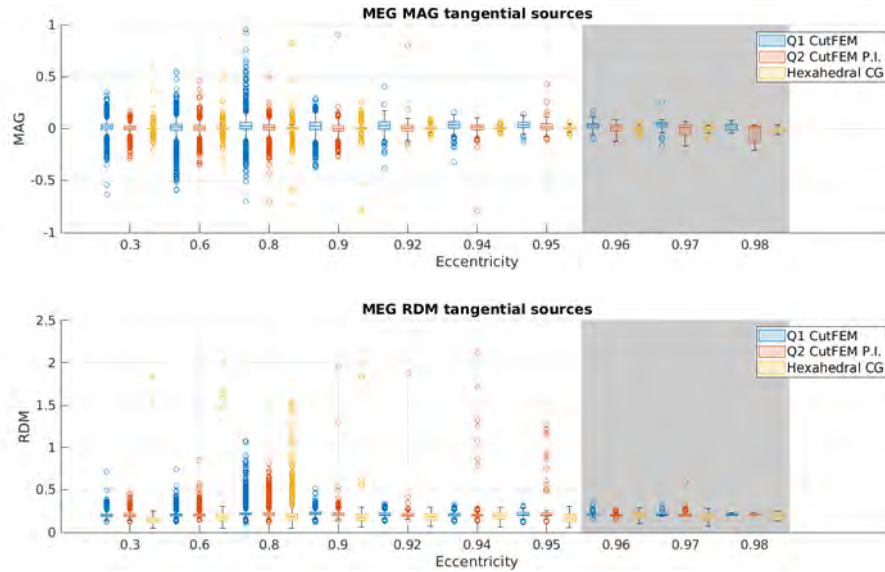FIGURE 6.4: MEG errors in a semi-realistic sphere model. From top to bottom: MAG errors for tangential sources, RDM for tangential sources. Errors are grouped by proximity to conductivity jump (eccentricity). Separate boxplots for first order CutFEM with Venant source model, second order CutFEM with partial integration, and hexahedral CG method with Venant.

maximum at 2.5 degrees near the electrodes and decrease with increasing distance to the electrodes. The spread of errors into the brain is slightly higher for second-order CutFEM than for the other two approaches, making this the first investigation where second-order CutFEM does not outperform all other methods. The distance to the electrodes is for all three methods the determining factor, not whether the evaluated point lies near the boundary of a realistic tissue compartment. This can be seen more clearly when looking at the magnitude differences between analytic and numerical solutions. The overall results are in a similar range as in the concentric sphere model, and the highest errors are again inside the skull and near the electrodes. The color scale is chosen in a manner such that the contrasts in the interior parts of the brain can be seen more clearly. We see that the MAG distribution in the CutFEM models broadly follows the realistic gray matter compartment. The MAG jumps at an interface are however below 0.5 percent, making this a negligible effect. This effect is not present in the hexahedral FEM model.

The EEG results follow the trends observed in MEG. They have already been published and can be found in Erdbrügger et al., 2023.

6.4 Conclusion

In this chapter, we created the first set of EEG/MEGCutFEM lead fields and compared them to other FEM approaches. The simplified, spherical geometries that were used as volume conductors allowed for the calculation of quasi-analytical solutions as reference.

The first investigations were performed in a standard 4-layer concentric sphere model that included a brain, cerebrospinal fluid, skull, and scalp layer. For EEG/MEG and tDCS, we calculated forward solutions using a first-order trial function CutFEM with the St. Venant source model, and two

FIGURE 6.5: TDCS errors in a semi-realistic sphere model. Left column: MAG errors. Right column: Angles. Top row: Errors for first order CutFEM. Center row: Errors for second order CutFEM. Bottom row: Errors for hexahedral FEM.
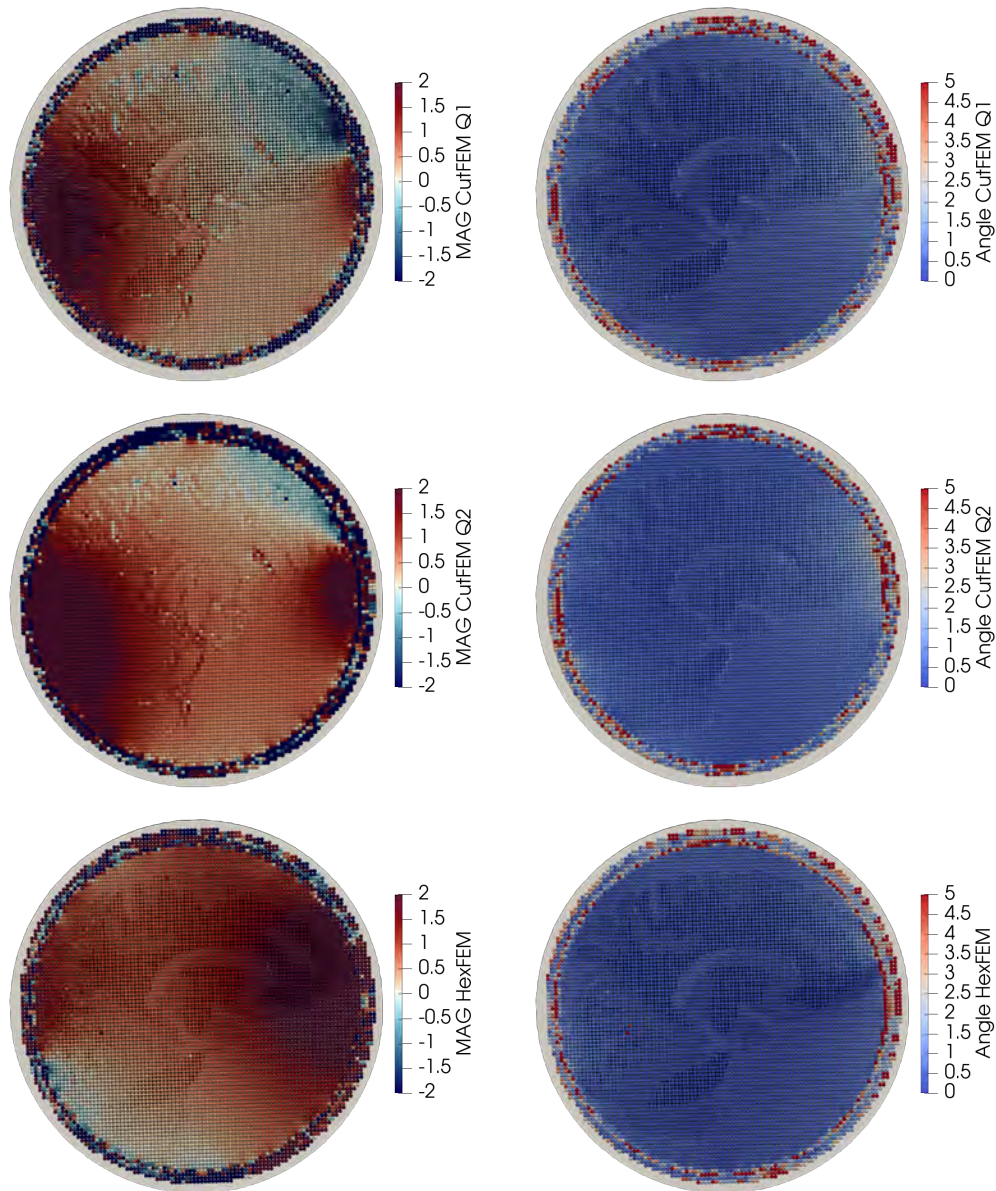
second-order trial function CutFEM approaches, one with the Venant and one with the partial integration source model. As a comparison, we also calculated solutions using an unfitted discontinuous Galerkin method (UDG) that operates on the same cut mesh as the second-order CutFEM approaches, and a tetrahedral continuous Galerkin FEM. The resolution for all methods was chosen in a manner that maintains a comparable number of degrees of freedom. The CG approaches, whose solutions at higher resolution can be calculated more efficiently than CutFEM at this point, were given higher resolutions.

Several key points are apparent from analyzing this first model. First, there is little qualitative difference between analyzing EEG, MEG, or tDCS. This is unsurprising as all use the same stiffness matrix. The difference between EEG and MEG lies only in the right-hand side vector. The EEG transfer matrix is due to Helmholtz reciprocity already the solution to the tDCS forward problem.

Secondly, the UDG results were outperformed by all other approaches, particularly near conductivity jumps. This may be because the current UDG implementation does not use a ghost penalty to stabilize small snippets (Nüßing et al., 2016; Nüßing, 2018).

All CutFEM approaches outperformed the tetrahedral CG approach. In particular, at lower eccentricities, the CutFEM errors were orders of magnitude smaller.

The second-order CutFEM approach with the partial integration source model was the overall most accurate approach. This highlights one of CutFEM's unique advantages, using higher-order trial functions without compromising on the faithfulness to the anatomic data or inflating the number of DoFs. The use of the partial integration source model is simpler to implement and has fewer parameters to optimize than the Venant approach. It is also not an approximation to the dipolar source model as the Venant. The use of second-order trial functions alleviates the PI model's main disadvantage of not being able to distinguish between source positions in the same mesh element.

The first sphere model had the advantage that we could calculate exact level sets for the concentric spheres. To investigate whether this inherent advantage over the CG approaches amounts to an unfair comparison, we created a second sphere model. This 5-compartment model places realistic gray and white matter, segmented from human MRI data, into the center of three concentric spheres, CSF, skull, and scalp. Identical conductivities for the inner three compartments effectively reduced this model to a three-layer concentric sphere model in terms of volume conduction. Compared to the first model, we no longer investigate UDG or second-order CutFEM with the Venant source model. As a continuous Galerkin comparison, we calculated a geometry-adapted hexahedral mesh. This type of mesh will also serve as a reference for the comparisons in fully realistic head models in the next chapters.

We saw that CutFEM still outperforms the CG FEM, albeit less clearly than in the previous model. Additionally, we see several outlier values at lower eccentricities that were not present in the previous model. These outliers were however present in both CutFEM and CG-based forward models. All

outliers ranged below 3 percent RDM/MAG. Looking at the tDCS error distribution showed us that while there are jumps in error magnitude near inner compartment interfaces, these are dominated by errors due to proximity to either the stimulation electrodes or a conductivity jump.

Using CutFEM with realistic level sets therefore does not deteriorate the overall numerical results. The reason for the slightly higher error ranges compared to the first model may be due to the way the spherical compartments were created, possibly leading to sub-millimeter inaccuracies in the shape or radius of the concentric spheres.

However, we did see that the second-order CutFEM approach no longer clearly outperforms the first-order CutFEM. The error distribution in tDCS even showed slightly higher errors in second-order CutFEM. One possible explanation for this is that in a realistic scenario, the 4 mm fundamental mesh cells contain more different cut cells than when using a 2 mm resolution, possibly outweighing the advantage of using higher-order trial functions. Whether this effect is even more pronounced in a fully realistic head model is at this point unclear. For example, a scenario where one fundamental cell contains snippets from two gyri separated by a thin layer of CSF or skull is more likely in a 4 mm model. The same trial functions would then be used for both gray matter snippets but the actual volume conduction would differ strongly in the two gyri. In the following chapters, we will therefore use the first-order CutFEM approach.

Regarding UDG, it may be promising to explore the possibility of adding a ghost penalty to stabilize the method.

One motivation for using discontinuous Galerkin over continuous Galerkin in MEG is a flux conservation property that can be used to calculate the current density $\sigma \nabla u$ (Piastra et al., 2018). In UDG, this may be harnessed as well and could motivate its use over CutFEM. The other advantage of DG methods, the prevention of skull leakages (Engwer et al., 2017), is likely to be of lesser importance in the CutFEM vs. UDG comparison. Thin skull areas can be modeled accurately using level sets, as anatomical details can be precisely represented.

Concerning source modeling, there has recently been the addition of a local subtraction method (Höltershinken et al., 2023). Local subtraction on tetrahedral CG meshes produces similar error ranges as those of first-order CutFEM with the Venant approach. In the future, it may therefore be promising to combine CutFEM with the local subtraction method, in particular when compared to second-order CutFEM with the partial integration approach.

In total, we found that the use of CutFEM shows promise in controlled spherical scenarios, and we will continue with the analysis of fully realistic head models in the following chapters.

Chapter 7

EEG/MEG group study

In the previous section, we analyzed CutFEM's performance in symmetric, spherical models. We found that CutFEM outperforms continuous Galerkin methods with either tetrahedra or hexahedra as well as an unfitted discontinuous Galerkin approach when using a comparable number of degrees of freedom. In this chapter, we want to extend upon these results and apply CutFEM to real data obtained from MRI and EEG/MEG measurements. We create realistic six-compartment and three-compartment head models and calculate lead fields based on CutFEM, geometry-adapted hexahedral CG-FEM, and BEM. These forward results are then used for the reconstruction of somatosensory evoked potentials/fields in an n = 19 group study.

In the absence of analytical solutions, it is difficult to make statements regarding the accuracy of our results. Reconstruction differences alone will therefore probably not give us a satisfactory answer as to whether to choose one method over another. Except for the new CutFEM scheme, the use of the investigated forward modeling approaches is widely accepted and the margin for localization errors is consequently small. Differences in orientation output however may be significantly more relevant, for example when the reconstructed dipole is used as a target for tDCS stimulation.

Throughout this chapter, we will not only quantify differences in localization/orientation but also investigate further metrics. We will investigate whether any of the 3 methods localizes closer to an anatomical estimate of the post-central gyrus where the somatosensory evoked potentials and fields are generated. Further, differences in the amount of data that can be explained by the different forward models will be analyzed, and estimates of how well sources can be separated will be given.

A particular focus will be set on the question of whether we can reliably estimate both source location and orientation using only MEG data. This will be of particular relevance in the chapter on the reconstruction of epileptic activity, where we have patients whose tDCS stimulation caps will be based on MEG reconstructions alone.

As we have both EEG and MEG data, we can determine whether more realistic volume conductors increase the similarity of the reconstruction outcomes of both modalities. The somatosensory stimulation paradigm used in this study is also suitable for estimating the conductivity of the skull (Aydin et al., 2014; Antonakakis et al., 2020a; Schrader et al., 2020). We can therefore quantify the impact of forward modeling on the estimated skull conductivity and also whether more realistic volume conductor modeling leads to an increase in coherence between EEG and MEG data.

7.1   Data acquisition and head model creation

Before the measurements, the nineteen participants of this study (age 19-49, mean age 26.15±7.76SD, 11 female, 8 male) gave written informed consent in accordance with the declaration of Helsinki. Combined electro- and magnetoencephalography was recorded during medianus nerve stimulation. For EEG, a 60-electrode cap (EasyCap, Herrsching, Germany) was used, and for MEG a setup of 275 axial gradiometers (VSM MedTech Ltd., Vancouver, Canada). The sampling rate was set to 600 Hz. The medianus nerve stimulation consisted of 1932 monophasic electrical square-wave pulses of length 0.5 ms with an inter-stimulus interval uniformly jittered between 350 and 450 ms. The ethics committees of the Universities of Münster (#2015-263-f-S) and Lübeck (#20-459) approved the study and the recorded data was also used in Radecke et al., 2023. Following Buchner et al., 1995, we preprocessed the data with a band-pass filter between 20 and 250 Hz. A 50 Hz notch filter that included harmonics was applied to account for the power line artifact. The data was epoched between -50 and 150 ms relative to the stimulus onset. Bad trials were removed semi-automatically. The data was averaged across trials and an individual 20 ms post-stimulus component with frontal positivity, the so-called P20 (or M20 in MEG Nakamura et al., 1998), was determined. The P20/M20 component is generated in the primary somatosensory cortex Buchner et al., 1995. It can be evoked reliably and creates a very focal response with a high Signal-to-noise ratio (SNR). An exemplary P20/M20 component can be seen in Figure 7.1.

Applications for the analysis of the P20/M20 component include intraoperative neurophysiological monitoring (Sarnthein et al., 2022), diagnostics (Cruccu et al., 2008), or the calibration of skull conductivity (Baysal and Haueisen, 2004).

The MRI data was acquired from a 3 Tesla Magnetom Skyra scanner (Siemens, Erlangen, Germany) with a 64-channel head coil. The T1 sequences were acquired using a 3D MP-Rage sequence (TR = 2300 ms TE = 3.6 ms, TI = 1100 ms, FA = 8°). For the T2, a spin echo sequence was used (TR = 3200 ms, TE = 408 ms, FA = 120°). Inter-subject comparisons of source reconstructions are undertaken in normalized space. Using a nonlinear transformation, the T1 is registered onto a normalized MNI (Montreal Neurological Institute, Collins et al., 1994) MRI using the fieldtrip (Oostenveld et al., 2011) integration of SPM12 (Ashburner et al., 2014). For the MNI image, an AAL atlas stating the labels of the different brain regions was then used to identify the post-central gyrus (Rolls et al., 2020). We will later use this nonlinear transformation to investigate whether our source reconstruction results end up in the correct gyrus. Note however that we only transform the final reconstruction results to MNI space. Forward and inverse modeling takes place on a personalized level for each subject.

For information on the image segmentation and the creation of six-compartment CutFEM and hexahedral CG-FEM head models, see the chapter on head model creation. For MEG in particular, it is common to use a more homogenized head model, as the skull conductivity is of less importance (van den Broek et al., 1998; Gramfort et al., 2010). We therefore opted for a three-compartment BEM model to investigate the impact of head model simplification. Choosing BEM over FEM for our three-compartment
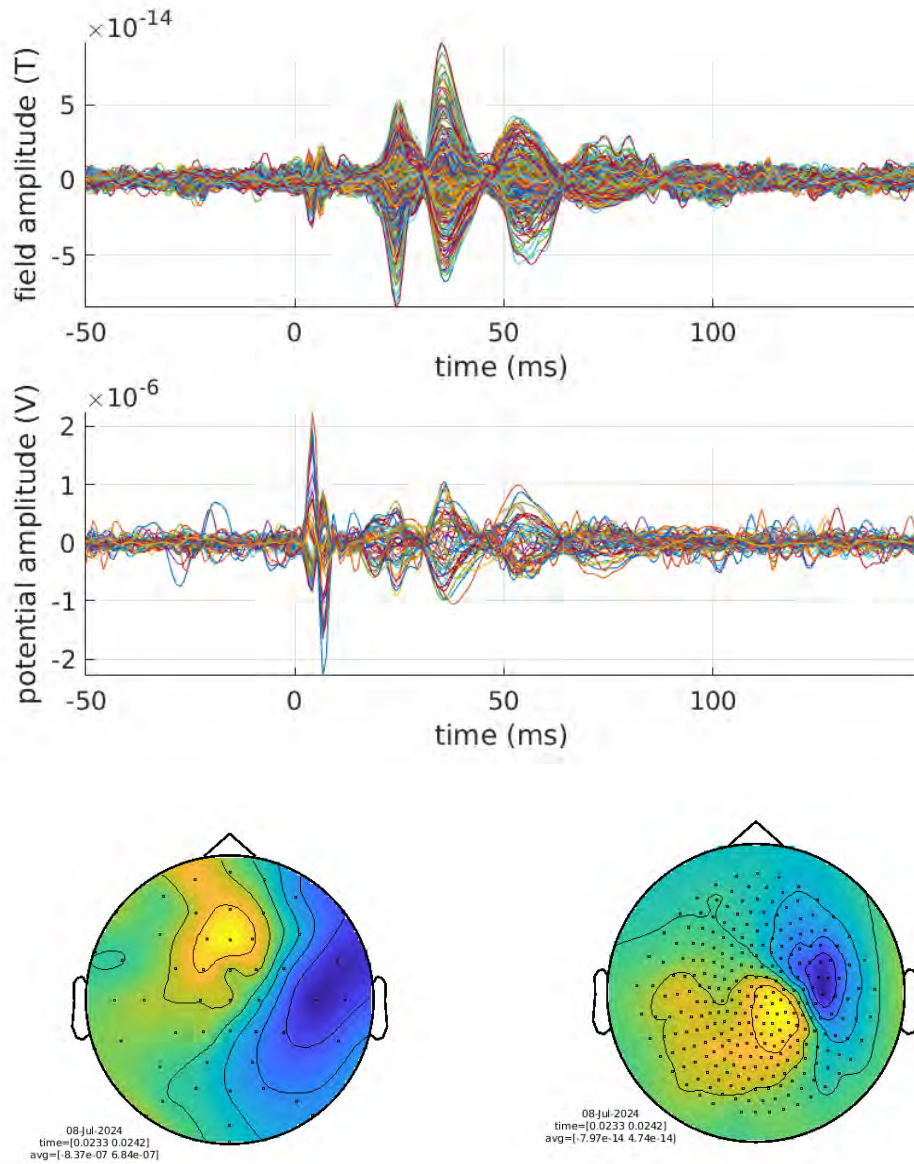
FIGURE 7.1: Averaged evoked somatosensory potentials and fields for subject 1. Top panel: Butterfly plot of averaged MEG data. Center panel: averaged MEG data. Bottom row: P20/M20 peak topographies for EEG (left) and MEG(right).

model will pose the question of whether differences are due to head model simplification or due to the different numerical approach. However, there are already several BEM-FEM comparison Vorwerk et al., 2012; Mahjoory et al., 2017, and in practice, FEM is mostly used in combination with a higher number of compartments.

The surfaces for the BEM models are created from the same binary segmentation result used for CutFEM and the hexahedral model. We define the brain as the union of gray matter, white matter, and CSF, while the combined compacta and spongiosa masks define the skull. To obtain nested compartments, cranial holes were filled and smooth surfaces were extracted with the fieldtrip (Oostenveld et al., 2011) function ft_prepare_mesh. The different models vary in the restrictions that they impose on the feasibility of source positions. For the 3C-BEM model, any point within the inner compartment is suitable, except for points too close to the skull (Gramfort et al., 2010). The six-compartment models place their sources only into the gray matter. We maintain comparability by using a regular grid with 2 mm spacing. Grid nodes outside the gray matter were removed and the remaining nodes moved such that the closest mesh vertex is inside the gray matter. On average, the source spaces for the 19 subjects have 33940 ± 14088 SD nodes.

The BEM lead field is then calculated using the fieldtrip (Oostenveld et al., 2011) integration of OpenMEEG (Gramfort et al., 2011), the FEM lead fields are calculated in DUNEuro (Schrader et al., 2021; Medani et al., 2023). CutFEM lead fields will be called 6C-CutFEM throughout this chapter. The lead fields based on the geometry-adapted hexahedral model are called 6C-HexFEM and the ones created by the three-compartment boundary element method 3C-BEM.

7.2   Solving the inverse problem

We have measured and preprocessed both EEG/MEG and MRI data, segmented and set up our head models, and calculated the lead fields, meaning we have solved the forward problem. Therefore, we can now proceed to localize the generators of the somatosensory evoked fields. In other words, we need to apply a suitable algorithm to solve the inverse problem. We want to solve a linear equation system of the type

$$Lx = y,$$

where $y \in \mathbb{R}^s$ is our measured data, $L \in \mathbb{R}^{sxN}$ is our lead field, and $x \in \mathbb{R}^s$ states the pattern of active sources. As we have tens of thousands of sources in the brain and only a few hundred sensors at the most, this problem is ill-posed. We therefore have an infinite number of possible solutions. Consequently, there is also a host of possible inversion algorithms to choose from. Broadly, they fall into two categories. Single-source reconstruction or current density approaches. Single-source reconstructions such as dipole scanning or fitting assume that there is only a limited set of active dipoles in the brain, typically no more than 1 or 2 (Darvas et al., 2004). As their output is a single dipole location and moment (or a probability distribution over the source space), the differences when switching subjects and forward methods are easy to quantify. In reality, an EEG/MEG signal is only measurable if a

sufficiently large patch of neurons is active, hence the assumption of a dipolar model only holds well for focal generators. If the source is dominated by noise, e.g. from muscle artifacts, beamformer algorithms may be used instead (Buschermöhle et al., 2024; Neugebauer et al., 2022).

Current density approaches such as minimum norm estimation do not place a limit on the number of simultaneously active sources (Hauk, 2004). Their reconstruction output is a patch rather than a single dipole. While we have an active patch of neurons in reality, in practice, current density approaches may feature smeared results if the underlying source is focal.

Our goal in this thesis is to quantify the impact forward modeling has on the final source localization. With the somatosensory evoked potentials/fields from our medianus stimulation, we have a very focal source with a dipolar pattern, motivating the use of a single-source inversion model. Muscle or eye artifacts are either removed in the preprocessing or averaged out over trials, giving us a clear signal with high SNR. We may therefore use a simple dipole scan for our inversion. Note that the assumption of a single active source is not entirely correct. The generators of the P20/M20 response that are located in the post-central gyrus in Brodmann area 3B are temporally preceded by thalamic activation than can be seen in the EEG but due to its depth not in the MEG (Buchner et al., 1995; Scherg and Buchner, 1993). To account for a possible overlap of thalamic and cortical activation, it has been suggested to place an additional source into the thalamus when performing an EEG dipole scan/fit (Götz et al., 2014). Before doing so, we want to give a short introduction to EEG/MEG dipole scanning.

Dipole Scanning

In its basic formulation, a dipole scan is the solution of the least squares problem

$$\min_{x,\eta} ||C^{-1}(y - L(x)\eta)||_2^2, \tag{7.1}$$

where y is the measured data, x is the location within the source space, $L(x) \in \mathbb{R}^{s \times 3}$ the lead field at location $x \in \Omega$ with one column per spatial direction. $\eta \in \mathbb{R}^3$ is the source strength with each entry stating the contribution of the different directions. $C \in \mathbb{R}^{s \times s}$ is a diagonal matrix that contains the channel-wise standard deviations of the noise activity in the pre-stimulus interval from -50 to -5 ms. Channels with higher noise levels are weighed lower when estimating the residual variance. In practice, we can iterate over all x in the source space, determine the optimal orientation $\eta_{x,opt}$ using the pseudo-inverse of $L(x)$ and calculate the residual variance $||C^{-1}(y - L(x)\eta_{x,opt})||_2^2 / ||C^{-1}y||_2^2$. The residual variance (RV) states the proportion (in %) of the signal power left unexplained by our reconstruction.

For both EEG and MEG, we perform slight adaptations to the inserted lead field matrix. For the EEG, we investigate the addition of a secondary thalamic source. We use the AAL atlas to determine the center of the thalamus in MNI space, then transform that location to each subject's MRI and identify the closest source position x_0. The modified EEG lead field $L(x, x_0)$ then contains 6 columns. 3 from the thalamic source x_0 that stays constant throughout the minimization and 3 that depend on the changing source location x. From

the pseudoinverse of this modified lead field, we then obtain an individual source strength for the cortical and the thalamic source.

Due to its depth, the thalamic source is not visible in the MEG and can therefore be neglected. In spherical head models, we distinguished between radial and tangential sources because the radial sources produced no magnetic field outside the volume conductor. While this is no longer the case in less homogenized, more realistic head models, we still have a sensitivity bias towards quasi-tangential sources (Ahlfors et al., 2010). Note that the terms radial and tangential are only well-defined in spherical head models. By quasi-radial or quasi-tangential sources we refer to the orientation of the vector that points from the source towards the inner skull surface (Haueisen et al., 2012). The issue with this sensitivity bias is that the noise present in the data might lead to an amplification of the radial reconstruction component. Therefore, it is common practice to regularize the MEG lead field in some manner. One way is to add a Tikhonov-based regularization term that dampens the magnitude of η (Tikhonov and Arsenin, 1977). It is however difficult to select a proper regularization strength.

An alternative is to truncate the lead field by removing the quasi-radial contributions. In practice, the quasi-radial orientation is calculated through a singular value decomposition (Piastra et al., 2021; Ahlfors et al., 2010). Let $x \in \Omega$. Then the MEG lead field can be written as a singular value decomposition $L(x) = U\Sigma V^t$, where Σ is a diagonal matrix with 3 non-zero entries, the singular values. The smallest of these is then the singular value corresponding to the quasi-radial direction. Setting it to zero truncates the lead field and removes any quasi-radial contributions and therefore any blow-up in the quasi-radial direction. However, the reconstructed dipole moment is now restricted to a 2D plane. While the M20 is a predominantly quasi-tangential source, the cortical normal is unlikely to be purely quasi-tangential. This option is the default in toolboxes such as fieldtrip.

The option we propose here is a modification from (Wolters et al., 1999). We perform the truncation based on a ratio of the size of the smallest singular value and the noise level of the data individually at each source location x in our grid. Whether the radial contribution is exceeded by measurement noise is quantified based on the signal-to-noise (SNR) definition in (Piastra et al., 2021; Goldenholz et al., 2009). Let $x \in \Omega$, N be the number of MEG sensors, v_x be the singular vector corresponding to the quasi-radial direction. The noise level σ_s at sensor s. is calculated for each channel individually as the standard deviation of the pre-stimulus interval from -50 to -5 ms. The σ_i's are the squares of the entries of the normalization matrix C. Then the SNR of a quasi-radial source at location x in the source space is given as

$$\mathrm{SNR}(x) = 10\log_{10}\frac{1}{N}\sum_{s=1}^{N}\frac{(aL_xv_x)_s^2}{\sigma_s^2}. \tag{7.2}$$

The lead field matrix can be chosen based on 3C-BEM, 6C-HexFEM, or 6C-CutFEM, leading to an individual SNR value for each forward modeling approach. The source strength a is adapted to our somatosensory experiment. In the literature, a source strength of 21 nAm has been reported for the M20 (Antonakakis et al., 2020a). The M20 is primarily a quasi-tangential source, but if we assume it to be about $10°$ out of the quasi-tangential plane, we

FIGURE 7.2: Calibrated EEG skull conductivities based on different forward approaches. Values in Siemens per meter. 6-compartment Hexahedral FEM values in black, 6-compartment CutFEM values in green, and 3-compartment BEM values in blue.

would end up with a radial contribution of about $4\,\text{nAm}$ as $\sin(10) * 21 \approx 4$. We then perform the truncation of the lead field if the $\text{SNR}(x)$ at a given point is lower than 3. A value larger than 3 implies that the average signal power across all channels exceeds twice the power of the noise.

Piastra et al., 2021 and Goldenholz et al., 2009 used a source strength of $10\,\text{nAm}$ but investigated sources with orientations estimated from the cortical normal. These oblique source orientations contain both quasi-tangential and quasi-radial components whereas we only focus on the quasi-radial part here.

The conditional truncation of the lead field that we perform here is strongly based on the structure of the somatosensory field data we analyze. Whether a similar procedure can be performed in different experimental setups largely depends on the availability of a reliable noise covariance estimate and a priori knowledge of the source strength.

Skull conductivity calibration

A central parameter in EEG source reconstruction is the conductivity of the skull layers. It has a strong influence on the depth of the reconstructed dipoles. As the MEG is less sensitive to the skull conductivity, a combination of EEG and MEG data can be used to optimize the skull conductivity for the EEG (Aydin et al., 2014; Antonakakis et al., 2020a). We first perform an MEG dipole scan and save the resulting dipole location x_{MEG}. Then we minimize the EEG residual variance at x_{MEG} over a range of skull compacta conductivities, between 0.008 and $0.3\,\text{Sm}$. For the 6-compartment methods, the skull spongiosa conductivity is set to a fixed 3.6 times the compacta conductivity. Minimizing the residual variance is assumed to be a convex problem, hence a Brent algorithm can be used to minimize the number of tested conductivity values (Schrader, 2022). The conductivity value that minimizes the residual variance is then used to calculate a full, calibrated EEG lead field for all source positions in the grid. Note that the MEG skull conductivity is not affected by this calibration procedure. An overview of the calibration values for all subjects can be found in Figure 7.2. 6C-HexFEM yielded 2.92 % higher skull compacta conductivity values than 6C-CutFEM, 3C-BEM 10.55 % higher values. The higher conductivity values for BEM probably offset the presence of the more conductive spongiosa layer in the 6-compartment methods. The differences are small and a repeated measures ANOVA shows no statistically significant differences.
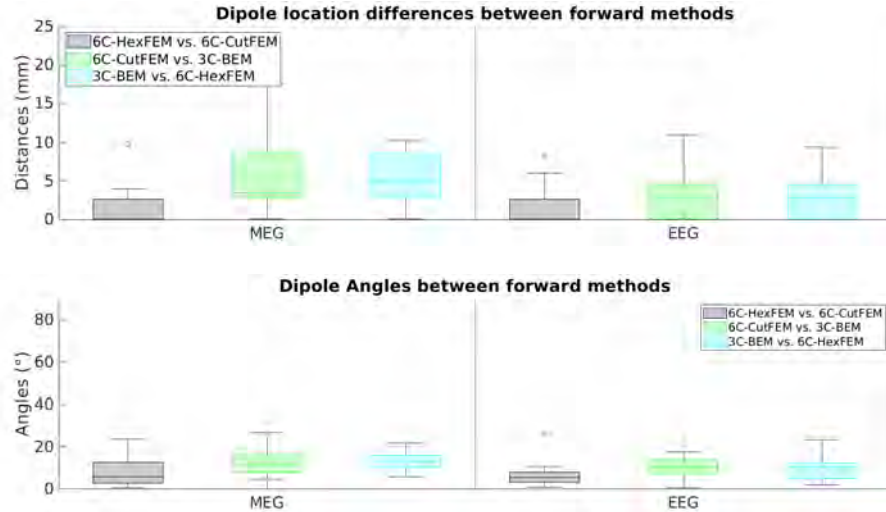
FIGURE 7.3: Differences in the reconstructed dipoles' location (top) and orientation (bottom). Differences are computed between 6C-CutFEM and 6C-HexFEM (black), 6C-CutFEM and 3C-BEM (green), and 6C-HexFEM and 3C-BEM (blue). Location differences in mm, angles in degrees. Differences based on MEG data are on the left, based on EEG on the right.

7.3   Results

Location and Orientation

We now turn to the first source reconstruction results. The first, and from a user's perspective possibly most significant results that we look at are differences in location and orientation. We compare individual differences between 6C-CutFEM vs. 6C-HexFEM, 6C-CutFEM vs. 3C-BEM, and 6C-HexFEM vs. 3C-BEM. Angles in degree and distances in millimeters for both EEG and MEG can be found in Figure 7.3. MEG dipole location differences are small on average, but can exceed 10 mm between the FEM approaches and reach 17.55 mm when comparing 6- and 3-compartment methods. Average angles are around 10 degrees but can exceed 30 degrees in MEG-based BEM-FEM comparisons and 25 degrees in EEG. Overall, as one would expect, the differences between 6-compartment CutFEM and HexFEM are smaller than the differences between either 6-compartment method and 3C-BEM.

For most subjects, the impact of switching forward models may therefore be small, but a difference of 1 cm may mean the difference in reconstructing to one gyrus or another. This is particularly important when the reconstruction is used to guide further invasive diagnostics, such as in epilepsy (Antonakakis et al., 2024a). The differences in angle are of relevance when the reconstruction is used as a target for a subsequent optimized tDCS stimulation (Khan et al., 2022). A small difference in the reconstructed angles may significantly alter the electrode placement.

As mentioned, we can also project our reconstructions into normalized MNI space, where the AAL atlas gives us an estimate of the post-central gyrus where the generators of the P20/M20 are located. A visualization of the reconstructions and the somatosensory cortex can be found in Figure 7.4. We see that all reconstructions broadly lie in the somatosensory cortex

and point tangentially toward the motor cortex. As could be expected from the previous results, average differences in the sub-centimeter range and under 10 degrees are difficult to identify by the naked eye. Note that the reconstructed orientations are only approximations as the transformation into MNI space is nonlinear.

The EEG reconstructions have a higher spread than the MEG reconstructions. When we compute the center of the 19 6C-CutFEM MEG reconstructions, then the average distance of each single reconstruction to that center is 4.95 mm. The 6C-CutFEM EEG spread is 7.77 mm. The other two methods have similar spreads, 5.38 and 8.78 mm for 6C-HexFEM, 5.60 and 9.29 mm for 3C-BEM.

We can further measure the distance between the projections of the reconstructed dipoles and the post-central gyrus. The corresponding EEG and MEG distances can be found in Figure 7.5. When reconstructing the MEG data, we see that the six-compartment methods localize closer to the post-central gyrus than the three-compartment method. Both average distance and standard deviation are approximately 1 mm smaller. 3.36 ± 2.92 mm SD for 6C-CutFEM, 3.70 ± 3.44 mm SD for 6C-HexFEM, 4.95 ± 4.08 mm SD for 3C-BEM. Comparing the distances to the post-central gyrus and the between method distances, we see that the subject with the highest difference (17.54 mm) between 6C-CutFEM and 3C-BEM also has the highest 3C-BEM distance to the post-central gyrus (16.13 mm) while CutFEM reconstructed 3.50 mm away from the somatosensory cortex. Similarly, the subject with the highest difference between 6C-CutFEM and 6C-HexFEM (9.74 mm) also has the highest 6C-HexFEM distance to the post-central gyrus (10.35 mm) where CutFEM only has 3.7 mm.

While CutFEM yields the best results here, these should not be overstated. The quality of the transformation into MNI space depends strongly on how similar the individual subjects' cortex can be matched with the MNI152 average. Our results may also depend on the choice of the atlas. The anatomical AAL atlas with the entire post-central gyrus covers a much larger area than the Brodmann area 3B. Choosing a functional atlas that explicitly covers only Brodmann area 3B yields distances about 2 times higher, but does not qualitatively change the statements of the previous section.

Coherence between EEG and MEG reconstructions

So far, we have looked at EEG and MEG reconstructions separately. Now we investigate whether the use of a more realistic volume conductor increases the coherence between EEG and MEG reconstructions. To do so, we again compute location differences and angles, this time between EEG and MEG reconstructions. The results can be seen in Figure 7.6. The average distance between a MEG-based and an EEG-based reconstruction is 10.14 mm for 6C-HexFEM, 10.76 mm for 6C-CutFEM, and 10.24 mm for 3C-BEM. The average angles are 28.25°, 27.83°, and 22.87° respectively. Adding more tissue compartments therefore does not directly increase the similarity of EEG and MEG reconstructions in our test scenario.

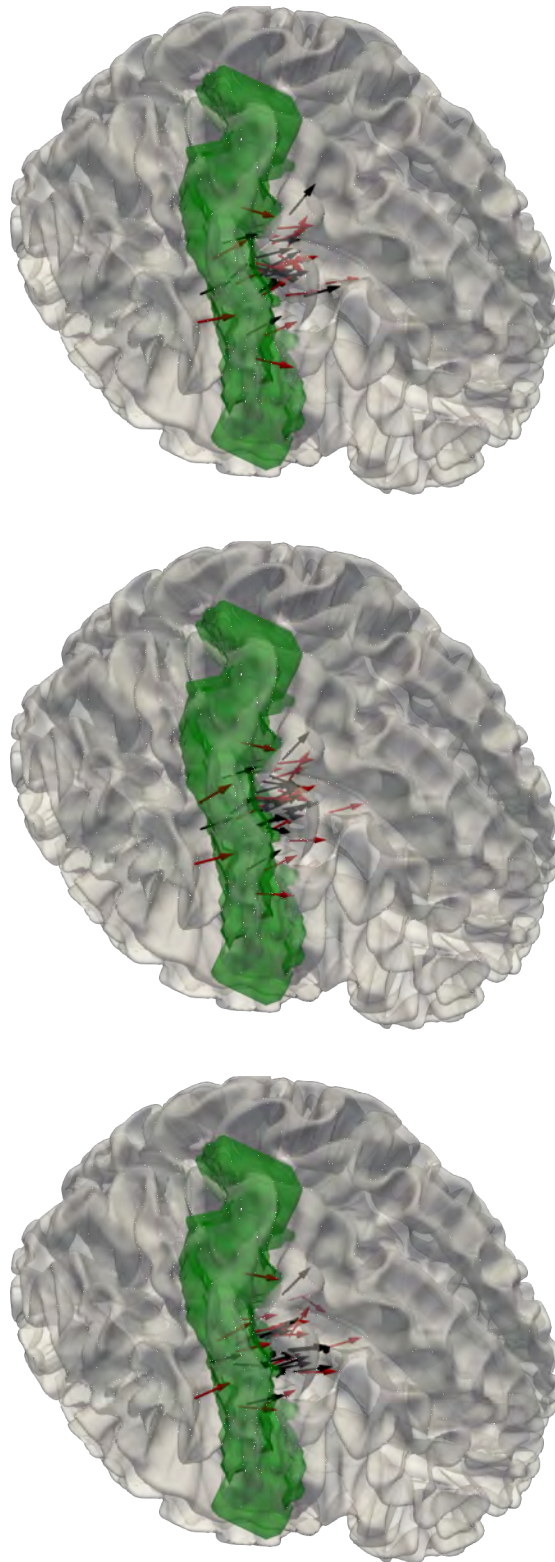FIGURE 7.4: Source reconstructions in normalized MNI space. EEG source reconstructions are red, MEG reconstructions are black. One arrow corresponds to the reconstructed dipole of one subject. Top panel: 6C-HexFEM reconstructions. Center: 6C-CutFEM reconstructions. Bottom: 3C-BEM reconstructions. In white we see the averaged white matter of the MNI152 T1 image. The post-central gyrus based on the AAL-atlas is green.
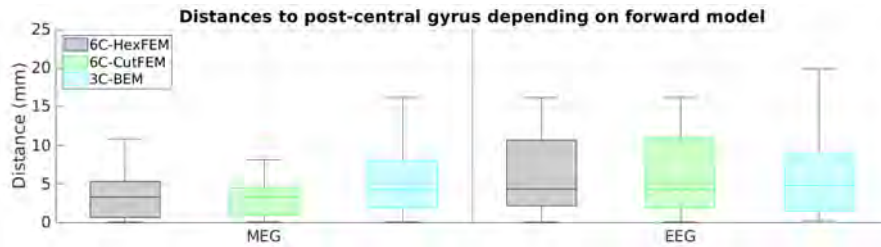
FIGURE 7.5: Distances (mm) to post-central gyrus depending on the forward model. 6C-HexFEM-based distances in black, 6C-CutFEM in green, 3C-BEM in blue. Distances of MEG reconstructions on the left, EEG distances on the right.
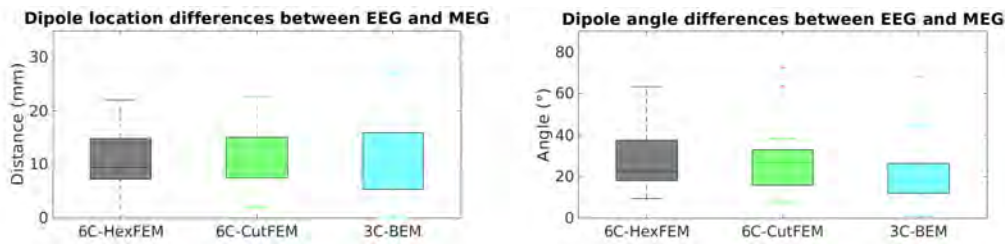
FIGURE 7.6: Location differences (left panel) and angles (right panel) between EEG and MEG-based source reconstructions when using different forward models. 6C-HexFEM-based distances in black, 6C-CutFEM in green, 3C-BEM in blue.

Residual variance

In the next step, we want to investigate whether we can better explain the measured data by creating realistic, six-compartment head models. Our first metric here is the residual variance. Boxplots showing the individual residual variances of each subject, grouped by the forward approach can be found for EEG and MEG in Figure 7.7. Starting with the MEG, we see the 3-compartment BEM model produces higher residual variances, meaning the BEM-reconstructed dipole explains a smaller proportion of the data than the six-compartment models. The average residual variance for 6C-CutFEM and 6C-HexFEM is identical at 3.6 %, 1.0 % lower than the average for 3C-BEM. A repeated measures ANOVA shows a significant main effect of the forward method (CutFEM/HexFEM/BEM) on the residual variance (($F_{(1.11, 19.9)}$ = 14.054, p = 0.0009, η^2 = 0.077). A subsequent pairwise t-test with Holm correction (Holm, 1979) shows no significant differences between the six-compartment methods, but significant differences between 6C-CutFEM and 3C-BEM (p<0.001) with a large effect size of 0.907 as measured by Cohen's d (Cohen, 1972b). The residual variances resulting from the reconstruction of EEG data are significantly higher with averages of 11.18 %, 11.30 %, and 11.55 % for 6C-CutFEM, 6C-HexFEM, and 3C-BEM respectively.

We can therefore state that the six-compartment methods are significantly better at explaining the measured data, especially in the MEG case. At this point, we cannot say whether this difference is due to a better fit to the P20/M20 signal or whether the six-compartment methods overfit noise. However, we have an excellent noise estimate based on the pre-stimulus interval and can use that to quantify the expected Euclidean distance between
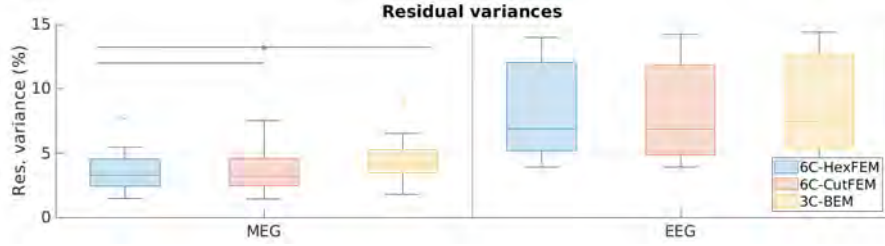
FIGURE 7.7: Residual variance (%) of the P20/M20 reconstruction using lead-field matrices from different forward models. The asterisk marks significant differences (MEG only) 6C-HexFEM in blue, 6C-CutFEM in red, and 3C-BEM in yellow. Outliers are depicted as circles, and the horizontal bar inside the boxes states median values. The x-axis is divided by the modality. MEG on the left, EEG on the right.

measured data and reconstructed source

$$\mathbb{E}(||\hat{Y} - Y||_2^2). \tag{7.3}$$

Here, Y is again our measured data, and $\hat{Y} = L(x_{opt})\eta_{x_{opt},opt}$ is the result of our dipole scan. For simplicity, we omitted the noise normalization matrix C^{-1} here. We assume that x_{opt} is the true source location and L is the true lead field, meaning that we do not have a modeling error in our lead field. Our intent here is only to quantify the impact of additive noise on our residual variance. Abbreviating $Lx = L(x_{opt})\eta_{x_{opt},opt}$, we then have

$$Y = Lx + N,$$

where N is the noise present in the data. It is assumed to be uncorrelated to the actual P20/M20 component. With the pseudoinverse L^+ of L we have

$$\hat{Y} = LL^+Y = LL^+(Lx + N) = LL^+Lx + LL^+N$$

$$= Lx + LL^+N.$$

Hence

$$\mathbb{E}(||\hat{Y} - Y||_2^2) = \mathbb{E}(||LL^+N - N||_2^2)$$

$$= \mathbb{E}(||(I - LL^+)N||_2^2) = \mathbb{E}(||(I - P_{Im(L)})N||_2^2)$$

$$= \mathbb{E}(||P_{Im(L)^\perp}N||_2^2),$$

where $P_{Im(L)^\perp}N$ is the orthogonal projection of N onto the complement of the span of the lead field matrix L. Note that $(I - P_{Im(L)})N = P_{Im(L)^\perp}N$.

This means that the expected difference between measured and reconstructed data is only affected by noise components that cannot be explained by the lead field. Now let $V = (v_1, ..., v_k)$ be a basis of $Im(L)^\perp$. Then by the Pythagorean theorem, we have

$$\mathbb{E}(||P_{Im(L)^\perp}N||_2^2) = \mathbb{E}(||\sum_i <v_i, N> v_i||_2^2) = \sum_i \mathbb{E}(||v_i, N> v_i||_2^2)$$

$$= \sum_i \mathbb{E}(<v_i, N>^2) = \sum_i \mathbb{E}(v_i^t NN^t v_i) = \sum_i v_i^t C v_i = Tr(P_{Im(L)^\perp}C.$$
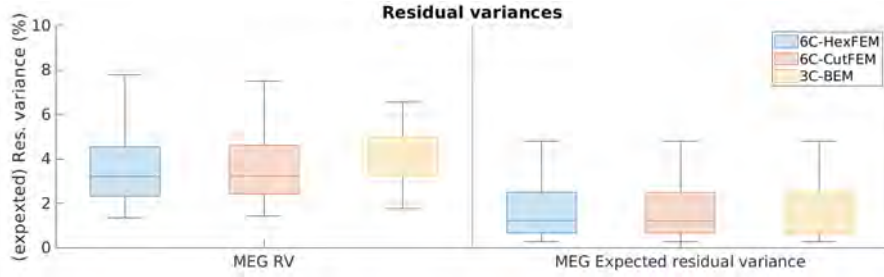
FIGURE 7.8: Expected MEG Residual variance (%) of the M20 reconstruction using leadfield matrices from different forward models. 6C-HexFEM in blue, 6C-CutFEM in red, and 3C-BEM in yellow. Outliers are depicted as circles, and the horizontal bar inside the boxes states median values. The x-axis is divided by the modality. MEG residual variance without SNR normalization on the left, expected residual variance on the right.

C is again the estimated noise covariance matrix from the prestimulus interval. In other words, we can calculate the expected difference from the trace of the projection of the noise covariance matrix onto the orthogonal complement of L. Normalizing $\mathbb{E}(||\hat{Y} - Y||_2^2)$ with $||y||_2^2$ in the same manner as the residual variance gives us an approximation of the expected residual variance (eRV).

A comparison of expected and actual residual variance for the different forward modeling approaches can be found in Figure 7.8. Note that to maintain consistency, the residual variance here was calculated without the SNR normalization with C^{-1}. We see that the expected residual variance is almost identical for all 3 forward modeling approaches. The average eRV is $1.68 \pm 1.30\,\%$ SD. Only in one subject was the eRV higher than the actual residual variance ($0.04\,\%$ for 6C-HexFEM, $0.16\,\%$ for 6C-CutFEM, $0.19\,\%$ for 3C-BEM).

We can therefore state that all lead fields are identical in the way they fit the additive noise in the data. Differences in residual variance are most likely not due to the overfitting of additive noise. Note that the eRV is not a measure for the amount of noise present in the reconstructed dipole. It only states the proportion of the observed residual variance that is due to noise that cannot be explained by the lead field. The actual residual variance is additionally affected by all other modeling errors. This includes all the inaccuracies incurred by preprocessing the data Y and creating the lead field matrix L, such as the dipolar source model, the limited number of head tissues, uncertainties in the electric conductivities, and sensor-to-head registration. It also includes the artifact from the electric stimulation and possible contributions of thalamic activity.

Source separability

In this section, we investigate the behavior of the residual variance as a function over the source space. We first look at the distribution of the RV over the cortex for subject 1 from our study. In Figure 7.9, we see that the difference between the six-compartment models features a similar residual variance distribution. The RV has an ellipsoidal shape on the cortex, the short diagonal is parallel to the direction of the reconstructed dipole, while the long
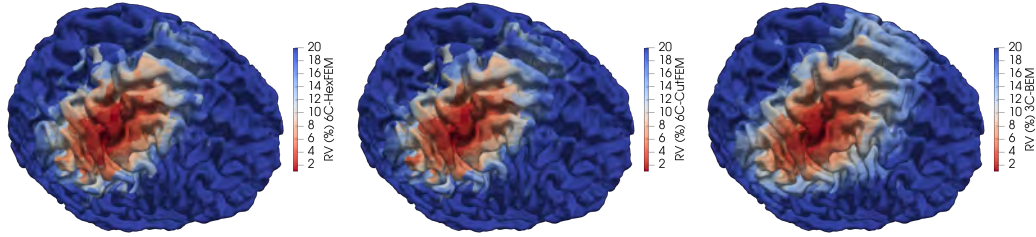
FIGURE 7.9: Absolute MEG residual variance (%) interpolated on cortex for subject 1. Left panel: Residual variance based on 6C-HexFEM lead field. Center panel: Based on 6C-CutFEM. Right panel: Based on 3C-BEM.

diagonal follows the central sulcus. Along the short diagonal, there is no apparent difference between three- and six-compartment methods but 3C-BEM is more spread along the long diagonal. This gives us a first indication that there might be a difference in the slope of the residual variance distribution which we will investigate in the next step.

While the shape of the RV distribution may be irregular, it will always have one global minimum at x_{opt}. We associate source separability with the shape of the residual variance function. If the $RV(x)$ increases more rapidly for one lead field over another when increasing $||x - x_{opt}||_2$, the minimum at x_{opt} is also clearer. A greater proportion of the measured data can only be explained by the lead field matrix at x_{opt}. Therefore a steeper increase in residual variance means that the reconstructed sources can be better distinguished by the surrounding sources. Note that source separability states, given one active source, how confident we are in choosing one location over another in close vicinity. It does not tell us how well we can distinguish two proximate active sources. All considerations here are derived from a single-source scenario.

We now state an exemplary process for calculating the source separability for 6C-CutFEM. The procedure is identical for all three forward models. For each subject, we first extract all source locations from the source grid whose distance to $x_o pt$ is less than 20 mm, between 218 and 295 total points depending on the subject. For each point x we then calculate the ratio of the residual variance $RV(x)/RV(x_{opt}$ and sort the points by their distance to x_{opt}. This gives us the CutFEM ratio for the source separability. We then repeat the process for the other lead fields. Note that x_{opt} depends on the lead field, hence the selected points also differ for each method. In total, we then have three sets of RV-ratios and spatial distances, with 30702 total points for the MEG and 30225 points for the EEG.

In Figure 7.10., we see Ratio vs. distance plots for each forward model and for both EEG and MEG. The curves are interpolated from the average RV ratio for each distance bin (bins are all integers from 0 to 20). Shaded areas indicate one standard deviation, also calculated per bin. Note that the scale is logarithmic and different for EEG and MEG. The MEG ratios exceed 10 where the maximal EEG ratios are below 2.5 as the overall residual variances are much lower in MEG than in EEG. The large standard deviation values are due to a high per-subject variance in residual variance. We see that the ratio increases most rapidly for 6C-CutFEM, followed by 6C-HexFEM, and 3C-BEM in both EEG and MEG.

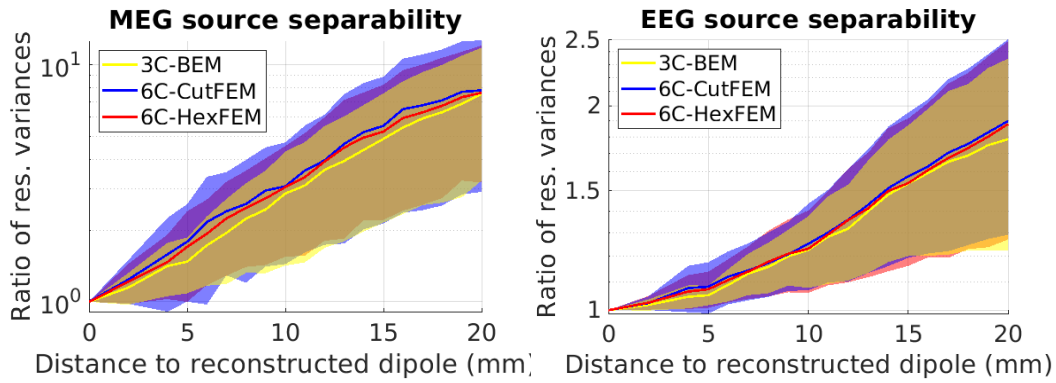In the second step, we perform an ANCOVA analysis to analyze the main

FIGURE 7.10: Source separability estimates for MEG (left panel) and EEG (right panel) depending on the forward model. X-axis: distance to reconstructed source $||x - x_{opt}||$. Y-axis: Residual variance ratio $RV(x)/RV(x_{opt})$, scaled logarithmically. Curves for 3C-BEM in yellow, 6C-CutFEM in blue, and 6C-HexFEM in red. Shaded areas indicate one standard deviation.

effect of the forward method (6C-HexFEM, 6C-CutFEM, 3C-BEM), distance to the minimum, and their interaction on the RV-ratio. For MEG, the AN-COVA shows two significant main effects and an interaction effect (Forward model: $F(2,30190) = 108.77$, $p < 0.001$, $\eta^2 = 0.007$. Distance to x_{opt}: $F(2,30190) = 8240.73$, $p < 0.001$, $\eta^2 = 0.214$. Interaction of the two: $F(2,30190) = 5.601$, $p < 0.001$, $\eta^2 = 0.0004$) were observed. For EEG, the ANCOVA yields similar results. Forward model: $F(2,30219) = 35.502$, $p < 0.001$, $\eta^2 = 0.002$. Distance to x_{opt}: $F(2,30219) = 9283.664$, $p < 0.001$, $\eta^2 = 0.235$. Interaction of the two: $F(2,30219) = 7.086$, $p < 0.001$, $\eta^2 = 0.0004$.

Next, we perform pairwise comparisons between the forward models. The R (R Core Team, 2013) function *estimate_contrasts* from the *modelbased* toolbox is used to estimate the pairwise contrasts (6C-CutFEM - 3C-BEM, 6C-CutFEM - 6C-HexFEM, 6C-HexFEM - 3C-BEM) at 4 bins (5, 10, 15, 20 mm) of distances to x_{opt}. Holm-adjusted p-values and confidence intervals are then calculated per bin.

The contrasts and their statistical significance can be seen in Table 7.1. for MEG and in Table 7.2. for EEG. The contrast has to be understood as a difference in ratios. At 10 mm distance to x_opt, the MEG-based 6C-CutFEM RV-ratio has increased on average 77 % more than the 3C-BEM ratio. The 95 % confidence interval is 53-101 %. 6C-CutFEM yields a statistically significant better source separability than 3C-BEM already at 5 mm distance to the source, where the difference between 6C-HexFEM and 3C-BEM is only significant at 10 mm distance or more.

Qualitatively, similar statements hold for the EEG, but the contrasts are smaller, and statistical significance is only reached at higher distance levels. The expectation, that the larger influence of volume currents in EEG leads to larger differences in source separability therefore does not hold in this setting.

MEG radial contributions

The final investigations we perform in this chapter are concerned with the reliable reconstruction of quasi-radial components using MEG data alone.

MEG Contrast	Distance to Source	Mean difference	p	CI_low	CI_high
6C-CutFEM - 3C-BEM	5	50	**0.011**	9	92
6C-CutFEM - 3C-BEM	10	77	**<0.001**	53	101
6C-CutFEM - 3C-BEM	15	103	**<0.001**	87	119
6C-CutFEM - 3C-BEM	20	129	**<0.001**	103	156
6C-CutFEM - 6C-HexFEM	5	9	0.601	-33	52
6C-CutFEM - 6C-HexFEM	10	29	**0.006**	4	54
6C-CutFEM - 6C-HexFEM	15	48	**<0.001**	32	64
6C-CutFEM - 6C-HexFEM	20	68	**<0.001**	41	94
6C-HexFEM - 3C-BEM	5	41	0.036	-1	83
6C-HexFEM - 3C-BEM	10	48	**<0.001**	24	72
6C-HexFEM - 3C-BEM	15	55	**<0.001**	39	71
6C-HexFEM - 3C-BEM	20	62	**<0.001**	38	88

TABLE 7.1: Source separability: Relative increase in MEG residual variance (*rv*) ratio with increasing distance (mm) to the minimal source location *rv*. Pairwise contrasts of the three different forward models. Columns from left to right: Contrast formula (reads Model1 'minus' Model2), distance to the source that minimizes the *rv*, Difference between the methods in %, p-value, and the 95 % Confidence Interval for the difference in *rv*-ratio. Bold p-values indicate significant ($p < 0.05$) differences.

EEG Contrast	Distance to Source	Mean difference	p	CI_low	CI_high
6C-CutFEM - 3C-BEM	5	-0.42	>0.99	-4	4
6C-CutFEM - 3C-BEM	10	2	**0.035**	0.00	4
6C-CutFEM - 3C-BEM	15	5	**<0.001**	3	6
6C-CutFEM - 3C-BEM	20	7	**<0.001**	5	10
6C-CutFEM - 6C-HexFEM	5	<0.1	>0.99	-4	4
6C-CutFEM - 6C-HexFEM	10	<0.1	0.33	-1	3
6C-CutFEM - 6C-HexFEM	15	2	**<0.001**	1	3
6C-CutFEM - 6C-HexFEM	20	3	**<0.001**	1	5
6C-HexFEM - 3C-BEM	5	<0.1	>0.99	-4	3
6C-HexFEM - 3C-BEM	10	1	0.32	-1	3
6C-HexFEM - 3C-BEM	15	3	**<0.001**	2	4
6C-HexFEM - 3C-BEM	20	4	**<0.001**	2	7

TABLE 7.2: Source separability: Relative increase in EEG residual variance (*rv*) ratio with increasing distance (mm) to the minimal source location *rv*. Pairwise contrasts of the three different forward models. Columns from left to right: Contrast formula (reads Model1 'minus' Model2), distance to the source that minimizes the *rv*, Difference between the methods in %, p-value, and the 95 % Confidence Interval for the difference in *rv*-ratio. Bold p-values indicate significant ($p < 0.05$) differences.

Going back to the SNR-based truncation described at the beginning of the chapter, we quantify the SNR distribution over the cortex. For each subject, we calculate the SNR of a quasi-radial source of 4 nAm strength at every location in the individual source grid. The grid is then projected into normalized MNI space and interpolated onto the same cortical surface. Here, the average across all 19 subjects is calculated and visualized. The cortical sheet and an inflated representation stem from the Freesurfer (Fischl, 2012) *surfrend* toolbox.

The SNR distribution can be seen in Figure 7.11. For 6C-CutFEM, we see that quasi-radial contributions are weakest on the gyral crowns and increase when moving down the gyral walls. Overall, the strength of a quasi-radial contribution is more dependent on the location of the source on the gyrus rather than the location of that gyrus in the brain. In contrast, the SNR in 3C-BEM changes more depending on where the source lies in the brain rather than where on the gyrus the source is positioned. In other words, 3C-BEM changes are spatially low-frequent, and 6C-CutFEM changes in SNR distribution are high-frequent. This becomes most apparent in the images in the fourth row of Figure 7.11., where the difference between 6C-CutFEM and 3C-BEM is depicted. 6C-HexFEM follows a similar pattern as 6C-CutFEM, but the differences between the gyral crown and fold are less distinct. The overall average SNR for 6C-CutFEM is 3.51 dB, and the one for 3C-BEM is 2.29 dB. 6C-HexFEM has an average SNR of 3.32 dB. For reference, the average SNR of the measured M20 components is 19.54 ± 3.20 SD.

It may seem surprising that in many places the SNR increases with increasing source depth as the overall signal strength decreases with increasing distance to the sensors. The reason for this stems from the fact that we only investigate quasi-radial contributions here. In addition, we therefore quantified the magnitude of the strongest and weakest singular values. The results can be seen in Figure 7.12. We see that an increasing source depth has opposing effects on the magnitude of the smallest and largest singular values. The smallest, representing the quasi-radial orientation, increases in a fashion that matches the SNR distribution while the largest decreases rapidly. The resulting condition of the lead field matrix - measured as a ratio of smallest to largest singular value - rapidly decreases with increasing source depth. The differences between the three methods follow the results from the SNR distribution, high frequent changes for six-compartment methods, and low-frequent changes for 3C-BEM. 6C-HexFEM is again slightly smeared when compared to 6C-CutFEM.

We have two possible explanations for this behavior. First, the volume conductor near the gyral crowns may be more symmetric around the gyral crowns, with the skull above, CSF to the sides, and gray/white matter below. In contrast, a source on a gyral wall may have CSF to one side, gray matter to the other, and a combination of the two above, resulting in a less homogeneous environment that is more distinct from a spherical volume conductor that would result in a zero field.

Secondly, our method of distinguishing quasi-radial and -tangential orientations may be less precise when the source lies deep inside the volume conductor. As the skull is not perfectly spherical, a deeper source may be equidistant to different areas of the skull, possibly reducing the accuracy of the singular value decomposition.
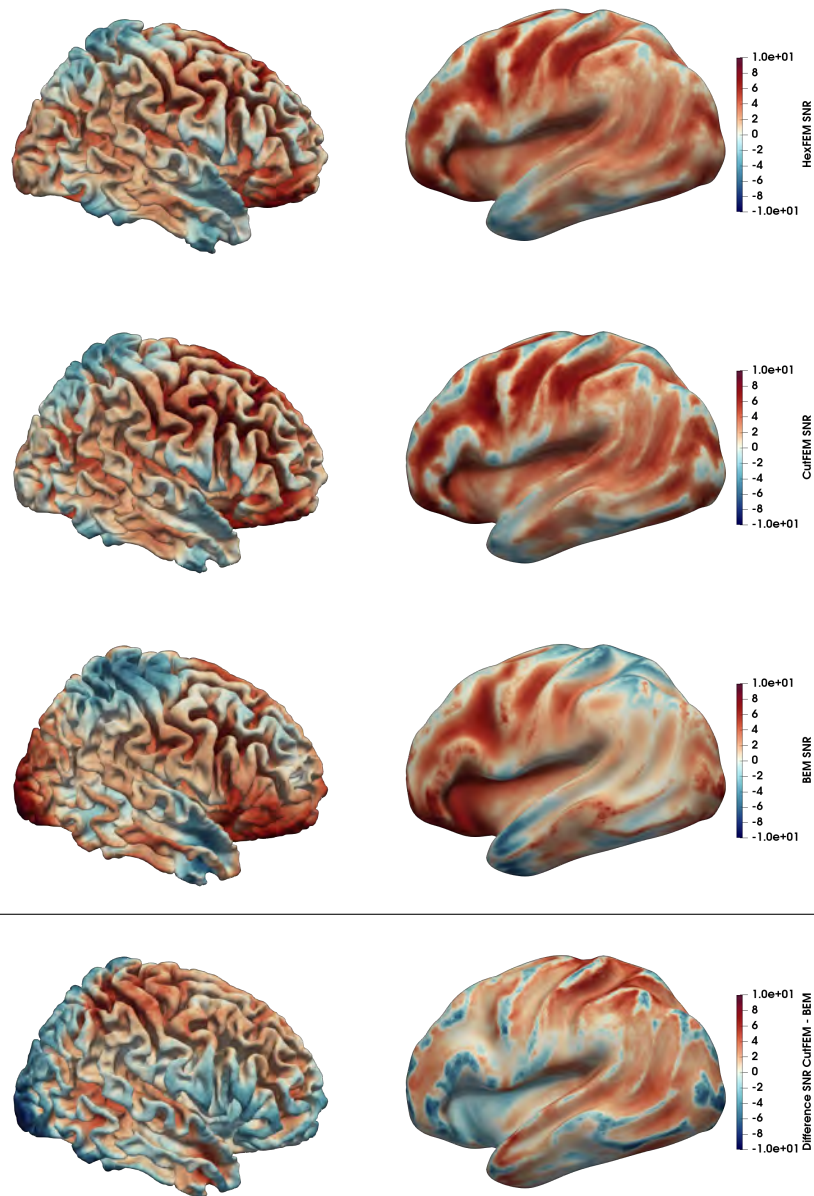
FIGURE 7.11: Signal-to-noise ratio (SNR) induced by quasi-radial sources with 4 nAm amplitude. Upper 3 rows: SNR maps for 6C-HexFEM, 6C-CutFEM, and 3C-BEM on MNI normalized cortex and inflated cortex. Bottom row: Difference between 6C-CutFEM and 3C-BEM SNR. Scaled from -10 to 10 dB.

Impact on tDCS stimulation outcome

In our final analysis of this chapter, we want to investigate how much of an impact the differences in source reconstruction have on the computation of optimized stimulation caps for tDCS. Multi-channel tDCS caps are calculated in a manner that optimizes the directionality (DIR), meaning the scalar product between the normalized target vector η at target position x_0 and the induced current density vector. The tDCS forward problem is solved at x_0 for a set of s predefined stimulation electrode positions on the scalp. The
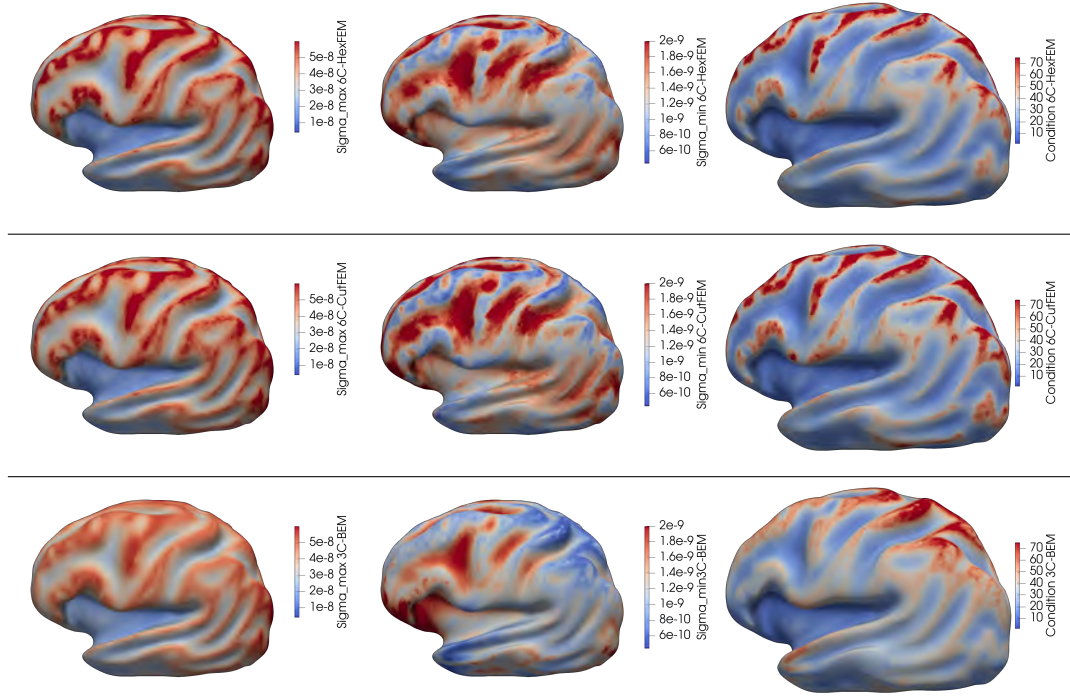
FIGURE 7.12: Largest and smallest singular value and Lead field condition interpolated onto inflated MNI cortex. Top row: values for 6C-HexFEM, center row: values for 6C-CutFEM. Bottom row: values for 3C-BEM.

result is a tDCS matrix $C_{x_0} \in \mathbb{R}^{(s-1)x3}$ whose i-th column contains the current density vector induced at x_0 by a ± 1 mA stimulation of electrode i. The 0-th electrode is the cathode and is implicitly modeled, hence there are only s-1 columns. For an arbitrary current pattern $q \in \mathbb{R}^{s-1}$, the directionality in the target is then defined as DIR $= \eta C q$. The stimulation strength at the 0-th electrode amounts to $q_0 = -\sum_i q_i$, implying that the injected current pattern adds to zero. To optimize the stimulation cap over possible current patterns q, we use the distributed constrained maximum optimization (D-CMI). We maximize the directionality given the side constraints that the total injected current does not exceed 2 mA, and that no single electrode has more than 1.5 mA. A dampening term $\lambda ||q||_2$ is added to spread the current over 8 electrodes. The reasoning here is that we want to further limit the excitation of non-target brain tissue. The dampening term forces us to use 8 total electrodes at a minimal expense of directionality. λ is gradually increased until 8 different electrodes are used, while 8 is simply the number of possible electrodes in the stimulation device that is used at our lab. The full optimization approach is then stated as

$$\max_q \eta C_{x_0} q - \lambda ||q||_2$$

$$s.t. \, |q_0| + ||q||_1 = 4, \; ||q||_0 \leq 1.5.$$

For more information about constrained maximum intensity optimization, see Dmochowski et al., 2011. For more information on the D-CMI see Khan et al., 2019.

FIGURE 7.13: Relative changes in directionality (top) and target intensity (bottom) when using changing stimulation caps. On the x-axis are the assumed true targets. Each boxplot then contains each subject's change in DIR/IT if a different stimulation cap is used.
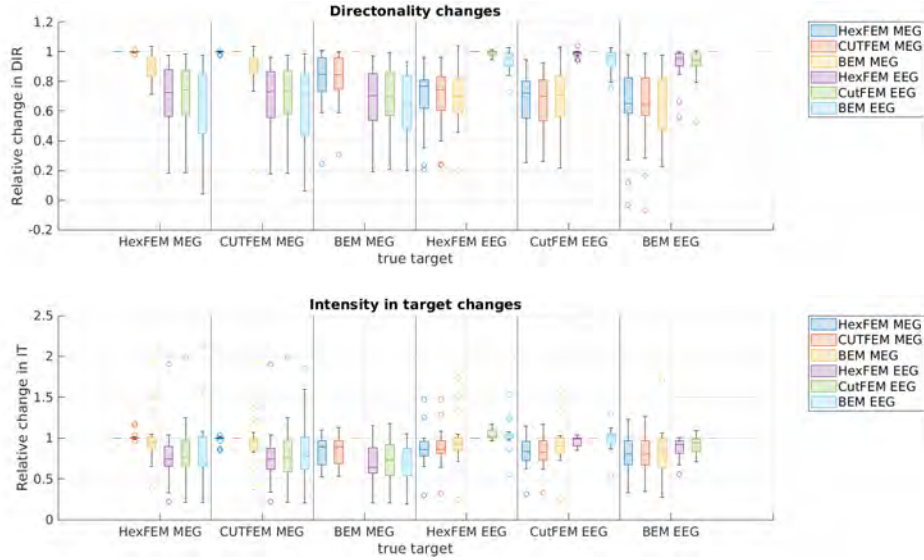
We will now analyze two metrics, the directionality (DIR), and the intensity in target (IT). The IT measures the strength of the current density $||C_{x_0}q||_2$. For this chapter, we will not focus on the differences that arise from calculating C_{x_0} using different forward approaches such as CutFEM or hexahedral FEM. Rather, we want to focus on the impact of changing the target. Based on our P20/M20 reconstructions, we calculate 6 stimulation patterns for each subject. One each for MEG using the reconstructions from 6C-CutFEM, 6C-HexFEM, 3C-BEM, and another one each for the EEG. We therefore have 6 targets x_{1-6}, 6 tDCS matrices $C_{x_{1-6}}$, and 6 current patterns q_{1-6}. In a second step, we then calculate the directionalities $\eta_{x_i} C_{x_i} q_j$ and target intensities $C_{x_i} q_j$ for $i = 1, ..., 6$, $j = 1, ..., 6$. Note that each C-matrix is calculated based on the geometry-adapted hexahedral FEM model.

The results can be seen in Figure 7.13. and can be interpreted as follows. On the x-axis, we see the targets x_{1-6}. The boxplots then indicate relative changes in DIR/IT if the stimulation pattern q_j that corresponds to the color bar stated in the legend was chosen. By relative changes, we mean that for each target x_i the DIR/IT values have been normalized by the values induced when using the "correct" stimulation pattern q_i. The results can therefore be considered as relative reductions/increments in DIR/IT of a true target when using a stimulation cap that is based on a faulty source localization.

We see that the overall differences between forward modeling approaches are dominated by the differences between EEG and MEG-based stimulation caps. Using an EEG pattern on an MEG target resulted in an average reduction in DIR of 43.45 percent and 22.53 percent IT. Using a BEM-based cap on a CutFEM-based target reduced DIR by 9.67 percent and IT even increased by 1.81 percent. When using a HexFEM-based pattern, the reduction in DIR decreases to 0.49 percent and IT increases by 2.76 percent. It can overall be stated that the reduction in directionality is greater than the potential differences in IT. That the IT is less sensitive to the target selection is sensible as all methods localize to roughly the same area. The directionality also depends

on the target orientation, making it the more sensitive parameter.

DIR values slightly larger than 1 can be explained by the use of the regularization factor λ. If λ has to be chosen larger to obtain an 8-electrode spread, the effect on the DIR is stronger. A CutFEM-based cap may use a smaller *lambda* value to reach 8 electrodes than a HexFEM-based cap, and the CutFEM pattern may then induce a larger DIR at the HexFEM target location due to its lower dampening. The effect is small, however, with the largest increase in DIR due to a different cap being 4.1 percent.

We notice that even though there was a slightly higher coherence between 3C-BEM-based EEG and MEG source localization, this did not translate to a higher coherence in either DIR or IT simulation outcomes.

7.4 Conclusion

In this chapter, we transitioned from controlled spherical to realistic state-of-the-art, six-compartment head models. Additionally, we no longer made statements about differences in the lead field matrices but investigated the reconstruction of real EEG/MEG data. For comparison, we chose two established EEG/MEG forward modeling approaches: A six-compartment geometry-adapted hexahedral finite element method and a three-compartment boundary element method. The recorded data stems from a combined EEG/MEG measurement of somatosensory evoked fields/potentials, induced by electric wrist stimulation. The first somatosensory peak, the P20/M20, a very focal signal that has been studied extensively in the literature, was analyzed. To add stability to our findings, the analysis was performed over a group of $n = 19$ participants.

In both EEG and MEG, we found that the differences in reconstructed dipole location and moment were smaller when comparing the six-compartment FEM approaches than when comparing a six-compartment and a three-compartment approach. This corresponds to Vorwerk et al., 2012, where a comparison of three-compartment BEM and FEM models was performed. Our findings concerning differences between three- and six-compartment models are in line with the findings in Antonakakis et al., 2019, who also investigated the use of different stimulators to elicit the P20/M20 response.

The average differences between 6C-CutFEM and 6C-HexFEM are small. In individual cases, however, differences between 6C-CutFEM and 6C-HexFEM exceeded a centimeter in location and 20 degrees in orientation.

When compared against an anatomical atlas, we found that all three methods localize close to or into the Brodmann area 3b which is host to the neurons that generate the P20/M20. This is a desirable outcome as it states that all three methods lead to roughly similar results. We found that CutFEM reconstructed closer to the post-central gyrus than the other two methods, an effect that was more pronounced in MEG than EEG. Atlas comparisons rely on a nonlinear registration to a template and come with a level of uncertainty that is difficult to quantify. However, we see that the MEG reconstructions are overall more in line with the atlas than the EEG. As the MEG reconstruction is overall considered to be spatially more accurate than the EEG, this

gives us a first indicator that CutFEM reconstructions may lead to more reliable results. Of note, an MEG-based three-compartment BEM reconstruction was on average only as close to the post-central gyrus as either EEG-based six-compartment approach. The subjects that had the highest distance to the post-central gyrus in 6C-HexFEM or 3C-BEM were also the subjects where the difference to 6C-CutFEM was highest. We therefore have a first indicator that CutFEM reconstructions are more reliable than the two alternatives.

The second part of this chapter was concerned with the analysis of residual variances (RV), meaning the proportion of measured data that is left unexplained by our reconstruction. Here, we saw that the average RV is lower for the six-compartment than for the three-compartment methods. The effect is statistically significant and more present in MEG than in EEG, where the overall RVs are higher for all approaches. Additional anatomical information therefore improves the fit to the measured data. To assess whether this is due to a better fit to the actual signal or due to an overfitting of noise, we performed several investigations.

First, we derived a way to calculate the expected residual variance based on additive noise. This expected RV is based on the prestimulus interval and gives an estimate of how much RV we would expect given a perfectly accurate forward model. We found that this value is overall lower than the residual variance observed in our reconstructions, indicating that we are at least not overfitting additive noise here. However, we cannot make statements regarding the inaccuracy of our reconstruction incurred by e.g. erroneous sensor registration or data preprocessing.

We then introduced a measure for source separability by quantifying how quickly the residual variance increases with increasing distance to the reconstruction optimum. We found a steeper increase in 6C-CutFEM than in 6C-HexFEM, which in turn rose more steeply than 3C-BEM. From this result, we can state that the spatially more homogeneous BEM lead field is less able to distinguish between proximate source candidates. Therefore, there are parts of the signal that are unique to the neural generator's location and would not exist if a proximate source was active instead. If our lead field cannot properly distinguish the actual and a proximate source, these signal parts would be left unexplained, resulting in a higher residual variance and possibly explaining the difference in RV between the three- and six-compartment approaches.

The following investigation was concerned with the sensitivity to quasi-radial sources. For each source location, the quasi-radial orientation was derived through singular value decomposition, and a signal-to-noise ratio (SNR) was calculated based on the definition in Piastra et al., 2021; Goldenholz et al., 2009. This was done for all three forward modeling approaches and all subjects. The results were translated into MNI space and interpolated onto a cortical surface.

We found that six-compartment methods are insensitive to quasi-radial sources on gyral crowns, but the sensitivity increases rapidly when moving down the gyral walls. The 3C-BEM SNRs depended more on the position of the gyrus that the source was on rather than the position of the source on the gyrus. As mentioned in the chapter on neurophysiology, the generators of the EEG and MEG signal are pyramidal cells in layer 5 of the cortex and aligned normally to the cortical surface (Murakami and Okada, 2006b). Our

results therefore align with the fact that predominantly quasi-radial sources are not visible in the MEG. Piastra et al., 2021 performed a similar SNR analysis using sources aligned with the cortical normal and also found a higher sensitivity to sources on the gyral walls when using six-compartment models rather than three-compartment models. With our study, we can now add that this higher sensitivity is not entirely due to quasi-tangential components but that quasi-radial contributions can also be reconstructed. In practice, this means that a source located on the gyral wall and whose cortical normal is around 10 degrees out of the quasi-tangential plane produces an MEG signal from which an accurate estimate of the same 10 degrees may be derived even in the presence of noise. This leaves us with another indicator that the lower residual variance in six-compartment FEM is not due to noise overfitting. Rather, it may be due to an accurate reconstruction of the quasi-radial signal components present in the data.

The differences between 6C-CutFEM and 6C-HexFEM were smaller than three-compartment vs six-compartment differences, but all the effects mentioned are more pronounced in CutFEM than in HexFEM. Where 6C-CutFEM shows very distinct SNR-troughs on the gyral crowns, the 6C-HexFEM SNR maps are slightly more smeared.

In addition to SNR-based comparisons, we investigated the lead field conditioning for each method, meaning the ratio of largest to smallest singular value. Ahlfors et al., 2010 found that the average conditioning of a 3C-BEM model is 16.67, corresponding to the value of 16.92 in this study. 6C-CutFEM has an average condition of 14.08, slightly higher than 6C-CutFEM's 13.89. We found that with increasing distance to the head surface, the radial singular value increased in strength while the quasi-tangential ones decreased, resulting in overall lower signal strength and corresponding with the MEG's decreasing sensitivity when increasing source depth.

As mentioned, a central goal of this chapter was to determine the reliability of MEG-based dipole orientations. The dipole moment is of particular importance when the source is used as a target for subsequent tDCS stimulation (Dmochowski et al., 2011; Antonakakis et al., 2024b; Khan et al., 2022). With our SNR analysis, we gave strong evidence that quasi-radial contributions are reconstructable using six-compartment modeling and CutFEM in particular. In principle, there are two regions, where the cortical normal is aligned with the quasi-radial direction, the gyral crown and the sulcal fundus. While the MEG is insensitive to gyral crowns, six-compartment modeling may aid in reconstructing bottom-of-sulcus signals. Focal cortical dysplasias for example are predominantly located at the bottom of a sulcus (Liu et al., 2019). In the next chapter, we will give more context on epilepsy scenarios where an MEG-based target selection is necessary or preferable.

It has to be noted that the noise levels present in the study are comparably low after averaging over almost 2000 trials per subject, making this a very controlled scenario. To balance this, we also chose a comparatively low estimate of 4 nAm for the source strength. Investigations with higher noise scenarios have not yet been performed and may be part of a future analysis.

Also, we only investigated somatosensory evoked potentials here. In particular, the 3C-BEM approaches' SNR map varies significantly across cortical regions. An analysis of visually evoked potentials (VEP) may therefore yield different results. VEPs would also serve as a better basis for investigating

subject positioning as was done in Justin K. Rice et al., 2013. In particular, a comparison between six compartment CutFEM and a tetrahedralized FEM model that features nested tissue compartments may be of interest.

We used a radial setup of gradiometers in this study, as that is the default configuration of the used CTF system. Positioning the gradiometers in a tangential fashion increases the MEG-sensitivity to quasi-radial sources as was shown in Haueisen et al., 2012. Performing a similar sensitivity analysis with tangential gradiometers may be particularly interesting with the introduction of optically-pumped magnetometers (OPM). With OPMs, the magnetic flux may be simultaneously measured in multiple directions at the same sensor location (Brookes et al., 2021).

Independent of the application, the differences in location of up to a centimeter and the differences in orientation of more than 20 degrees justify the additional computational load of finite element approaches and Cut-FEM in particular. The better correspondence with an anatomic atlas, decreases in residual variance, improvements in source separability, and sensitivity to quasi-radial sources all suggest that the reconstructions based on six-compartment models and CutFEM in particular are more reliable than those achieved using three-compartment BEM models. However, in a direct comparison of EEG and MEG reconstructions, we did not find a higher coherence of the two modalities when using six over three compartments. The differences with respect to a simulated tDCS stimulation were small. Here, the choice of basing the stimulation on an EEG or an MEG reconstruction dominated the choice of the numerical forward model.

Chapter 8

Source reconstruction and tDCS cap optimization in epilepsy patients

In the previous chapters, we investigated CutFEM's performance in controlled spherical scenarios and a group study of somatosensory evoked potentials. They were concerned with the accuracy or reliability of CutFEM forward modeling. The final parts of this thesis are concerned with its application in epilepsy diagnostics and therapy through transcranial electric stimulation. Epilepsy is one of the most common neurological diseases with around 50 million patients worldwide (Leonardi and Ustun, 2002). Classical treatment options are medication or invasive surgery. Both have a limited success rate and possibly severe side effects. About one third of patients have refractory epilepsy, i.e. they have persistent seizures under medication (Beleza, 2009). A surgical excision first requires an accurate localization of epileptogenic tissue and the surgeon has to be very conservative in not damaging healthy tissue. Around 60 percent of epilepsy surgeries in patients with focal cortical dysplasias (FCD) result in complete seizure freedom, also called Engel class 1A (Veersema et al., 2019).

EEG, MEG and tDCS may aid in the diagnosis and treatment of epilepsy in multiple ways.

The presence of interictal epileptic discharges (IEDs or spikes) in EEG or MEG measurements serves as an indicator for the diagnostics of epilepsy but may also serve as an aid in guiding invasive diagnostics and subsequent surgery. In Tassi et al., 2010, 30 % of surgically treated epilepsy patients had FCD, highlighting their importance in epilepsy treatment. However, experts often fail to recognize FCDs based on the MRI alone. Providing a region of interest significantly increased the detection rate in Wehner et al., 2021. In Rampp et al., 2019, it was shown that the seizure freedom after surgery was significantly more probable if the tissue identified by MEG source localization was fully resected. In Antonakakis et al., 2024a, a focal cortical dysplasia was identified as a resection target only after a combined EEG/MEG source localization.

TDCS on the other hand is currently investigated as a non-invasive treatment option (Yang, Shin, and Hong, 2021; Kaufmann et al., 2021; Antonakakis et al., 2024a). A typical setup for tDCS is a bipolar stimulation, one cathode, and one anode. The cathode is then placed over the target zone (identified by fMRI, EEG/MEG, patient semiology, etc.) to inhibit epileptic activity. This procedure may neglect the orientation of the induced electric

fields. A higher level of personalization may be achieved if the stimulation montage is optimized in a manner that the introduced currents directly oppose the measured epileptic EEG/MEG data. Calculating such optimized stimulation caps can increase the intensity of the stimulation in the target and reduce side effects (Dmochowski et al., 2011; Khan et al., 2019). Beumer et al., 2022 outline a workflow to create such personalized montages for epilepsy patients. Spike data is measured by EEG and reconstructed using a dipole-fit algorithm that determines a location and an orientation, much like the dipole scan we applied in the previous chapter.

Choosing EEG or MEG for source localization depends on several factors. While the EEG has in theory no sensitivity bias towards any source direction, gyral crowns may produce stronger quasi-radial signals due to their closer proximity to the sensors. Also, as EEG and tDCS solve an almost identical problem, one has a direct correspondence between source localization and optimized stimulation setup. The downside is a stronger dependence on accurate volume conductor modeling.

An epilepsy-specific issue is that neither modality is guaranteed to show all the spikes. In Iwasaki et al., 2005 and Knake et al., 2006 it was found that 18 and 13 percent of epileptic patients display spikes in the MEG, but not in the EEG.

There is therefore no conclusive answer as to whether one can base a tDCS stimulation on EEG or MEG source reconstruction or even a combination of the two. Rather, the decision has to be made on a patient-to-patient basis.

This is the first of two chapters that are concerned with epilepsy. In the first chapter, we will introduce two patients, their patient history and semiology, and notable particularities concerning volume conductor modeling. Similar to the group study from the previous chapter, we will investigate the impact of different forward modeling approaches on the reconstruction and the final stimulation caps.

One of the patients proceeded with the tDCS stimulation. The second chapter covers the stimulation paradigm and outcome.

8.1   Patient 1

Patient history and preliminary data analysis

Patient 1 is a 36-year-old male with a long history of epilepsy. He had a resection in the left somatosensory cortex in 2008. From the histopathology, a focal cortical dysplasia type 2b was confirmed. As of December 2022, he still suffers from refractory epilepsy. His prescribed antiseizure medications are Briviact, Ontozry, and Apydan extent. His attending epileptologist describes his seizures as an initial sensation in the head, followed by sensations in the right arm and behind the eyes, like a wave or a flickering. Later, the patient reports an increased sensitivity of the fingers 4 and 5 of the right hand. The entire seizure lasts about 60 seconds and is not accompanied by motor impulses, a decrease in reaction speed, or loss of perception. Seizures occur multiple times per week, in particular on stressful days.

In 2022, a one-hour combined EEG and MEG measurement was performed in Münster. During the first 10 minutes, an electric wrist stimulation was performed to elicit P20/M20 components in the right somatosensory
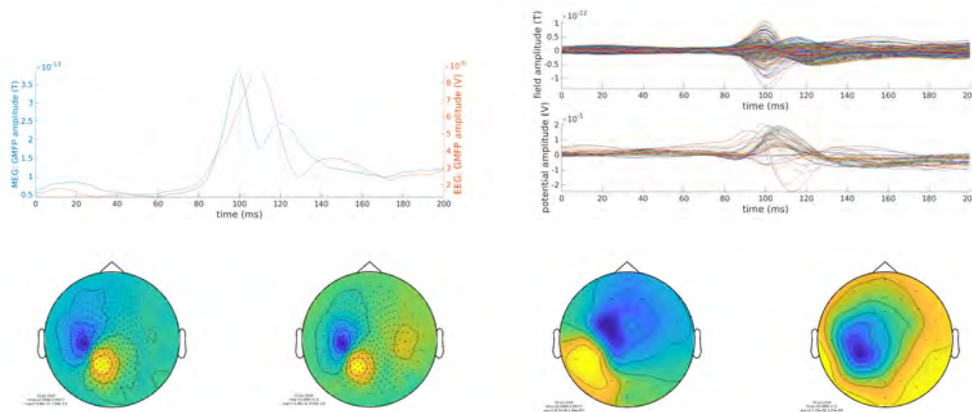
FIGURE 8.1: EEG and MEG averaged spike markings for Patient 1. Top row: Global mean field power (left) of EEG (red) and MEG (blue). On the top right are butterfly plots of MEG (top) and EEG (bottom). The spike peak was selected based on the MEG and is at t = 100 ms. Bottom row from left to right: MEG topography at the spike onset (t = 90 ms) and spike peak, EEG topography in the same order.

cortex. This dataset was used for skull conductivity calibration. Note that his semiology points to a left somatosensory epileptic focus and that is also where the surgery was performed. In Allison et al., 1991, a 59-year-old epilepsy patient underwent excision of the somatosensory cortex. Afterward, no somatosensory evoked potentials could be measured on the cortical surface. However, this patient's resection affected a larger area than the one we investigated here. Additionally, our patient still suffers from epilepsy. We therefore decided to stimulate the right somatosensory cortex instead, as it is unclear how the resection affects the processing of the wrist stimulation. See the previous chapter for more information on skull conductivity calibration and specifics of the EEG/MEG measurement protocol.

A certified epileptologist from Bochum then marked 259 epileptic spikes based on the remaining 50 minutes of MEG data. The patient also suffered from a seizure during the measurement. As his seizures do not lead to involuntary movements, we have the rare opportunity to perform source localization for both spikes and seizures. In this chapter, we will emphasize the reconstruction of spikes and the volume conductor modeling. See the next chapter for an analysis of the seizure data. We used fieldtrip (Oostenveld et al., 2011) to preprocess the data. The steps are similar to the preprocessing for somatosensory evoked potentials. Following a baseline correction we applied a bandpass filter from 1 to 100 Hz, a 50 Hz notch filter including harmonics to eliminate powerline noise, and averaged the data. No spikes were excluded from the averaging process.

See Figure 8.1. for EEG/MEG butterfly plots and spike onset and peak topographies. The spike onset is 10 ms before the MEG spike peak. The MEG shows a clear peak with a distinctly dipolar topography at the spike onset and very limited pre-spike activity. At the peak, we see a dipolar pattern, but also contralateral activity, suggesting propagation. In comparison, the EEG butterfly plot is less clear. The pre-spike noise level is higher, and the sensors differ with respect to their peak time point. Namely, three channels, CP3, C5, and TP7 feature a distinct peak before the other channels do. These

channels are located near the resection hole, possibly explaining their earlier onset and peak compared to the remaining sensors. The EEG topography shifts from a tangential dipolar pattern at the time of the MEG onset to a radial one at the peak. At the EEG peak, the topographies are similar to the MEG peak topographies, with even more contralateral activity visible in the MEG and a more clearly radial pattern in the EEG. The EEG main peak is several milliseconds later than the MEG peak as indicated by the global mean field power (GMFP).

To summarize, we have a single spike scenario and a single dipolar onset that features contralateral propagation at the spike peak. We expect the onset to be due to tangentially oriented pyramidal neurons, as suggested by the EEG topography. Following the onset, quasi-radially oriented neurons synchronize. These are captured more strongly in the EEG than in the MEG, which is confirmed by the global mean field power. The MEG reaches its peak before the EEG when the highest number of tangentially oriented neurons are active. The EEG peak is reached later, at peak quasi-radial synchronization.

For source localization, we expect the MEG to be the modality of choice as the onset appears to be tangentially oriented. The noise level is lower, the peak is more distinct, and uncertainties in the skull modeling, which will be discussed in the next section, have a smaller impact on the MEG than the EEG.

Going back to the results from the previous chapter, patient 1 is an ideal candidate to investigate whether we can track the transition from quasi-tangential to quasi-radial source orientation properly using the MEG alone.

Head modeling

T1- and T2-weighted MRI data was measured following the same protocol as the group in the previous chapter, the only difference being the usage of a 3-Tesla MagnetomTrio MRI scanner (Siemens, Munich, Germany) as the measurement was performed in Münster, not in Lübeck. During the surgical intervention, a portion of the patient's skull had to be temporarily removed. While the removed skull plate was returned after the excision, the patient still has several cranial holes. These have a major impact on the EEG source reconstruction, but also the readability of the EEG itself (Lanfer et al., 2012; Li et al., 2007). Following Montes-Restrepo et al., 2014, a computer tomography (CT) image was measured, and used to model the patient's skull.

See Figure 8.2. for a depiction of the resected brain area and the cranial defects. From the T2 image, we see that the area of the resected brain tissue has is indistinguishable from cerebrospinal fluid (CSF) and is therefore modeled accordingly. Modeling the cranial holes is a more challenging task. As the surgery was in 2008, we have no exact information about the material that was used to fill the holes. Studies that analyze the effects of cranial holes on the EEG typically either simulate a variety of conductivities or model them as scalp/muscle tissue (Vanrumste et al., 2000; Lanfer et al., 2012). Feedback from a neurosurgeon suggests that the holes are typically filled with fat tissue or bone dust. Whether these are still present 12 years later or whether skin/scar tissue has replaced them, is difficult to determine. From the CT, we
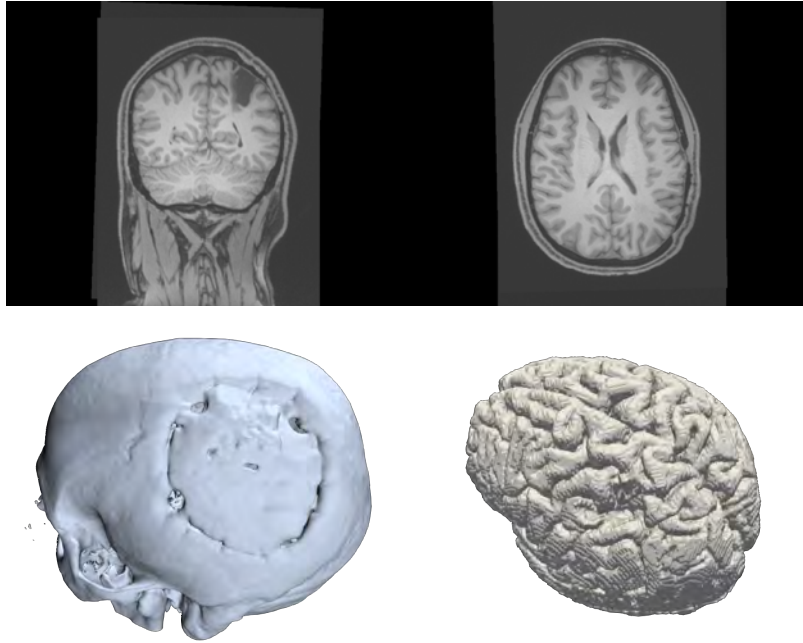
FIGURE 8.2: Head modeling for patient 1. Top row: coronal and axial T1 slices. Note the resected area in the coronal slice and the light-shaded areas connecting the scalp and brain in the axial slice. Bottom row: CT-based skull compacta segmentation (left) and T1-based gray matter segmentation (right).

see no difference between scalp and holes. Neither the T2 nor the T1 show clear differences between the scalp tissue and the tissue in the cranial holes. After consultation with several physicians, we decided to model the holes as scalp tissue. This was also the procedure in Antonakakis et al., 2024a, where another subject is described that underwent a similar epilepsy diagnosis and subsequent tDCS stimulation as patient 1.

Following the analysis pattern from the previous chapter, we again compute lead fields based on the three different forward approaches. Six compartments (Gray matter, white matter, CSF, skull spongiosa, skull compacta, and scalp) for CutFEM and geometry-adapted hexahedral FEM, and three compartments (brain, skull, scalp) for BEM. CutFEM-based reconstructions will again be referred to as 6C-CutFEM, hexahedral results as 6C-HexFEM, and BEM results as 3C-BEM. The six-compartment models accurately model the cranial holes, the fieldtrip-openmeeg pipeline used for 3C-BEM requires nested surfaces, hence all skull holes have been closed here. The source space is again a 2 mm spaced regular grid that conforms to the venant condition of 6C-HexFEM, resulting in 16752 total sources.

As mentioned, somatosensory evoked potentials/fields were measured in this patient, allowing for EEG skull conductivity calibration (Antonakakis et al., 2020b; Schrader, 2022). The calibrated skull conductivity values for 6C-CutFEM, 6C-HexFEM, 3C-BEM are 0.00084, 0.00083 and 0.0012 S/m respectively. See the section on data acquisition and head model creation from the previous chapter for more information on the head model/lead field creation and skull conductivity calibration.

Source reconstruction

For inversion, we again use the dipole scan described in the previous chapter. As mentioned, we are interested in tracking the transition from quasi-tangential to quasi- radial source in the MEG data. To do so, we perform a separate dipole scan for each data sample ranging from the MEG onset 10 ms before the MEG peak to the EEG peak which is 10 ms after the MEG peak. The results can be seen in Figure 8.3.

From the EEG reconstructions, we see that the localizations start tangentially near the resection before moving to deeper areas with a quasi-radially inward pointing orientation. This behavior can be seen with all three forward models that were used. However, using the 6C-FEM approaches and CutFEM in particular, the transition is smoother. The reconstructions follow a single line as trajectory while in 3C-BEM, we have three separate spatial clusters.

For the MEG reconstructions, we again performed an SNR-based cut-off of the quasi-radial singular value with an expected source amplitude of 40 nAm, as the global mean field power of the epilepsy peak is about 10 times higher than for the M20. See the previous chapter for more information. The MEG reconstructions are more eccentric than the EEG reconstructions. In particular, the transition to deeper areas is less pronounced than in the EEG case. Only the 3C-BEM reconstructions feature a similar depth profile in EEG and MEG at later stages. Note however that there is a significant amount of secondary activity present in the MEG data at all time points after 100 ms, with MEG residual variances increasing to more than 40 % in all three models at the EEG peak. MEG residual variances at the onset are 11.06, 10.27 and 9.62 % for 6C-CutFEM, 6C-HexFEM, and 3C-BEM respectively. MEG peak RV's are 2.99, 2.12, and 1.93 %.

In 3C-BEM, the SNR-based cut off was performed at all time points before 95 ms, a transition from quasi-tangential to quasi-radial dipole orientations can therefore not be investigated. The final reconstructions based on the FEM models included radial orientations and the temporal transition from quasi-tangential can be seen in both sets of reconstructions.

The MEG magnitudes from MEG onset to peak increased from 90.11 to 171.8 nAm in 6C-CutFEM, from 132.5 to 211.9 nAm in 6C-HexFEM, and from 152.3 to 240.7 nAm in 3C-BEM. The increase in global mean field power and dipole amplitude is therefore best matched by 6C-CutFEM. Notably, the dipole strengths at the EEG peak are still above 100 nAm for all three models (100.1 for 6C-CutFEM, 128.8 for 6C-HexFEM, and 155.8 for 3C-BEM). A blow-up due to erroneous reconstruction of quasi-radial noise components is not apparent from the reconstruction magnitudes.

The EEG magnitudes from MEG onset to MEG peak to EEG peak transition from 154,7 to 221.1 to 219.5 nAm in 6C-CutFEM, from 123.0 to 207.5 to 197.2 nAm in 6C-HexFEM, and from 203.4 to 256.4 to 458.7 nAm.

The EEG is more sensitive to deeper areas than the MEG (Piastra et al., 2021). As the spike activity appears to transition from a quasi-tangential source to a deep quasi-radial one, this could explain the different peak profiles in EEG an MEG. The MEG peaks at peak tangential synchronization, while the deep quasi-radial peak is less present in the MEG.
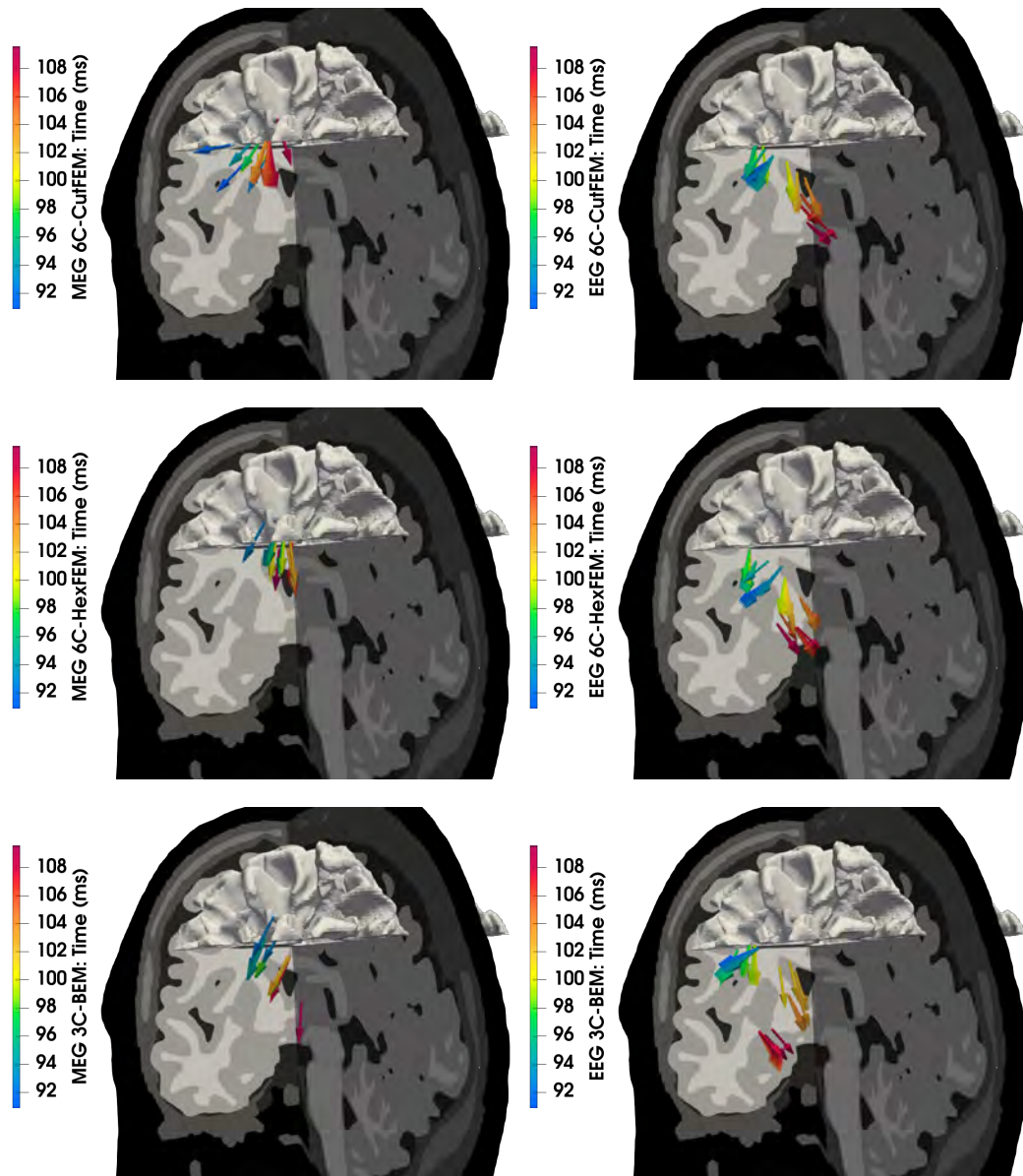
FIGURE 8.3: MEG and EEG dipole scan results for epilepsy patient 1. MEG
on the left, EEG on the right. Top row: 6C-CutFEM-based results. Center row:
6C-HexFEM-based. Bottom row: 3C-BEM-based. One arrow per data sam-
ple, coloration based on time with respect to MEG peak at t = 100 ms. White
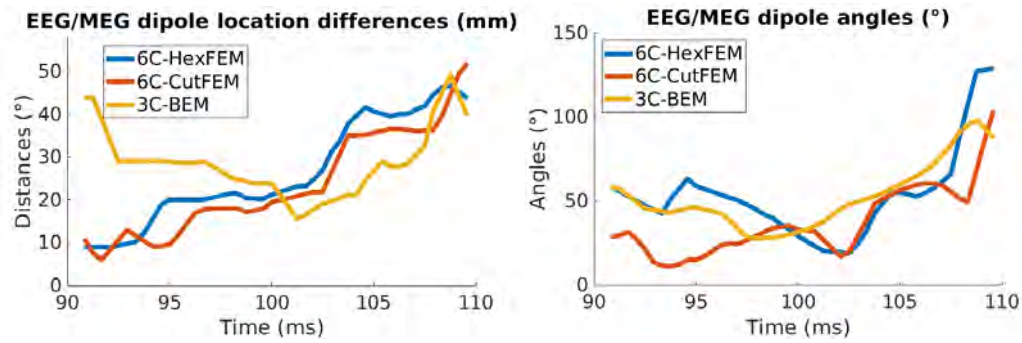matter surrounding the resection area outlined at the top of each image.

FIGURE 8.4: Differences between MEG and EEG dipole scan results for epilepsy patient 1. X-Axis: Time in miliseconds, Y-Axis: Location differences/Angles. Angles in degree on the right, distances in mm on the left. Differences when using 6C-HexFEM in blue, when using 6C-CutFEM in red, 3C-BEM in yellow.

Before comparing tDCS optimization results, we now look at the alignment of EEG and MEG reconstructions by calculating the angles and distances between EEG and MEG dipole separately for each forward method. The results can be found in Fgiure 8.4. In the time-range between MEG onset and peak we see that there are significant differences between the three methods. Location differences below 10 mm can only be found here and only in the six-compartment methods. 3C-BEM differences start at over 4 cm and gradually decrease with increasing time. 6C-CutFEM and 6C-HexFEM feature similar distances at the onset, but 6C-HexFEM differences increase more rapidly after that. We see that near the MEG peak, both the location and the angle of the reconstructed dipoles are similar at around 20 mm and 35 degrees. With increasing time, the MEG and EEG reconstructions diverge. This behavior is more pronounced in the six-compartment methods than in 3C-BEM. The angles between EEG and MEG localizations are massively lower near the MEG onset when using 6C-CutFEM rather than the other two methods with angles around 10 degrees vs 45 and 63 degrees at half the rising flank.

For a source localization of epilepsy activity, one typically chooses a timepoint at half the rising flank of the spike (Antonakakis et al., 2024a; Aydin et al., 2014; Lantz et al., 2003). The intent in doing so is to obtain a sufficiently large signal-to-noise ratio with limited propagation. We therefore see the biggest alignment differences between our methods at the most important time-point for source reconstruction (t = 95 ms).

tDCS optimization

Our final analysis for patient 1 is concerned with the creation of multichannel optimized tDCS caps. The procedure for the calculation of these caps is congruent with the description in the previous chapter. We use the distributed maximum intensity (D-CMI) approach based on Khan et al., 2019 to distribute the current over a total of 8 stimulation electrodes out of 74 possible positions that are based on the EEG1010 system. We use twice the injected current (± 4 mA), and a per electrode limit of 2 mA.
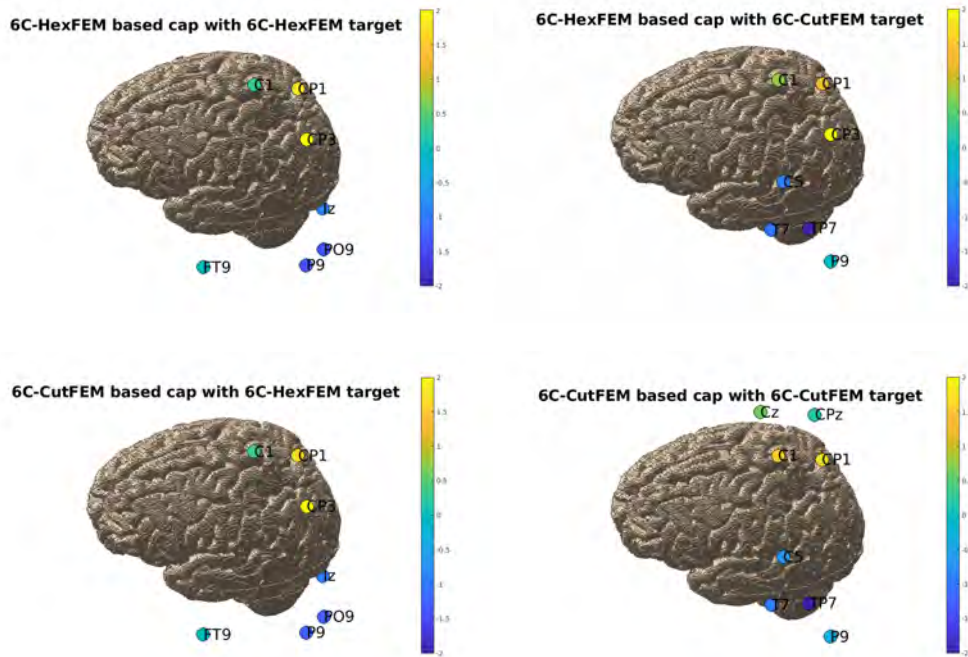
FIGURE 8.5: tDCS optimization caps from 6C-CutFEM and 6C-HexFEM forward solutions. Depicted are cortical gray matter, stimulation electrode labels, positions are colored based on current strength (mA) at the respective electrode. Top row: Caps using 6C-HexFEM for tDCS forward solutions. Bottom row: 6C-CutFEM based tDCS forward solutions. Left side: Targets selected based on 6C-HexFEM MEG lead fields. Right side: Targets based on 6C-CutFEM MEG reconstructions.

As targets, we select the 6C-CutFEM and 6C-HexFEM MEG reconstructions at half the rising flank (t = 95 ms). TDCS optimization matrices are calculated using both the six-compartment hexahedral mesh and CutFEM. Note that in the previous chapter, we only used tDCS forward results from the hexahedral mesh, not CutFEM. In this chapter, the tDCS forward problem is solved using both hexahedral and CutFEM. Four optimized caps are then calculated, two that use the CutFEM-based tDCS matrix and either the 6C-CutFEM or 6C-HexFEM-based dipole reconstruction as target and two that use the Hexahedral FEM-based tDCS matrix. Calculating four caps allows us to individually quantify the impact that MEG source reconstruction and tDCS forward modeling have on the optimization. No three-compartment method was investigated here, as these are less common in tDCS optimization (Thielscher, Antunes, and Saturnino, 2015). The resulting caps can be seen in Figure 8.5.

When selecting the 6C-HexFEM based MEG target, we see close to no difference in the optimization outcome. The largest difference over all stimulation electrodes between a 6C-CutFEM and a 6C-HexFEM cap is 0.087 mA. The maximum directionality is $0.27 \, \mathrm{A/m^2}$ for 6C-HexFEM and $0.22 \, \mathrm{A/m^2}$ for 6C-CutFEM. Differences are larger when using the 6C-CutFEM MEG target. Here CP3, one of the principal stimulation electrodes when using 6C-HexFEM tDCS is not used in the 6C-CutFEM-based cap. Directionalities are 0.31 vs $0.23 \, \mathrm{A/m^2}$.

Notably, the choice of MEG reconstruction primarily leads to a difference in anode positioning. This is to be expected as the cathodes lie closer to the resection and the targets. A change in orientation therefore corresponds to a change in anode positioning.

For this patient, we can therefore state that the choice of the target dominates the choice of the tDCS forward solver due to the orientation differences.

8.2 Patient 2

Introduction and preliminary data analysis

Patient 2 was 24 years old at the time of data collection in April 2023. He has had a left hemispheric suprasylvian porencephalic cyst since birth and has been suffering from epilepsy since the age of 8. His cyst is presumably the result of a perinal infarction. The brain tissue that died in the process was replaced by CSF. In contrast to patient 1, no focal cortical dysplasia has been diagnosed but his epilepsy may be due to left hippocampal sclerosis. He suffers from gait and cognitive impairments. His attending physician describes his seizures as an initial feeling of dizziness and changes in gaze, sometimes accompanied by a loss of awareness. This initial phase lasts about 1-2 minutes. If the seizure continues, his eyes deviate to the right, and the right side of his body stiffens and starts jerking, followed by a generalized stiffening and jerking all over. The entire seizure lasts about 4-5 minutes. At the point of data collection, no invasive diagnostics/surgery had been performed, his skull should therefore be free of defects. He is currently seizure-free under medication. Whether he is interested in a tDCS stimulation as treatment is at this point unclear.

He underwent a similar measurement protocol as patient 1, with the exception that no combined EEG/MEG measurement was possible as due to his head size he did not fit into the MEG dewar when wearing an EEG cap. Therefore, only MEG data was measured and no somatosensory evoked potentials/fields were measured as there is no need for skull conductivity calibration without the EEG.

This time, the full one-hour measurement was used for spike markings, resulting in a total of 111 spikes. The markings were performed by the same epileptologist who did the markings for patient 1. No seizure occurred during the measurement. Preprocessing was also identical to patient 1, see Figure 8.6. for a butterfly plot of the averaged MEG spike data. We see a central dipolar topography that remains stable throughout the entire peak. The ratio

$$||y_{t=95}/||y_{t=95}||_2 - y_{t=100}/||y_{t=100}||_2||_2$$

marks the change in topography distribution from half the rising flank to spike peak (basically the relative difference measure from before) is also under 8 %. No propagation is visible, again making a single dipole scan the method of choice. The extent of quasi-radial contributions is not foreseeable due to the absence of EEG data.

In the 100 ms before the spike peak, a signal peak that would suggest a deep hippocampal onset could not be found either with or without filtering.
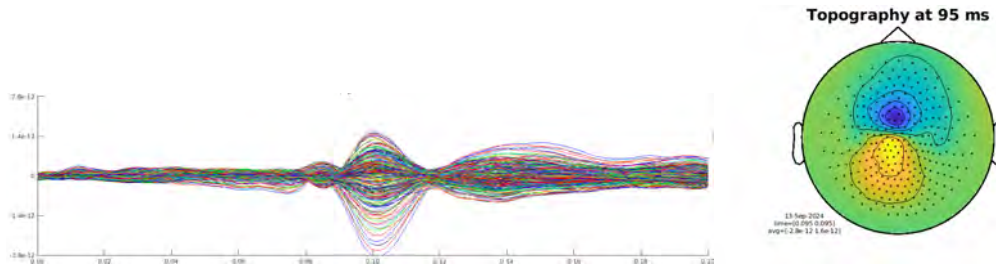
FIGURE 8.6: MEG averaged spike markings for Patient 2. Butterfly plots of MEG (left). The spike peak is at t = 100 ms. Right panel: MEG topography after the spike onset (t = 95 ms)
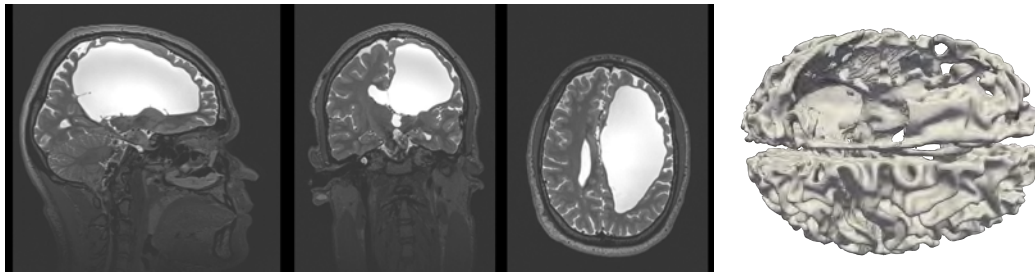
FIGURE 8.7: First 3 panels: sagittal, coronal, and axial T2 slice of patient 2. Right panel: Final white matter segmentation based on T1 image.

Head modeling

T1- and T2-weighted MRIs were measured following the same protocol as patient 1. As mentioned, this patient suffers from a large porencephalic cyst that can be seen in Figure 8.7. The cyst is considered to be filled with CSF and from the T2, we see no difference in contrast between the area of the cyst and the CSF in other areas. Therefore, it was assigned the conductivity value of CSF. CSF-segmentation via our standardized pipeline in SPM12/CAT12 failed. Rather, we thresholded the T2 to obtain the CSF. The gray and white matter could be extracted from the T1 image. However, the thin strip of brain tissue that separates the cyst and the skull could not be segmented automatically and had to be segmented manually. In this area, the distinction between gray and white matter is challenging, hence we decided to simply model it as a layer of gray matter. The binary masks for 6C-CutFEM and 3C-BEM could therefore be set up without further problems but we do not have a tissue probability map for gray and white matter in the area between the cyst and skull. Rather, we calculated signed distance functions (SDF) based on anti-aliasing the binary segmentation results as mentioned in the chapter on head model creation and Whitaker, 2000. We then used the SDF for the area between the skull and cyst and level sets based on tissue probability maps for the remaining head.

Source reconstruction

As the spike has a single dipolar topography, we again use a dipole scan for inverse reconstructions. We analyze the time-range from spike onset to peak, in this patient from 91.7 to 100 ms by again performing a single dipole

scan for each data sample. As mentioned, we do not have an a-priori estimate for the quasi-radial contribution. Therefore, we will perform the entire dipole scanning twice for all forward approaches. Once with only the quasi-tangential components of the lead fields and once with the SNR-based conditional truncation we have been using for patient 1 and the group study (source amplitude for the quasi-radial part is again 40 nAm, SNR-threshold is 3). The difference data $y - L(x_{op}\eta_{opt}$, i.e. the part of the data that cannot bet explained by the source reconstruction, can be visualized as a topography.

In Figure 8.8, we see the reconstructions based on quasi-tangential lead field components only. There is almost no difference between the six-compartment reconstructions. All localizations are almost constant over time, the six-compartment reconstructions are about 2 cm more central than those based on 3C-BEM. Depth differences are visible only at the signal peak, where the six-compartment methods jump to a slightly deeper source. Residual variances at half the rising flank are 16.87, 16.28, and 13.68 % for 6C-HexFEM, 6C-CutFEM, and 3C-BEM respectively. The unexplained data in the right column is notable for two reasons. First, we see that there is a clear quadrupolar activity left unexplained by both six-compartment methods, suggesting that we may have significant quasi-radial activity. The second is that the 3C-BEM is unable to properly explain the two poles in the MEG data, possibly due to the modeling error of not addressing the large CSF-filled cyst. There are almost no differences between the six-compartment methods, with location differences below 4 mm and angles below 7 degrees. Differences between three- and six-compartment methods increase over time, from 20 degrees to almost 60 degrees and from 16.4 mm to 32 mm from onset to peak. Source amplitude are 160.7, 236.4, 153.7 nAm for 6C-HexFEM, 6C-CutFEM, and 3C-BEM respectively.

In our second dipole scan, we admit quasi-radial components if their SNR exceeds a threshold of 3. The results can be seen in Figure 8.9. As expected, we see a marked difference in the unexplained data. The topographies are less clear and a significant amount of noise is visible in the six-compartment reconstructions. The 3C-BEM looks virtually unchanged, quasi-radial components did not change the two unexplained poles from before. Residual variances at half the rising flank dropped significantly in the six-compartment methods, with decrements of 9.34, 8.02, and 4.02 % (6C-HexFEM, 6C-CutFEM, 3C-BEM) again measured at half the rising flank. These decrements are highest in the six-compartment methods. While the amount of unexplained signal power decreased significantly, the dipole orientations are now dominated by the radial component, now pointing radially inward. This behavior is also represented in the source amplitudes, which increased by a factor of 4.6, 2.41, and 1.99 (6C-HexFEM, 6C-CutFEM, 3C-BEM). If we move to the peak, the discrepancy increases as source amplitudes increase to up to 1800 nAm.

To summarize, we have a dataset with a very clear tangential topography where neither secondary activity nor significant noise levels are visible. After reconstructing the quasi-tangential signal components, we are left with quadrupolar topographies that indicate the presence of quasi-radial source contributions. The residual topographies are also clear and free of noise. Allowing quasi-radial orientations into our reconstructions has the desired effect of explaining a large amount of the residual data, but at the cost of
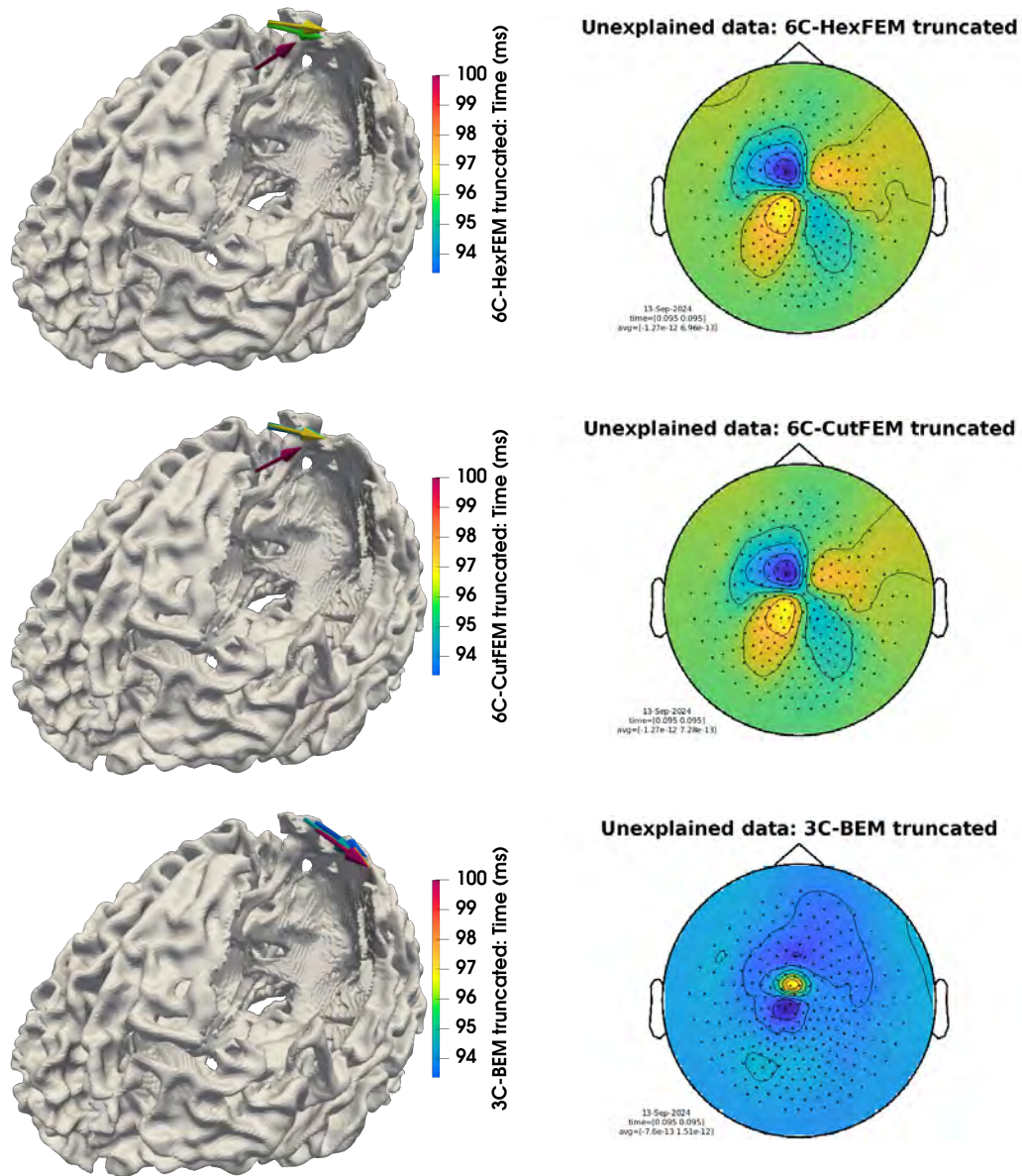
FIGURE 8.8: MEG dipole scan reconstructions for patient 2 using only tangential lead field components. Left column: Reconstructions over time. Right column: data left unexplained by the reconstruction at half the rising flank. Top row: 6C-HexFEM based reconstructions. Center row: Based on 6C-CutFEM. Bottom row: Based on 3C-BEM. One dipole per data sample colored by time-point from 91 to 100 ms.

FIGURE 8.9: MEG dipole scan reconstructions for patient 2 using the SNR-based truncation of quasi-radial components . Left column: Reconstructions over time. Right column: data left unexplained by the reconstruction at half the rising flank. Top row: 6C-HexFEM based reconstructions. Center row: Based on 6C-CutFEM. Bottom row: Based on 3C-BEM. One dipole per data sample colored by time-point from 91 to 100 ms.
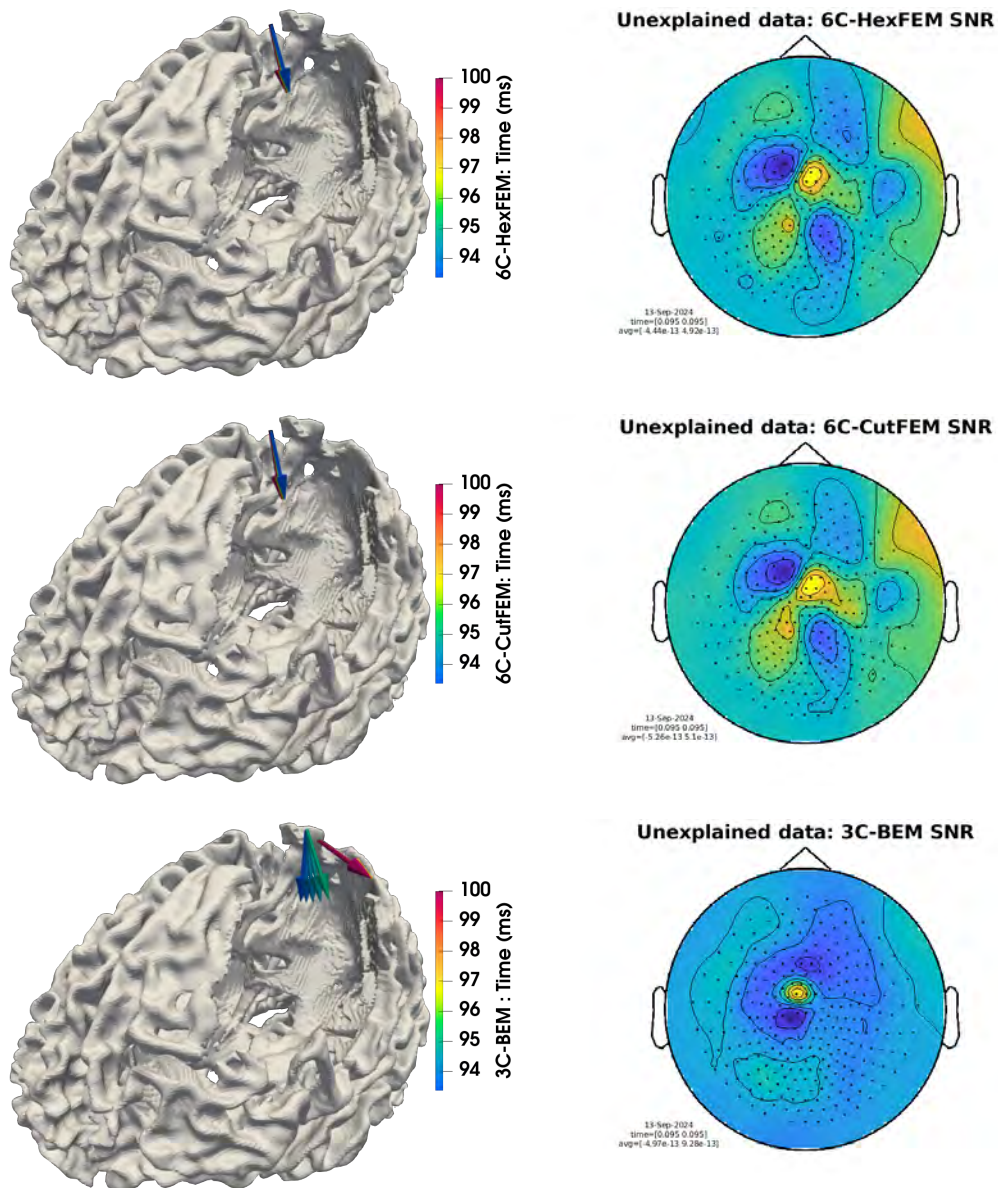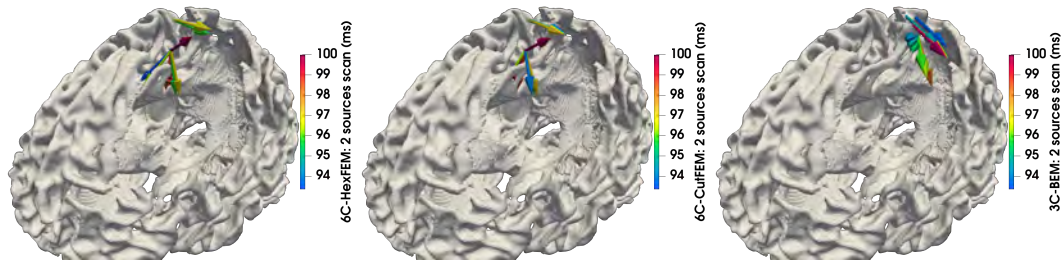
FIGURE 8.10: Two-dipole scan results for patient 2. From left to right: reconstructions based on 6C-HexFEM, 6C-CutFEM and 3C-BEM. One dipole per data sample colored by time-point from 91 to 100 ms.

a massive blow up in the quasi-radial orientation. Also, the quadrupolar topographies are reduced, but not fully explained. There is thus no single dipole in the source grid that properly explains both quasi-radial and quasi-tangential components.

There are three different possible explanations for the observed behavior. First, the true source orientation really is best represented by a quasi-radial dipole. The residual quadrupolar topography is due to inaccuracies in the volume conductor model as we only modeled gray matter around the cyst.

Second, the error is due to source modeling. The measured signal has a large magnitude, suggesting an extended patch of active neurons. The approximation of a single sum-dipole may not hold here.

The last option is the presence of an additional active source. Recall that the patient's semiology indicated hippocampal sclerosis as possible trigger of his epilepsy. A deep quasi-radial source in the hippocampus may be hidden by the eccentric quasi-tangential source that we reconstructed.

Option 1 may be explored by adding a better distinction of gray/white matter and CSF around the cyst. Additionally, measuring and reconstructing EEG data may yield more clarity on the target's true orientation.

For Option 2, investigations may be performed on the inverse or the forward modeling side. We could turn to current density approaches such as minimum norm estimation or perform a patch-dipole scan, where instead of a single dipole, an extended patch of the source grid is admitted to the reconstruction at any time. The center of the patch is then moved over the cortex. Alternatively, multipolar source models could be tested, where the source at a single position is not represented only by the dipole moment, but by quadrupolar moments as well (Beltrachini, 2019).

The last option may be investigated by performing another dipole scan, where we try to reconstruct the deep quasi-radial source. We fix the source reconstructed in the truncated dipole scan and perform a grid-wide scan for the second source. More precisely, for each point in the grid we calculate the pseudo-inverse not for the $sx3$ lead field matrix at that location, but rather add another 3 columns from the truncated lead field at the reconstruction optimum from the truncated scan. The results can be seen in Figure 8.10.

The quasi-radial reconstructions are not located significantly deeper than the initial quasi-radial ones. The hypothesis of an additional deep hippocampal source can therefore not be confirmed based on the quadrupolar signal parts.
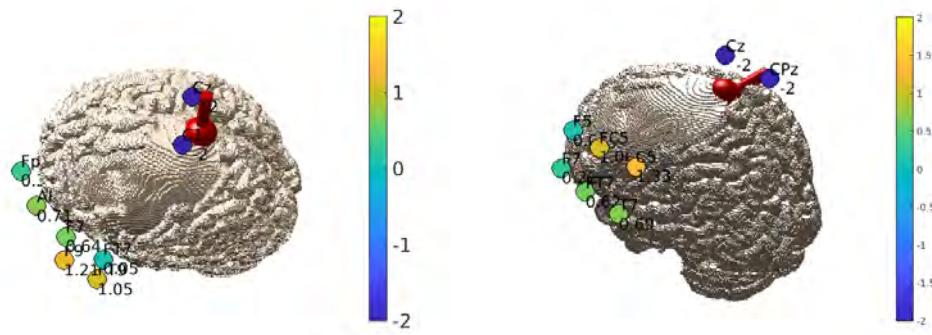
FIGURE 8.11: Optimized tDCS caps for patient 2. Left: target selection based on the SNR-regularized reconstruction. Right: Based on the truncated reconstruction. Stimulation electrodes colored by current strength (mA). Red dipoles indicate the optimization targets, with orientations anti-parallel to the MEG reconstructions.

tDCS optimization

Given the mentioned uncertainties in this patient source reconstruction, any optimized tDCS cap comes with a great deal of uncertainty with respect to the optimal orientation. If the source is a large extended patch with a principally quasi-tangential orientation, the truncated reconstruction may be the optimal target, if its quasi-radial, the SNR-regularized reconstruction may be preferable. In Figure 8.11., we see the 6C-HexFEM based D-CMI optimized tDCS caps for both scenarios.

We see that both optimizations result in similar caps, with the cathodes near the target and the anodes located more fronto-temporal. the Anode placement in the SNR-regularized case is limited by the absence of stimulation electrode below the head. We refrained from showing 6C-CutFEM based caps as well as HexFEM and CutFEM yielded virtually identical results in this patient.

8.3   Conclusion

In this chapter, we transition from evoked potentials/fields in healthy human subjects to spike data from two epilepsy patients with multiple anatomical defects. We again performed reconstructions using lead fields from CutFEM, hexahedral FEM, and BEM.

Patient 1 already had surgery and has therefore cranial holes and a sizeable resection area in his left somatosensory cortex. Patient 2 has hippocampal sclerosis and a porencephalic cyst that covers most of his left hemisphere.

In both patients, we found large differences between reconstructions based on three- and six-compartment lead fields. Where in the group study, we only found differences of around 1 cm, the differences in these patients ranged between 1.5 and 4 cm, highlighting the importance of modeling the defects present in both patients' volume conductors.

In patient 1, both EEG and MEG data are available. A single spike population was marked that has a clear transition from tangential to radial topographies in the EEG. Following up on our investigations with respect to

the reconstructability of quasi-radial sources in MEG, we saw that CutFEM was able to track the transition from quasi-tangential to quasi-radial better than the other two forward methods. Additionally, we found a greater alignment of EEG and MEG reconstructions, especially at half the rising flank. However, we did not see lower residual variances in the six-compartment methods in this patient. As the patient has two defects, future investigation could show whether the cranial holes or the resected brain tissue are responsible for the deviations in the MEG source reconstructions.

When creating optimized multi-channel tDCS caps, it proved to be more relevant which forward method was used for source reconstruction, rather than which forward method was used to solve the tDCS forward problem.

Patient 1 continued with a two-week tDCS stimulation, the procedure and outcome of which are found in the next chapter.

In patient 2, we only have MEG data available. The reconstructed sources are closer to the surface, yet we still see a depth difference between three- and six-compartment forward models at the spike peak. The two six-compartment methods on the other hand yielded almost identical reconstructions.

Performing reconstructions based only on quasi-tangential lead fields left much of the data unexplained. As the residual data appeared quadrupolar, we admitted quasi-radial orientations, resulting in lower residual variance and a blow-up in source strength. Scanning with two dipoles yielded no indication of a secondary deep source. Therefore, the quadrupolar terms are likely due to the extent of the active neuron patch. We set up two tDCS stimulation caps, one with and one without quasi-radial target components. The two caps differ mainly in their anode placement, with cathodes located over the reconstruction targets.

Update from September 17th, 2024: The patient agreed to a tDCS stimulation and an additional EEG topography was provided by his attending epileptologist. The EEG spikes feature a clear radial topography. Source reconstruction in BESA performed by the epileptologists indicated a quasi-radial source orientation at a location matching the reconstructions shown in this chapter.

Aside from this patient's future tDCS stimulation, his data should continue to be investigated for numerous reasons. It may yet be that given more sophisticated inversion algorithms such as RAMUS (Rezaei et al., 2021), an active hippocampal source may be identified. The large extent of the active neuron patch motivates the investigation of non-dipolar source models (Beltrachini, 2019). A follow-up investigation could determine optimal tDCS parameters for an extended cortical area. If the source cannot reasonably be explained by a dipole, then the tDCS optimization should not assume the target to be a dipole either.

Chapter 9

tDCS stimulation of an epileptic patient

In the final chapter, we investigate the effects of transcranial direct current stimulation on the first subject (P1) from the previous chapter, where we analyzed the impact of forward modeling on the reconstruction of epileptic spike activity and the subsequent computation of optimized stimulation caps. The stimulation protocol is based on Antonakakis et al., 2024a. In this double-blind study, a 26-year-old female patient with left-frontal lobe epilepsy was subjected to two weeks of non-invasive tDCS stimulation: one week of active sham stimulation and one week of multi-channel tDCS (mc-tDCS), where the target was selected based on a combined EEG/MEG reconstruction of epileptic spike activity. The mc-tDCS cap was created by applying a distributed constrained maximum intensity (D-CMI) approach. One hour of EEG was recorded both before and after each stimulation and given to three blinded epileptologists who independently marked ictal and interictal events. Findings included a decrease in the number of seizures after mc-tDCS stimulation but also after active sham.

9.1 A seizure-based multi-channel tDCS cap

We performed a similar stimulation and analysis for subject P1 from the previous chapter. However, there is one crucial difference: During the EEG/MEG measurement, P1 suffered from a mild seizure, giving us the rare opportunity to base our mc-tDCS cap on the recorded ictal event rather than interictal spikes. As mentioned, the patient's attending physician describes his seizures as an initial sensation in the head, followed by sensations in the right arm and behind the eyes, like a wave or flickering. Later, the patient reports an increased sensitivity of the fingers 4 and 5 of the right hand. The entire seizure lasts about 60 seconds and is not accompanied by motor impulses, a decrease in reaction speed, or loss of perception. Seizures occur multiple times per week, in particular on stressful days.

There are thus multiple reasons for performing the tDCS-optimization based on his seizure rather than spikes. As the seizures do not lead to involuntary movements, the EEG/MEG data during the seizure is of similar quality as the seizure-free periods and not distorted by muscle artifacts. His high number of seizures per week implies a high probability that there will

FIGURE 9.1: Average EEG and MEG spike activity. Left panels: Butterfly plots and global mean field power (GMFP). Marked peaks are at 100 ms. Right panels: MEG (top) and EEG (bottom) topography averaged over the first half of the peak (90-100 ms)

.

be seizure events during the EEG measurements before and after the stimulation, allowing us to base comparisons on markings from certified epileptologists and not a possibly biased and faulty seizure diary from the patient. Additionally, we can investigate further metrics such as seizure intensity and duration. The downside of a seizure-based mc-tDCS cap is that we no longer have a clear hypothesis for changes in interictal activity.

The following sections are structured as follows: We start by discussing how to create a mc-tDCS cap based on seizure activity and investigate simulation results such as directionality and intensity in target at the reconstructed onsets of both seizure and spike. We proceed with a more thorough explanation of the two stimulation weeks and the recorded data. Finally, we analyze the stimulation outcome regarding changes in both ictal and interictal activity.

Analysis of seizure markings

The patient underwent one hour of combined EEG/MEG measurement in Münster in March 2022. Twenty-five minutes into the measurement, he suffered from a mild seizure that lasted a total of 22 seconds. Based on the measured data, the epileptologist marked a total of 112 separate peaks that occurred during the seizure. The data was preprocessed in fieldtrip (see also the previous section: baseline correction, bandpass filter from 1 to 100 Hz, 50 Hz notch filter to eliminate powerline noise) and averaged, see Figure 9.1.

We first note that each peak marking is followed by another clear peak with an almost flipped topography. This secondary peak has a topography similar to the spike markings from the previous section. With the mc-tDCS, we intend to inhibit the epileptic activity at the earliest stage possible, maximally disrupting the synchronization of neurons. Therefore, we decided to

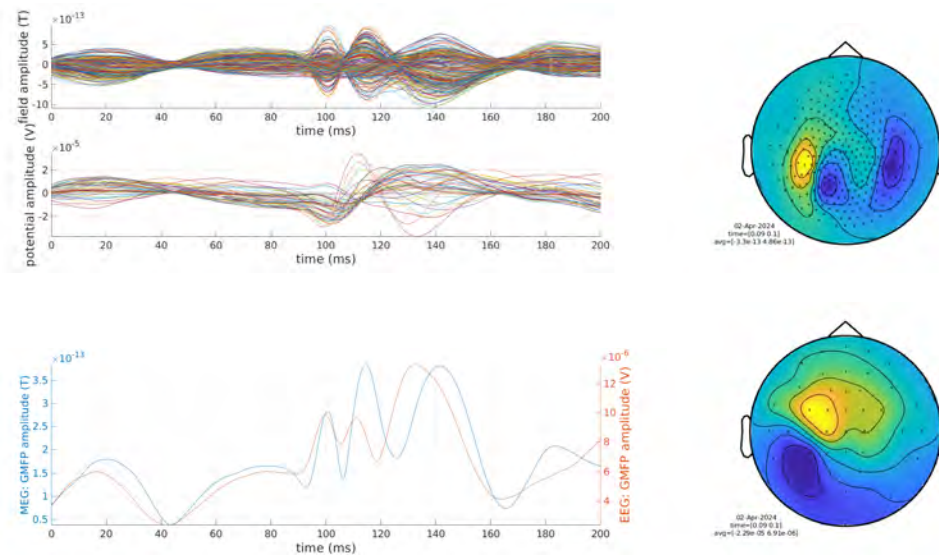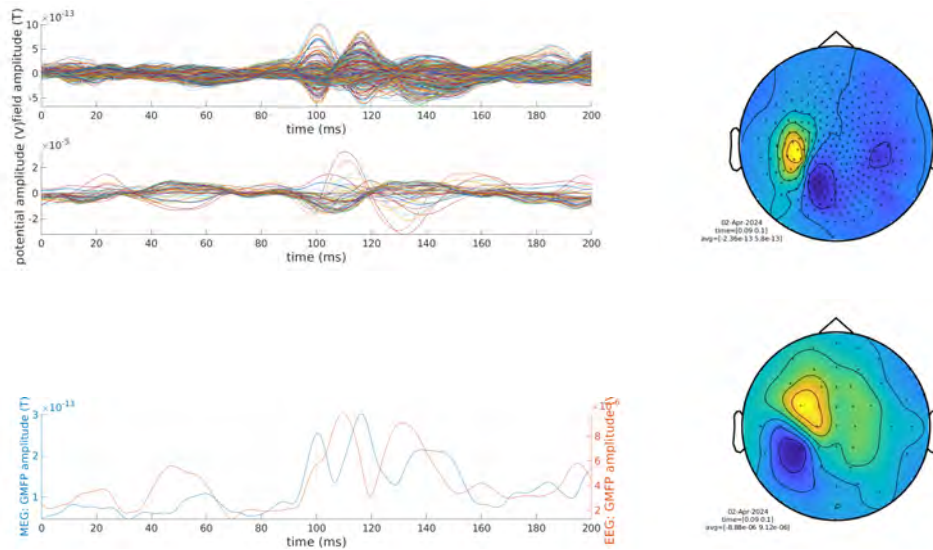FIGURE 9.2: EEG and MEG spike activity, averaged over the first 10 spikes only. Left panels: Butterfly plots and global mean field power (GMFP). Marked peaks are at 100 ms. Right panels: MEG (top) and EEG (bottom) topography averaged over the first half of the peak (90-100 ms)
.

select the onset of the first peak as a stimulation target, implying a possible excitation of the interictal activity.

Secondly, the topography of the first peak is not characterized by a single dipole alone, but we find additional contralateral activity in the right hemisphere as well. From the semiology, we can expect that the activity propagates into somatosensory areas during the later stages of the seizure. This could explain the contralateral activity even though the right arm and hand are affected by the seizure and not the left. We minimize the contributions of propagation to our data by only averaging the first 10 marked peaks, yielding the desired reduction in contralateral activity while maintaining a clearly dipolar peak topography (Figure 9.2.).

Volume conductor modeling

The volume conductor for P1 distinguishes five isotropic compartments (gray matter, cerebrospinal fluid, spongiosa, compacta, and scalp) plus anisotropic white matter. Gray and white matter segmentations are based on a T1-MRI image, the scalp on a T2, and the skull layers are created using a CT image. White matter anisotropy tensors are calculated from diffusion tensor imaging. For more information, see the previous section or Antonakakis et al., 2024a; Radecke et al., 2023. We use a geometry-adapted hexahedral mesh with a node-shift of 0.33 (Wolters, Grasedyck, and Hackbusch, 2004) and the standard continuous Galerkin finite element approach from the previous section. Note that we do not make use of CutFEM forward modeling as at the time there was no CutFEM implementation for MEG and the tDCS implementation was at an early stage. We employ the venant source model including mixed moments from Nüßing, 2018 on a 2 mm source grid containing 85540 nodes for both EEG and MEG forward calculations.
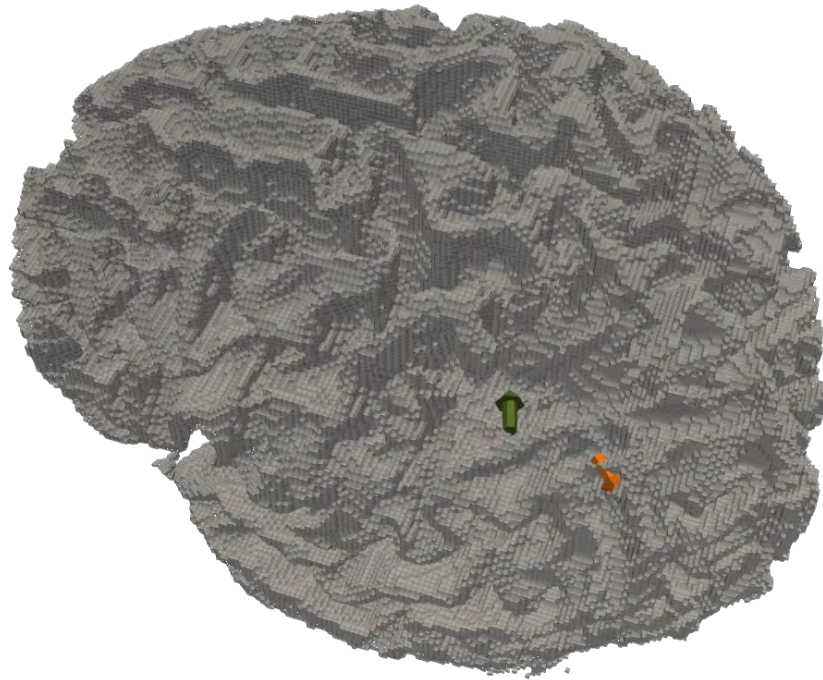
FIGURE 9.3: MEG-based source reconstructions of spike onset (green) and seizure onset (yellow). Visualized over white matter segmentation. The spike reconstruction points toward the resection.

Source reconstruction

Before performing source reconstruction, we have to decide whether to include the use of EEG data or not. In the previous chapter, we discussed the uncertainties connected to the patient's volume conductor model, from the cranial holes of unknown conductivity, a generally lower SNR and goodness of fit compared to MEG, deeper lying reconstruction results for the spikes, and high uncertainty in the calibrated skull conductivity. Additionally, the marked spikes have a primarily tangential orientation, motivating the use of MEG. Therefore, we decided against the use of EEG-based source reconstruction for this patient.

A single dipole deviation scan is performed to identify the origin of the onset of the first peak. As onset, we define the first sample whose data lead to a residual variance of less than 10 %, in this case, 4.2 ms before the spike peak. See Figure 9.3. for a comparison of seizure and spike onset (spike results from the previous chapter). The spike onset points to an area about 18 mm more occipitally and has an almost flipped orientation (151°).

tDCS stimulation and active sham caps

For our stimulation protocol, we require two caps: one for the actual stimulation, calculated based on the source reconstruction of the onset of the first seizure peak, and one for the active sham stimulation used to quantify possible placebo effects. The stimulation cap is based on the distributed constrained maximum intensity (D-CMI) approach (Khan et al., 2019).
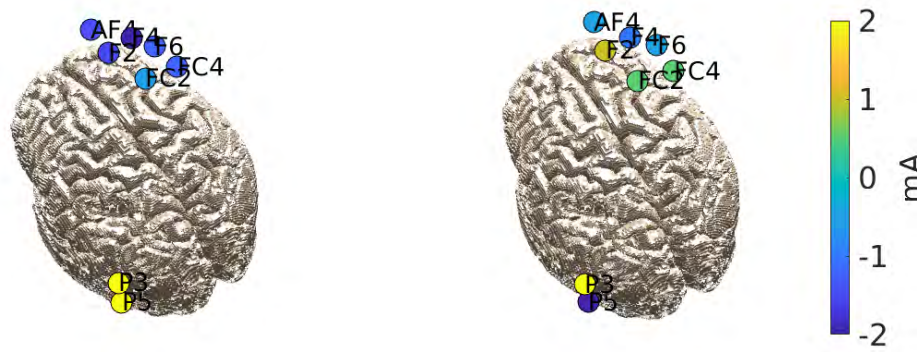
FIGURE 9.4: Optimized multi-channel tDCS and active sham caps. Circles indicate electrode positions, the labels are based on standard EEG-10-10 configuration. The color indicates stimulation strength (mA).

.

Electrode	mc-tDCS (mA)	active sham (mA)
P3	-2	2
P5	-2	-2
FC2	0.041	0.5
FC4	0.572	0.5
F2	0.822	1
F4	1.217	-1
F6	0.598	-0.5
AF4	0.75	-0.5

TABLE 9.1: Optimized multi-channel tDCS and active sham stimulation setup.

.

In essence, we have a set of predetermined electrode positions given by the holes in the stimulation cap, in our case 74 positions following the 10-10 system (Oostenveld and Praamstra, 2001). The D-CMI approach then finds a set of currents that maximizes the scalar product between the target vector and the current density vector induced by the stimulation electrodes. Note that in our case the target vector is the opposite of the reconstructed dipoles' orientation. The optimization is constrained by a 4 mA total current limit, maximally 2 mA per electrode, and a penalty term is added to ensure that the injected current is split over at least 8 electrodes, minimizing side effects. 8 is the maximum for our starstim (-)Neuroelectrics, Barcelona, Spain) tDCS device. For the active sham cap, we used the same 8 electrodes used for mc-tDCS. See Figure 9.4. and Table 9.1. for an overview of both stimulation setups. For brevity, we will refer to the D-CMI optimized mc-tDCS cap as mc-tDCS from here on.

The stimulation intensity in the target region is measured by two metrics: Intensity in target (IT), the Euclidean norm of the induced current density vector at the target location, and directionality (DIR), the scalar product of the current density vector and the normed target vector. The values for both stimulation types can be seen in Table 9.2., the induced current density in the target region due to either stimulation is visualized in Figure 9.5. The active sham reduces intensity in the seizure target by 76.8 %, and directionality by 88.2 % (84.5 % and 89.1 % if the reconstructed spike onset is selected as the
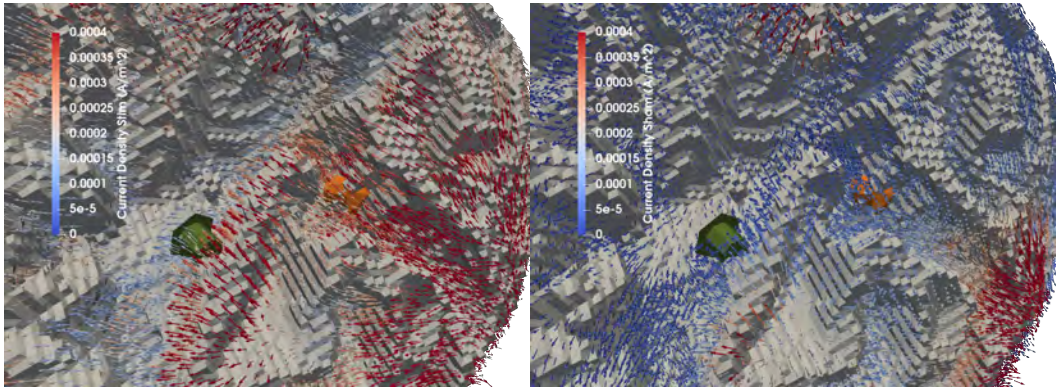
FIGURE 9.5: Cortical mc-tDCS (left) and active sham stimulation (right) current density vectors (A/m^2). Targets are green (spike onset) and orange (seizure onset).

.

		active sham	mc-tDCS
Spike	DIR	0.0184	0.1691
	IT	0.0486	0.3138
Seizure	DIR	0.0304	0.2576
	IT	0.1061	0.4575

TABLE 9.2: Stimulation metrics for mc-tDCS and active sham stimulation (A/m^2). Directionality (DIR) states the scalar product of induced current density and target vector, IT refers to the 2-norm of the induced vector. Quantified for targets reconstructed based on either the spike or seizure onset.

.

target).

Stimulation protocol

As mentioned, our study follows the general stimulation protocol described in Antonakakis et al., 2024a: 2 weeks (Monday-Friday) tDCS stimulation, one of which is active sham. The active sham condition took place in September 2022, and the actual stimulation in December 2022, ensuring a wash-out period of more than 6 weeks to minimize carry-over effects (Woods et al., 2016). Each day's stimulation protocol started with a one-hour EEG session between 9 and 10 am, 2 times 20 min tDCS stimulation intercepted by a 20 min break, concluded by another hour of EEG, yielding a total of 20 one-hour blocks of EEG data.

EEG was recorded using a 19-electrode Waveguard cap (Ant Neuro, Hengelo, Netherlands). During the stimulation weeks, the patient was admitted to the University Hospital Bochum. He spent both the EEG recording and tDCS stimulation sessions reading or using electronic devices. Neither the patient nor the medical technical assistants who attended to him and who handled the stimulation device could distinguish the two stimulation conditions and were therefore blinded. The stimulation time took place at roughly the same time each day to minimize the influence circadian rhythms have on the number of (inter-)ictal epileptic discharges (Kaufmann et al., 2021). A stimulation protocol of 2 times 20 min stimulation with a 20-minute break has

been shown to outperform single 20 min stimulation protocols (Yang, Shin, and Hong, 2021).

After the two stimulation weeks, any meta data such as the stimulation date was removed from the 20 recordings before shuffling them and giving them to 3 independent epileptologists who marked ictal and interictal epileptiform discharges. The epileptologists had one meeting on how to mark the data and decided on distinguishing spikes, polyspikes, and seizure activity. For spikes, they marked the peak, for polyspikes - 3 or more spikes in rapid succession - the beginning, and for seizures both beginning and end. See Figure 9.6. for a comparison of the three events. Adding polyspikes as a metric may seem controversial, as the decision when to mark something as a single polyspike or several separate spikes is highly subjective, in particular as the patient has a very high number of IEDs. However, it significantly decreased the workload for the marking epileptologists and since we have 3 independent sets of markings, we already take great care to minimize random effects from inconsistent markings.

Evaluation metrics

A 2021 meta-study (Sudbrack-Oliveira et al., 2021) found 9 original sham-controlled studies that investigated the effects of tDCS stimulation on epilepsy. While both the type of epilepsy and electrode placement varied, they all quantified either the number of IEDs, seizures, or both.

Our patient also gives us the rare opportunity to analyze the seizure intensity and duration from the EEG data. The duration is defined as the time in seconds between start and stop marking, as intensity we look at the average global mean field power during that timeframe.

Regarding spikes, we can additionally quantify the peak strength and whether it changes its topography from before to after the stimulation. Peak strength is defined as the global mean field power (GMFP) at the point of the peak, topography changes are measured as relative difference measure (RDM) between the average peak topography before and after the stimulation.

Statistical analysis of the tDCS intervention effect has to take into consideration as many confounding parameters as possible. We eliminated as many of these factors as possible, from adding a sham condition to quantify placebo effects, blinding the patient, medical technical assistants, and the marking epileptologists as well as maintaining similar stimulation times every day and adding a 6-week wash-out period between conditions, yet several remain: Variance in epileptic activity may be affected by the ultradian rhythms (Spencer et al., 2016) and who of the 3 epileptologists performed the marking. Therefore, we perform a mixed-effects analysis of variance (ANOVA), where the outcome, i.e. the number of marked events in a single 1-hour EEG dataset, depends on the main effects pre-/post-stimulation, whether it was an active sham or a stimulation week, the day in the week. Our tDCS intervention effect is then given as the interaction effect between pre-/post-stimulation and week. Note that given our limited sample size (20), setting up the ANOVA with this many parameters strongly reduces the number of degrees of freedom for each condition.

Seizure count:	Sham Pre	Sham Post	Stim Pre	Stim Post
Epil. 1	6	4	10	5
Epil. 2	6	4	10	5
Epil. 3	7	4	9	5
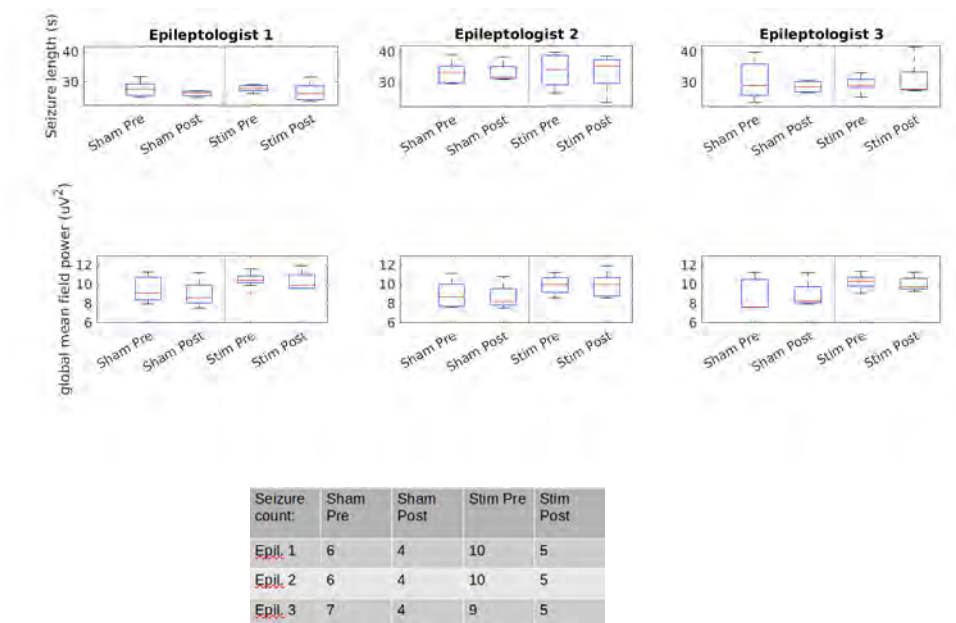
FIGURE 9.6: Seizure lengths (top) and global mean field power (GMFP, bottom) during the 4 different conditions: Before and after active sham stimulation, before and after mc-tDCS. One graph per epileptologist who performed the marking
.

9.2   Stimulation outcome

Seizures

First, we look at seizure-based metrics, see Figure 9.6. As the total number of seizures is low, we only compare them on a week-to-week basis. All epileptologists marked a total of 25 seizures, two of them agreed on the markings, while the third marked an additional seizure in the EEG data before the sham condition and one less before the stimulation condition. Both stimulation conditions resulted in reductions, 33 % in the active sham week, and 50 % in the mc-tDCS week. We found two significant main effects: pre-/post-stimulation ($F(1,50) = 15.57$), $p < 0.001$, $\eta^2 = 0.24$) and active sham/stimulation week ($F(1,50) = 5.968$), $p = 0.018$, $\eta^2 = 0.11$). In other words, whether an EEG was measured before or after the (sham-)stimulation and whether it was measured in the first or second week both have a statistically significant impact, but the interaction of the two does not. The weekday, or which epileptologists performed the marking are also no significant factors. From Figure 9.6., we see that there is no clear effect on either the length of seizures or the GMFP. The average seizure duration is 30.20 seconds with an average GMFP of 14.07 μV.

Spikes

Compared to the seizure markings, where coherence over expert markings was high, we see in Figure 9.7. that the same is not the case for interictal activity. Epileptologist 1 marked 5060 events, 3593 of which are polyspikes, expert 2 marked 10080 with 2490 polyspikes, and the third marked 2256 of 5090 total IEDs as polyspikes. Marker 2 was more likely to mark an event

as multiple single spikes rather than one polyspike. The similarity in total marked events between experts 1 and 3 does not mean that they marked the same events. If expert 1 marked an event as a spike, only in 49 % of cases did expert 3 also place a marker within a timeframe of 40 ms.

Additionally, there is a high variance in the total IED number depending on the day and week. Each expert has marked at least 108, 297, and 133 total IEDs per day and a maximum of 1653, 1825, and 1172 respectively.

Still, we observe several trends. The overall number of spikes and polyspikes increases after (sham-)stimulation, in the mc-tDCS week between 22 % and 136 %, in the active sham week between 0 % and 38 %, depending on the expert who performed the marking. There is also a higher variance in peak topographies in the sham week, as measured by the RDM. We observe no trends in peak strength. The variance due to epileptologist, day, and week seems to dominate the mc-tDCS-based effects in this patient.

Interaction between spikes and seizures

We found a slight increase in spikes after stimulation and a slight decrease in seizure number, indicating that the two are inversely correlated. We test this by performing another ANOVA, this time quantifying the impact of epileptologist, number of spikes/polyspikes, week, and day onto the number of spikes. Neither day of the week nor number of spikes alone is a significant predictor for seizure count, yet the interaction between them is $(F_{(4,29)} = 7.02)$, $p < 0.001$, $\eta^2 = 0.49$. No other significant effects were found.

9.3 Discussion

We stimulated an epileptic patient for two weeks, one week of multi-channel optimized transcranial direct current stimulation (mc-tDCS), and one week of active sham stimulation. The optimization was performed using the distributed constrained maximum intensity stimulation approach (D-CMI, Khan et al., 2019). The stimulation target was selected based on the source reconstruction of Magnetoencephalography (MEG) data. MEG data was marked by an epileptologist who found both ictal and interictal epileptic activity, allowing us to base the stimulation on the ictal activity. Ictal activity was associated with an inverse topography compared to interictal discharges, leading to the assumption that the stimulation would have opposite effects on seizure and spike activity.

The stimulation of P1 is the second entry in what is supposed to become a group study targeted at investigating the effects of tDCS on epileptic activity. Therefore, the stimulation protocol that the patient underwent is not sufficient to create statistically significant results for every single subject but is designed for a larger group of patients.

During the mc-tDCS week, we observed a 50 % decrease in seizure activity, compared to 33 % in the sham week. Post-stimulation spike numbers increased in both weeks, more strongly so in the mc-tDCS week. These results align with our initial hypothesis of inhibiting seizures and exciting spikes. To explain our results, we look at the zone concept discussed in Rosenow

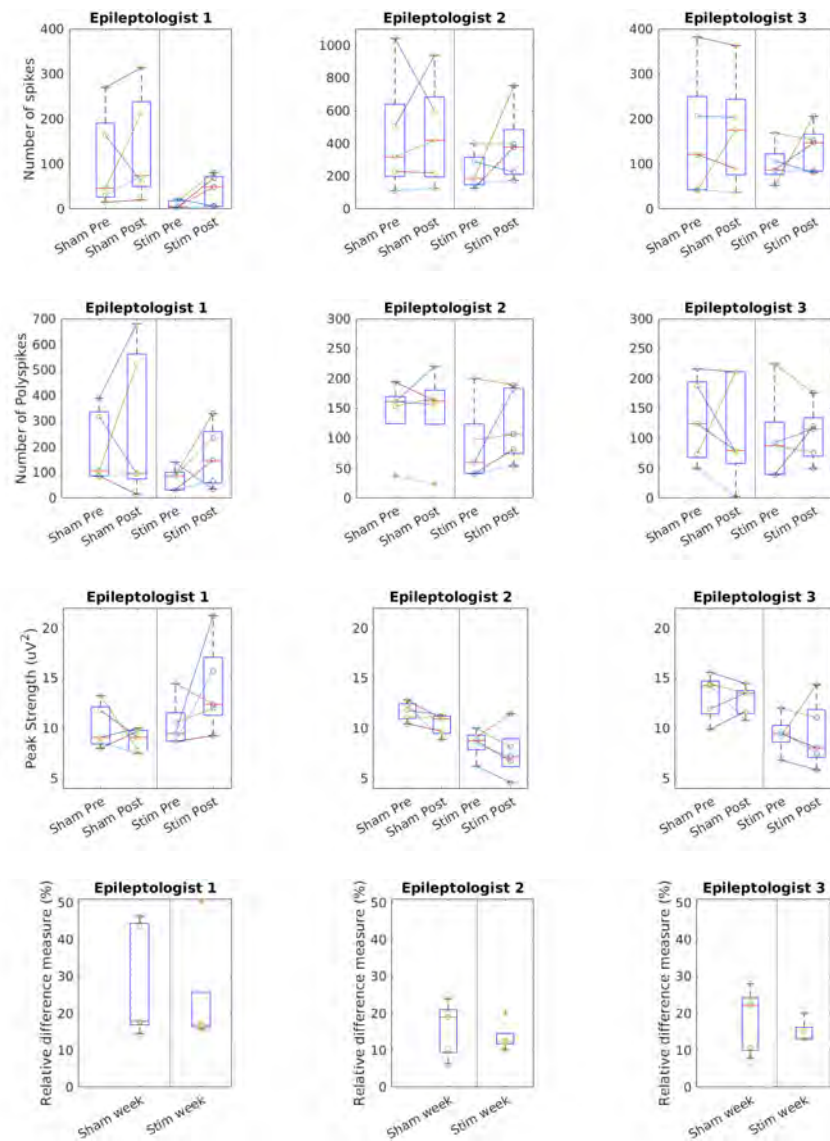FIGURE 9.7: Number of spikes (top), polyspikes(2nd row), spike peak strength(GMFP, 3rd row), and relative difference measure (RDM, bottom) during the 4 different conditions (2 for RDM): Before and after active sham stimulation, before and after mc-tDCS. One graph per epileptologist who performed the marking. RDM is calculated based on average peak topographies before and after each (sham-)stimulation day.

.

and Lüders, 2001. In essence, there are 5 zones of interest for our analysis. The symptomatogenic zone is activated during seizures and produces the tingling and visual aura reported by the patient. The irritative zone produces interictal spikes, the epileptogenic zone contains both the area that produces the clinical seizures (the seizure onset zone) and an area that potentially could produce seizures, if the seizure onset zone is removed. The latter is the case in our patient, who had parts of his cortex surgically removed. The definition of the epileptogenic lesion, or focal cortical dysplasia (FCD) in this case, is usually based on MR imaging and therefore limited by the quality of the imaging. If it is epileptogenic, it has a strong overlap with the epileptogenic zone, but one does not necessarily contain the entirety of the other (Rosenow and Lüders, 2001).

Important is the distinction between the irritative zone and the seizure onset zone. As we see from our source reconstruction, seizure and spike localize to proximate, but distinct locations in the cortex, giving us evidence that they originate from different regions that are possibly connected by the post-surgery remnants of the FCD. We have further seen that an increase in spike activity is connected to a significant decrease in seizure numbers. This decrease corresponds to the concepts described in Avoli, Curtis, and Köhling, 2013; Chang et al., 2018, who discuss the existence of good and bad spikes that either prevent or facilitate ictal activity. These theories however operate on a cellular or even molecular basis, with unclear implications for the surface EEG/MEG that we can measure. For future mc-tDCS candidates, where we do not have high-quality seizure data, there is therefore no strong argument for when to excite spikes rather than inhibit them. At least, no argument that goes beyond quantifying both events.

Both stimulation weeks are associated with a significant reduction in seizures after the stimulation. There may be a variety of reasons for this. First, the patient's stress level may have changed throughout the stimulation, possibly due to an increasing discomfort associated with wearing EEG/stimulation caps, starting to work, or the general noise level in the hospital. However, he did not indicate such on his daily questionnaires and his attending epileptologists also find such a scenario implausible. Secondly, a decrease in seizure activity may be part of his circadian rhythm (Kaufmann et al., 2021; Spencer et al., 2016).

There is however a third possibility. The active sham still induced a current about 1/4 as strong as the mc-tDCS. Given how the uncertainties in the volume conductor model due to the cranial holes translate to uncertainties in the reconstructed orientations and locations it may well be that the active sham stimulation also had an inhibitory effect on the seizures. Additionally, the patient suffers from a type 2b FCD, where the cortex loses most of its lamination and where balloon cells without apical dendrites are present. How these neurons, which do not produce extracranial electromagnetic fields, react to electric stimulation is also unclear. Possibly a sufficiently strong current interferes with the activity of these neurons to disrupt their epileptogenic process. An additional argument for the active sham explanation is the lower increase in spike numbers, less than 40 % compared to up to 136 %. Our simulation shows that for active sham, the intensity in the spike target is 54 % lower than in the seizure target region, possibly leading to a less substantial effect on the spikes.

TDCS may add to the treatment of epilepsy in several ways: Epilepsy is a condition where treatment options such as medication or seizure are highly invasive. While medication is often effective at first, between 20-40 % of patients will develop refractory epilepsy, where the medication loses its effectiveness. TDCS may offer an alternative for these patients.

Regarding surgical excision, the epileptogenic zone may be larger than the seizure onset, thus even after surgical intervention, epilepsy patients with FCD are often not entirely seizure-free (59 % reached Engel class 1A in Veersema et al., 2019). Here, long-term tDCS may be used to delay or inhibit the long-term formation of new epileptogenic neuron clusters at the expense of minimal side effects.

Aside from its promise as a new treatment, a successful tDCS stimulation that has a measurable impact on ictal or interictal activity provides additional diagnostic value, linking the stimulated brain region directly to the patient's epilepsy and strengthening the diagnosis on the way to surgical resection.

The requirements for an optimized mc-tDCS treatment as we investigated here are high. There is no guarantee that the subject's EEG/MEG shows ictal or even interictal activity, with 25 % of refractory epilepsy patients not showing either MEG or EEG spikes in Knake et al., 2006. Even given spikes of sufficient frequency and signal-to-noise ratio, a multi-focal source reconstruction or a target lying in a deep brain structure may limit the value of tDCS as a treatment option.

9.3.1   Outlook for the patient

The trends observed from the transcranial direct current stimulation of patient 1 indicate that the patient may profit from a stimulation over an extended period of time. Such a stimulation could be performed in several different ways, each posing distinct practical challenges. Performing the stimulation at the hospital clinic would ensure an accurate application of the stimulation. It would however bind more of the already limited spatial and personal hospital capacities and force the patient to visit the clinic on a regular basis. Home stimulation performed by the patient himself is comparatively cheap. The patient however has to be reliable both in his ability to perform the stimulation unsupervised and in not overdosing or in other ways abusing the device (Charvet et al., 2020).

A third option is the implantation of a subdural stimulation device. The device would perform the stimulation independently from the patient based on a protocol determined by his attending epileptologist, offsetting both cost and reliability concerns raised by clinical/home stimulation. The downside is the limited number of feasible electrode patterns and the invasive surgery. At the time of writing this thesis, the epileptologists treating patient 1 were in the process of considering the implantation of an EASEE (Precisis GmbH, Heidelberg, Germany) device. Several long-term studies investigating the effect of EASEE devices are currently in the making, see `https://easee.precisis.de/en/health-care-professionals/studies/`.

Chapter 10

Summary and Outlook

Summary

In this thesis, we presented a cut finite element method (CutFEM) and applied it to forward modeling for Electro- and Magnetoencephalography (EEG/MEG) as well as transcranial direct current stimulation (tDCS). After introducing the neural sources inside the brain and how to stimulate them transcranially, we show how to derive the forward problems for EEG/MEG/tDCS from the Maxwell equations. We then briefly describe solving the EEG forward problem in three-compartment scenarios using the boundary element method (BEM). In chapter two, we then describe how to solve the forward problems using the finite element method (FEM) in more complicated scenarios. FEM heavily relies on accurate meshing, the facilitation of which is the central motivation for the CutFEM described in chapter three. CutFEM relies on a fundamental mesh for its trial functions, intersected by level-set functions representing tissue boundaries. Before moving towards simulation results, chapter four describes how to create the level set functions needed for CutFEM based on segmentation results. This chapter also focuses on creating realistic six-compartment hexahedral meshes and three-compartment surface triangulations. These are used for the computation of FEM and BEM forward solutions that are compared against CutFEM in later chapters.

Chapter 5 consists of sphere model scenarios, where CutFEM outperforms both competing tetrahedral FEM approaches and an unfitted discontinuous Galerkin approach when compared against (quasi-)analytical reference solutions. The first realistic data sets are analyzed in Chapter 6, where we present the results of an $n = 19$ group study of somatosensory evoked potentials and fields. We found that CutFEM shows promise in several categories when compared against results from six-compartment hexahedral FEM and three-compartment BEM approaches. Among these is proximity to an atlas-based estimation of Brodmann area 3b, residual variance, source separability, and sensitivity to quasi-radial contributions.

The final two main chapters of the thesis are concerned with the analysis of two epilepsy patients and the subsequent tDCS stimulation of one of them. Both patients differ in the origin of their affliction and also pose several challenges for head modeling since one of them had previous resective surgery and the other has a large porencephalic cyst. Comparing source reconstructions based on three- and six-compartment forward models showed more pronounced differences than in the group study investigations in healthy subjects.

The outcome of the multi-channel optimized tDCS stimulation performed on the patient who has already had surgery shows a trend in seizure reduction. The second patient also agreed to participate in a tDCS stimulation.

Outlook

In this thesis, we examined CutFEM's performance in applications in neural bioelectromagnetism. We showed that CutFEM yields competitive results in spherical and realistic head model scenarios. One caveat is the computation time CutFEM requires in MEG due to a slow convergence of the iterative solver. The convergence can be sped up by applying an overlapping Schwarz smoother before the algebraic multigrid (AMG) solver. This reduces the number of iterations but does not significantly decrease the total computation time for the transfer matrices due to longer computation times per iteration. A separate AMG preconditioning on each tissue interface may yield a better balance of convergence speed and time per iteration.

The investigation of second-order trial functions combined with the partial integration source model has shown promise in purely spherical scenarios and holds promise for realistic head models. Integrating the local subtraction source model may benefit the overall accuracy of CutFEM independent of the number of trial functions.

The greater sensitivity to quasi-radial sources in MEG and the better source separability we found in CutFEM should be investigated in datasets with an ambiguous source orientation or where there is a higher number of simultaneously active sources. Also, further investigations could show whether the increased quasi-radial sensitivity is particularly important when the MEG sensor is not oriented radially towards the head. Sensors that can measure tangential and quasi-radial fluxes at the same location are possible with the upcoming optically pumped magnetometers. Their introduction may result in an increased demand for more realistic head modeling.

Concerning tDCS, it may be promising to investigate whether the use of CutFEM yields a change in the sensitivity profile of the cortex.

As DUNEuro is already part of toolboxes such as Brainstorm and Fieldtrip, future updates to these toolboxes should include CutFEM forward models as well, reducing hurdles in the use of complex forward models for clinical applications and increasing the visibility of the impact forward modeling has on source localization and transcranial electric stimulation.

Appendix A

Numerical solvers for CutFEM

The computationally most expensive part of FEM-based solving the EEG/MEG/tDCS forward problem is setting up and solving the tDCS/transfer matrix problems $Au = b$, where b is either the EEG or MEG transfer matrix right-hand side, see Chapter 3. As the FEM models we employ typically consist of millions of degrees of freedom, the system is not solved directly, but via an iterative solver. The time it takes to solve this equation system depends on multiple factors, among these the condition number of the matrix A, the iterative numerical solver used, and the desired reduction

$$||Ax - b||$$

in some solver-dependent metric.

As indicated in Chapter 4, a central motivation for the ghost penalty is its impact on the conditioning of A. In Burman, 2010, it was shown for triangular meshes that using the ghost penalty renders the conditioning of A independent of the way the level set functions intersect the mesh.

Currently, the iterative solver used for CutFEM is an algebraic multigrid solver (AMG). Multigrid methods create a grid hierarchy of several levels over the stiffness matrix. The levels are connected by prolongation/restriction matrices, the weights of which depend on the type of multigrid method used. In each iteration, the solver steps from level to level, applying a smoother in-between. On the coarsest level, the system is solved directly and the solution is updated.

The weights connecting the levels can be chosen based on the spatial location and geometric information about the trial function associated with the respective stiffness matrix entry, resulting in a geometric multigrid approach. The downside is that the choice of weights along the coarser levels is not straightforward, particularly in unstructured meshes.

Algebraic multigrid methods create the coarsening weights based primarily on information contained in the stiffness matrix. Since Wolters et al., 2002, the AMG has been used to solve the EEG forward problems, the version implemented in DUNEuro is based on Blatt, 2010. Weights are chosen primarily based on the coupling of two matrix entries $a_{i,j}, a_{j,i}$.

For the EEG, a reduction of residual l_2-norm by a factor of 1e-8 results in relative difference measure and magnitude errors below 0.1%. For the MEG, we need a reduction of 1e-11 to achieve similar values. This may be due to the increased distance between sensors and source, and the lower sensitivity to quasi-radial contributions.

To investigate the performance of the ghost penalty and the AMG, we create a set of 4 mm 4-layer sphere models. The models are identical to those

Min. CSF thickness (mm)	2	1.5	1	0.5	0
Condition Nr (in billions)	6.44	7.01	6.51	6.57	6.50
Nr. Iterations	70	71	74	84	159

TABLE A.1: Matrix condition and pure AMG solver iterations until a reduction of 1e-11 is achieved for shifted spheres.

used in Chapter 6, but the innermost sphere (brain) is iteratively shifted to the right, until it touches the skull sphere, resulting in a hole in the CSF. We then calculate the condition number of the resulting CutFEM stiffness matrix and track the number of iterations required to reach a reduction of 1e-11. All CutFEM-related parameters are identical to the ones chosen in Chapter 6. The iterations are averaged over 20 electrodes and rounded to the next digit.

The results can be found in Table B.1. We note the condition number is independent of the position of the spherical gray matter level set. However, the number of iterations increases with decreasing minimal CSF thickness, more than doubling from 70 to 159 iterations. For reference, a 1 mm geometry-adapted hexahedral mesh with 3 million nodes requires less than 30 iterations for the same reduction.

This behavior indicates that choosing a different solver setup rather may be more important than increasing the ghost penalty, in particular as an increased ghost penalty results in higher numerical errors Erik Burman and Peter Hansbo, 2012.

In Gross and Reusken, 2023, a sub-space splitting process is recommended, one subspace is the continuous Galerkin space on the fundamental mesh, and the other is the space of all cut basis functions. Preconditioners with bounded condition number are then derived, and a symmetric Gauss-Seidel method is suggested. Note that the assumption for these preconditioners is a much smaller dimensionality of the space with the cut basis functions, i.e. only a few fundamental cells are assumed to be intersected by the level sets. In our application, with six or more compartments which are often only a few millimeters thick, this assumption does not hold.

In discontinuous Galerkin (DG) and unfitted discontinuous Galerkin (UDG), the addition of a first coarsening step has shown promise Blatt, 2010; Nüßing, 2018. Note that the DG-space V^{DG} contains the CG-space V^{CG}. The first coarsening step reduces the stiffness matrix to the CG space, where the AMG is applied. For UDG, the reduction is from the UDG space to the Cut-FEM space. On the fine (U)DG-space, a multiplicative overlapping Schwarz smoother is applied Bastian et al., 2008. In the DG case, the overlapping patches are based on the vertices, with one patch per vertex. Each patch consists of the trial functions in the mesh elements surrounding the vertex. For UDG, the patches are created based on the faces of fundamental cells cut by level sets. For each face, all trial functions acting on the two cut cells neighboring the face are aggregated. In UDG, this has the added benefit of smoothing over the contributions of small cut cells in the absence of a ghost penalty term.

Combining the subspace splitting from Gross and Reusken, 2023 with the overlapping Schwarz smoother from Nüßing, 2018, we obtain the following method.

Starting from the full CutFEM space, the first restriction matrix aggregates

all trial functions associated with the same vertex in the fundamental mesh, effectively clearing up the overlap of trial functions. On this coarse space, we then apply the standard AMG. On the fine level, an overlapping Schwarz smoother is applied. The patches are created in the same manner as in the UDG case.

For the test model from before, we end up with an average of 16 iterations for 2 mm minimal CSF thickness and 17 iterations for a minimal thickness of 0 mm, effectively cutting the number of iterations by 89%.

However, the time per iteration is 34.89 seconds when using the Schwarz Smoother, compared to 0.95 when using the AMG alone. The total computation time therefore increases by a factor of 3.7 when using the Schwarz smoother rather than the AMG alone.

Calculations were performed without parallelization on an Intel Core i7-6700 with 3.4 GHz, 8 cores, and 32 GB RAM.

A future study could investigate using a more efficient smoother on the fine mesh. A separate AMG-based preconditioner for each level set may be effective at smoothing over the interfaces at a more reasonable time per iteration. Alternatively, the use of fewer, larger patches could be investigated for the overlapping Schwarz method.

Appendix B

Software tools

For the creation of this thesis, several software toolboxes were used. Many of them are part of an automated pipeline to create six-compartment geometry-adapted hexahedral head models and lead field matrices for EEG/MEG as well as the tDCS optimization matrices. The pipeline including documentation can be found on Zenodo `https://zenodo.org/doi/10.5281/zenodo.11066431`.

Fieldtrip
EEG/MEG data preprocessing, interfaces to SPM12, Openmeeg, calculating EEG analytical solutions, see `https://www.fieldtriptoolbox.org/`

Gmsh
Tetrahedral mesh generation, see `https://www.gmsh.de/`

FSL
MRI registration, MRI visualization, see `https://fsl.fmrib.ox.ac.uk/fsl/docs/#/`

SPM12
Skull segmentation, see `https://www.fil.ion.ucl.ac.uk/spm/software/spm12/`

CAT12
Creation of tissue probability maps, see `https://neuro-jena.github.io/cat12-help/`

ITK
Anti-aliasing of binary segmentations, see `https://itk.org/`

Brainstorm
Sensor registration onto the scalp surface, see `https://neuroimage.usc.edu/brainstorm/`

Paraview
Visualization, see `https://www.paraview.org/`

VGrid
Creation of geometry-adapted hexahedral meshes, see `http://vgrid.simbio.de/`

SimBioInterface
Source space generation, see `https://www.mrt.uni-jena.de/simbio/index.php?title=Main_Page`

SDFGen
Turning surface triangulations into signed distance functions, see `https://github.com/christopherbatty/SDFGen`

Openmeeg
Three-compartment Boundary element method lead field calculations, see `https://openmeeg.github.io/`

DUNEuro

Finite element-based lead field generation, see `https://www.medizin.uni-muenster.de/duneuro/startseite.html`. DUNEuro is based on the DUNE toolbox.

DUNE

Modular numerics toolbox for solving partial differential equations, see `https://dune-project.org/`

Matlab

General scripting, data processing, see `https://de.mathworks.com/products/matlab.html`

Latex

Thesis typesetting, see `https://www.latex-project.org/`

Bibliography

Acar, Zeynep Akalin, Can E. Acar, and Scott Makeig (2016). "Simultaneous head tissue conductivity and EEG source location estimation". In: *NeuroImage* 124, pp. 168–180. ISSN: 1053-8119.

Ahlfors, Seppo P. et al. (2010). "Sensitivity of MEG and EEG to source orientation". In: *Brain topography* 23, pp. 227–232.

Akhtari, M. et al. (2002). "Conductivities of three-layer live human skull". In: *Brain topography* 14.3, pp. 151–167. DOI: 10.1023/a:1014590923185.

Akkus, Zeynettin et al. (2017). "Deep Learning for Brain MRI Segmentation: State of the Art and Future Directions". In: *Journal of digital imaging* 30.4, pp. 449–459. DOI: 10.1007/s10278-017-9983-4.

Allison, Truett et al. (1991). "Cortical somatosensory evoked potentials. II. Effects of excision of somatosensory or motor cortex in humans and monkeys". In: *Journal of neurophysiology* 66.1, pp. 64–82. ISSN: 0022-3077.

Antonakakis, Marios et al. (2019). "The effect of stimulation type, head modeling, and combined EEG and MEG on the source reconstruction of the somatosensory P20/N20 component". In: *Human brain mapping* 40.17, pp. 5011–5028.

Antonakakis, Marios et al. (2020a). "Inter-subject variability of skull conductivity and thickness in calibrated realistic head models". In: *NeuroImage* 223, p. 117353. ISSN: 1053-8119.

Antonakakis, Marios et al. (2020b). "Inter-subject variability of skull conductivity and thickness in calibrated realistic head models". In: *NeuroImage* 223, p. 117353. ISSN: 1053-8119.

Antonakakis, Marios et al. (2024a). "Targeted and optimized multi-channel transcranial direct current stimulation for focal epilepsy: An N-of-1 trial". In: *Brain stimulation* 17.2, pp. 221–223. ISSN: 1935-861X. DOI: 10.1016/j.brs.2024.02.010.

— (2024b). "Targeted and optimized multi-channel transcranial direct current stimulation for focal epilepsy: An N-of-1 trial". In: *Brain stimulation* 17.2, pp. 221–223. ISSN: 1935-861X. DOI: 10.1016/j.brs.2024.02.010.

Ashburner, John and Karl J. Friston (2005). "Unified segmentation". In: *NeuroImage* 26.3, pp. 839–851. ISSN: 1053-8119. DOI: 10.1016/j.neuroimage.2005.02.018.

Ashburner, John et al. (2014). "SPM12 manual". In: *Wellcome Trust Centre for Neuroimaging, London, UK* 2464, p. 4.

Aurlien, H. et al. (2004). "EEG background activity described by a large computerized database". In: *Clinical Neurophysiology* 115.3, pp. 665–673. ISSN: 1388-2457.

Avoli, Massimo, Marco de Curtis, and Rüdiger Köhling (2013). "Does interictal synchronization influence ictogenesis?" In: *Neuropharmacology* 69, pp. 37–44. DOI: 10.1016/j.neuropharm.2012.06.044.

Aydin, Ümit et al. (2014). "Combining EEG and MEG for the reconstruction of epileptic activity using a calibrated realistic volume conductor model". In: *PloS one* 9.3, e93154. DOI: 10.1371/journal.pone.0093154.

Badia, Santiago, Francesc Verdugo, and Alberto F. Martín (2017). "The aggregated unfitted finite element method for elliptic problems". In: DOI: 10.48550/ARXIV.1709.09122.

Bastian, P. et al. (2008). "A generic grid interface for parallel and adaptive scientific computing. Part I: abstract framework". In: *Computing* 82.2-3, pp. 103–119. ISSN: 0010-485X. DOI: 10.1007/s00607-008-0003-x.

Batsikadze, Giorgi et al. (2013). "Partially non–linear stimulation intensity–dependent effects of direct current stimulation on motor cortex excitability in humans". In: *The Journal of physiology* 591.7, pp. 1987–2000.

Baysal, Uğur and Jens Haueisen (2004). "Use of a priori information in estimating tissue resistivities—application to human data in vivo". In: *Physiological measurement* 25.3, p. 737. ISSN: 0967-3334.

Beleza, Pedro (2009). "Refractory epilepsy: a clinically oriented review". In: *European neurology* 62.2, pp. 65–71. ISSN: 0014-3022.

Beltrachini, L. (2019). "A Finite Element Solution of the Forward Problem in EEG for Multipolar Sources". In: *IEEE transactions on neural systems and rehabilitation engineering : a publication of the IEEE Engineering in Medicine and Biology Society* 27.3, pp. 368–377. DOI: 10.1109/TNSRE.2018.2886638.

Beumer, Steven et al. (2022). "Personalized tDCS for Focal Epilepsy—A Narrative Review: A Data-Driven Workflow Based on Imaging and EEG Data". In: *Brain Sciences* 12.5. DOI: 10.3390/brainsci12050610.

Blatt, Markus (2010). "A Parallel Algebraic Multigrid Method for Elliptic Problems with Highly Discontinuous Coefficients". PhD thesis. Heidelberg University Library. DOI: 10.11588/heidok.00010856.

Boto, Elena et al. (2017). "A new generation of magnetoencephalography: Room temperature measurements using optically-pumped magnetometers". In: *NeuroImage* 149, pp. 404–414. ISSN: 1053-8119. DOI: 10.1016/j.neuroimage.2017.01.034.

Braess, Dietrich (2007). *Finite Elemente: Theorie, schnelle Löser und Anwendungen in der Elastizitätstheorie*. Springer-Verlag. ISBN: 3642347975.

Brant-Zawadzki, M., G. D. Gillan, and W. R. Nitz (1992). "MP RAGE: a three-dimensional, T1-weighted, gradient-echo sequence–initial experience in the brain". In: *Radiology* 182.3, pp. 769–775. ISSN: 0033-8419. DOI: 10.1148/radiology.182.3.1535892.

Brookes, Matthew J. et al. (2021). "Theoretical advantages of a triaxial optically pumped magnetometer magnetoencephalography system". In: *NeuroImage* 236, p. 118025. ISSN: 1053-8119. DOI: 10.1016/j.neuroimage.2021.118025. URL: https://www.sciencedirect.com/science/article/pii/S1053811921003025.

Buchner, H. et al. (1995). "Somatotopy of human hand somatosensory cortex revealed by dipole source analysis of early somatosensory evoked potentials and 3D-NMR tomography". In: *Electroencephalography and clinical Neurophysiology* 96.2, pp. 121–134. DOI: 10.1016/0168-5597(94)00228-7.

Buchner, Helmut et al. (1997). "Inverse localization of electric dipole current sources in finite element models of the human head". In: *Electroencephalography and clinical Neurophysiology* 102.4, pp. 267–278.

Burman, Erik (2010). "Ghost penalty". In: *Comptes Rendus Mathematique* 348.21-22, pp. 1217–1220.

Burman, Erik et al. (2015). "CutFEM: discretizing geometry and partial differential equations". In: *International journal for numerical methods in engineering* 104.7, pp. 472–501.

Buschermöhle, Yvonne et al. (2024). "Comparing the performance of beamformer algorithms in estimating orientations of neural sources". In: *iScience* 27.3, p. 109150. ISSN: 2589-0042. DOI: 10.1016/j.isci.2024.109150.

Chang, Wei-Chih et al. (2018). "Loss of neuronal network resilience precedes seizures and determines the ictogenic nature of interictal synaptic perturbations". In: *Nature neuroscience* 21.12, pp. 1742–1752. DOI: 10.1038/s41593-018-0278-y.

Charvet, Leigh E. et al. (2020). "Supervised transcranial direct current stimulation (tDCS) at home: A guide for clinical research and practice". In: *Brain stimulation* 13.3, pp. 686–693. ISSN: 1935-861X. DOI: 10.1016/j.brs.2020.02.011.

Chuang, Keh-Shih et al. (2006). "Fuzzy c-means clustering with spatial information for image segmentation". In: *Computerized medical imaging and graphics : the official journal of the Computerized Medical Imaging Society* 30.1, pp. 9–15. ISSN: 0895-6111. DOI: 10.1016/j.compmedimag.2005.10.001.

Cohen, D. (1972a). "Magnetoencephalography: detection of the brain's electrical activity with a superconducting magnetometer". In: *Science (New York, N.Y.)* 175.4022, pp. 664–666. ISSN: 0036-8075. DOI: 10.1126/science.175.4022.664.

Cohen, David (1972b). "Magnetoencephalography: detection of the brain's electrical activity with a superconducting magnetometer". In: *Science* 175.4022, pp. 664–666. ISSN: 0036-8075.

Collins, D. Louis et al. (1994). "Automatic 3D intersubject registration of MR volumetric data in standardized Talairach space". In: *Journal of computer assisted tomography* 18.2, pp. 192–205. ISSN: 0363-8715.

Cruccu, G. et al. (2008). "Recommendations for the clinical use of somatosensory-evoked potentials". In: *Clinical Neurophysiology* 119.8, pp. 1705–1719. ISSN: 1388-2457. DOI: 10.1016/j.clinph.2008.03.016. URL: https://www.sciencedirect.com/science/article/pii/S1388245708002046.

Cuartas Morales, Ernesto et al. (2019). "A Finite-Difference Solution for the EEG Forward Problem in Inhomogeneous Anisotropic Media". In: *Brain topography* 32.2, pp. 229–239. DOI: 10.1007/s10548-018-0683-2.

Darvas, F. et al. (2004). "Mapping human brain function with MEG and EEG: methods and validation". In: *NeuroImage* 23, S289–S299. ISSN: 1053-8119. DOI: 10.1016/j.neuroimage.2004.07.014. URL: https://www.sciencedirect.com/science/article/pii/S1053811904003799.

Di Pietro, Daniele and Alexandre Ern (2012). *Mathematical Aspects of Discontinuous Galerkin Methods*. Vol. 69. Springer. ISBN: 978-3-642-22979-4. DOI: 10.1007/978-3-642-22980-0.

Dmochowski, Jacek P. et al. (2011). "Optimized multi-electrode stimulation increases focality and intensity at target". In: *Journal of neural engineering* 8.4, p. 046011. ISSN: 1741-2552.

Edwards, Dylan J. et al. (2017). "Transcranial direct current stimulation and sports performance". In: *Frontiers in human neuroscience* 11, p. 243. ISSN: 1662-5161.

Engwer, Christian and Andreas Nüßing (2017). "Geometric reconstruction of implicitly defined surfaces and domains with topological guarantees". In: *ACM Transactions on Mathematical Software (TOMS)* 44.2, pp. 1–20.

Engwer, Christian et al. (2017). "A discontinuous Galerkin method to solve the EEG forward problem using the subtraction approach". In: *SIAM Journal on Scientific Computing* 39.1, B138–B164.

Epshteyn, Yekaterina and Béatrice Rivière (2007). "Estimation of penalty parameters for symmetric interior penalty Galerkin methods". In: *Journal of Computational and Applied Mathematics* 206.2, pp. 843–872. ISSN: 03770427. DOI: 10.1016/j.cam.2006.08.029.

Erdbrügger, Tim et al. (2023). "CutFEM forward modeling for EEG source analysis". In: *Frontiers in human neuroscience* 17. ISSN: 1662-5161.

Erdbrügger, Tim et al. (2024). "CutFEM–based MEG forward modeling improves source separability and sensitivity to quasi–radial sources: A somatosensory group study". In: *Human brain mapping* 45.11. DOI: 10.1002/hbm.26810.

Erik Burman and Peter Hansbo (2012). "Fictitious domain finite element methods using cut elements: II. A stabilized Nitsche method". In: *Applied Numerical Mathematics* 62.4, pp. 328–341. ISSN: 0168-9274. DOI: 10.1016/j.apnum.2011.01.008. URL: http://www.sciencedirect.com/science/article/pii/S0168927411000298.

Evans, Lawrence C. (2022). *Partial differential equations*. Vol. 19. American Mathematical Society. ISBN: 1470469421.

Fernández-Corazza, Mariano, Sergei Turovets, and Carlos Horacio Muravchik (2020). "Unification of optimal targeting methods in transcranial electrical stimulation". In: *NeuroImage* 209, p. 116403. ISSN: 1053-8119. DOI: 10.1016/j.neuroimage.2019.116403.

Ferree, T. C., K. J. Eriksen, and D. M. Tucker (2000). "Regional head tissue conductivity estimation for improved EEG analysis". In: *IEEE transactions on bio-medical engineering* 47.12, pp. 1584–1592. ISSN: 0018-9294. DOI: 10.1109/10.887939.

Fischl, Bruce (2012). "FreeSurfer". In: *NeuroImage* 62.2, pp. 774–781. ISSN: 1053-8119.

Fischl, Bruce and Anders M. Dale (2000). "Measuring the thickness of the human cerebral cortex from magnetic resonance images". In: *Proceedings of the National Academy of Sciences* 97.20, pp. 11050–11055. ISSN: 0027-8424. DOI: 10.1073/pnas.200033797.

Frank, Alexander (3/2022). "Sensitivity of Optimization in Transcranial Direct Current Stimulation to Electrode Modeling". PhD thesis. WWU Münster. URL: http://www.sci.utah.edu/~wolters/PaperWolters/2022/MasterFrank.pdf.

Gaser, Christian et al. (2022). "CAT–A computational anatomy toolbox for the analysis of structural MRI data". In: *biorxiv*, pp. 2022–06.

Gençer, Nevzat G. and Can E. Acar (2004). "Sensitivity of EEG and MEG measurements to tissue conductivity". In: *Physics in Medicine & Biology* 49.5, p. 701.

Goldenholz, Daniel M. et al. (2009). "Mapping the signal–to–noise–ratios of cortical sources in magnetoencephalography and electroencephalography". In: *Human brain mapping* 30.4, pp. 1077–1086.

Götz, Theresa et al. (2014). "Thalamocortical impulse propagation and information transfer in EEG and MEG". In: *Journal of clinical neurophysiology : official publication of the American Electroencephalographic Society* 31.3, pp. 253–260. DOI: 10.1097/WNP.0000000000000048.

Gramfort, Alexandre et al. (2010). "OpenMEEG: opensource software for quasistatic bioelectromagnetics". In: *Biomedical engineering online* 9, pp. 1–20.

— (2011). "Forward field computation with OpenMEEG". In: *Computational intelligence and neuroscience* 2011.

Gross, Sven and Arnold Reusken (2023). "Analysis of optimal preconditioners for CutFEM". In: *Numerical Linear Algebra with Applications* 30.5. ISSN: 1070-5325. DOI: 10.1002/nla.2486.

Hämäläinen, Matti et al. (1993). "Magnetoencephalography—theory, instrumentation, and applications to noninvasive studies of the working human brain". In: *Reviews of Modern Physics* 65.2, pp. 413–497. ISSN: 0034-6861. DOI: 10.1103/RevModPhys.65.413.

Hanrath, Anne (2019). *Finite element representation of the EEG forward problem with multipole expansion*. Dissertation, RWTH Aachen University, 2019.

Haueisen, J. et al. (2012). "Reconstruction of quasi-radial dipolar activity using three-component magnetic field measurements". In: *Clinical neurophysiology : official journal of the International Federation of Clinical Neurophysiology* 123.8, pp. 1581–1585. ISSN: 1388-2457. DOI: 10.1016/j.clinph.2011.12.020.

Hauk, Olaf (2004). "Keep it simple: a case for using classical minimum norm estimation in the analysis of EEG and MEG data". In: *NeuroImage* 21.4, pp. 1612–1621. ISSN: 1053-8119. DOI: 10.1016/j.neuroimage.2003.12.018.

He, Q., A. Rezaei, and S. Pursiainen (2020). "Zeffiro User Interface for Electromagnetic Brain Imaging: a GPU Accelerated FEM Tool for Forward and Inverse Computations in Matlab". In: *Neuroinformatics* 18.2, pp. 237–250. DOI: 10.1007/s12021-019-09436-9.

Herculano-Houzel, Suzana (2009). "The human brain in numbers: a linearly scaled-up primate brain". In: *Frontiers in human neuroscience*, p. 31. ISSN: 1662-5161.

Holm, Sture (1979). "A simple sequentially rejective multiple test procedure". In: *Scandinavian journal of statistics*, pp. 65–70. ISSN: 0303-6898.

Höltershinken, Malte B. et al. (2023). *The Localized Subtraction Approach For EEG and MEG Forward Modeling*. DOI: 10.48550/ARXIV.2302.12785.

Hoy, Kate E. et al. (2013). "Testing the limits: investigating the effect of tDCS dose on working memory enhancement in healthy controls". In: *Neuropsychologia* 51.9, pp. 1777–1784. ISSN: 0028-3932.

Hyvönen, Nuutti (2004). "Complete Electrode Model of Electrical Impedance Tomography: Approximation Properties and Characterization of Inclusions". In: *SIAM Journal on Applied Mathematics* 64.3, pp. 902–931. ISSN: 0036-1399. DOI: 10.1137/S0036139903423303.

Iwasaki, Masaki et al. (2005). "Detection of epileptiform activity by human interpreters: blinded comparison between electroencephalography and magnetoencephalography". In: *Epilepsia* 46.1, pp. 59–68. ISSN: 0013-9580.

Jenkinson, Mark et al. (2002). "Improved optimization for the robust and accurate linear registration and motion correction of brain images". In: *NeuroImage* 17.2, pp. 825–841. ISSN: 1053-8119.

Johnson, A. A. and T. E. Tezduyar (1999). "Advanced mesh generation and update methods for 3D flow simulations". In: *Computational Mechanics* 23.2, pp. 130–143. ISSN: 0178-7675. DOI: 10.1007/s004660050393.

Johnson, C. R. (1997). "Computational and numerical methods for bioelectric field problems". In: *Critical reviews in biomedical engineering* 25.1, pp. 1–81. ISSN: 0278-940X. DOI: 10.1615/critrevbiomedeng.v25.i1.10.

Justin K. Rice et al. (2013). "Subject position affects EEG magnitudes". In: *NeuroImage* 64, pp. 476–484. ISSN: 1053-8119. DOI: 10.1016/j.neuroimage.2012.09.041. URL: https://www.sciencedirect.com/science/article/pii/S1053811912009512.

Kaufmann, Elisabeth et al. (2021). "Acute effects of spaced cathodal transcranial direct current stimulation in drug resistant focal epilepsies". In: *Clinical neurophysiology : official journal of the International Federation of Clinical Neurophysiology* 132.7, pp. 1444–1451. ISSN: 1388-2457. DOI: 10.1016/j.clinph.2021.03.048.

Khan, Asad et al. (2019). "Constrained maximum intensity optimized multi-electrode tDCS targeting of human somatosensory network". In: *Annual International Conference of the*

IEEE Engineering in Medicine and Biology Society. IEEE Engineering in Medicine and Biology Society. Annual International Conference 2019, pp. 5894–5897. DOI: 10.1109/EMBC.2019.8857253.

Khan, Asad et al. (2022). "Individually optimized multi-channel tDCS for targeting somatosensory cortex". In: *Clinical Neurophysiology* 134, pp. 9–26. ISSN: 1388-2457.

Kirschstein, Timo and Rüdiger Köhling (2009). "What is the source of the EEG?" In: *Clinical EEG and neuroscience* 40.3, pp. 146–149. ISSN: 1550-0594.

Knake, S. et al. (2006). "The value of multichannel MEG and EEG in the presurgical evaluation of 70 epilepsy patients". In: *Epilepsy research* 69.1, pp. 80–86. ISSN: 0920-1211.

Kronberg, Greg et al. (2017). "Direct current stimulation modulates LTP and LTD: activity dependence and dendritic effects". In: *Brain stimulation* 10.1, pp. 51–58. ISSN: 1935-861X.

Kybic, Jan et al. (2005). "A common formalism for the integral formulations of the forward EEG problem". In: *IEEE transactions on medical imaging* 24.1, pp. 12–28. ISSN: 0278-0062. DOI: 10.1109/tmi.2004.837363.

Lanfer, Benjamin et al. (2012). "Influences of skull segmentation inaccuracies on EEG source analysis". In: *NeuroImage* 62.1, pp. 418–431. ISSN: 1053-8119.

Lantz, Göran et al. (2003). "Propagation of interictal epileptiform activity can lead to erroneous source localizations: a 128-channel EEG mapping study". In: *Journal of clinical Neurophysiology* 20.5, pp. 311–319.

Lefaucheur, Jean-Pascal et al. (2017). "Evidence-based guidelines on the therapeutic use of transcranial direct current stimulation (tDCS)". In: *Clinical Neurophysiology* 128.1, pp. 56–92. ISSN: 1388-2457.

Leonardi, Matilde and T. Bedirhan Ustun (2002). "The global burden of epilepsy". In: *Epilepsia* 43, pp. 21–25. ISSN: 0013-9580.

Lew, S. et al. (2009a). "Accuracy and run-time comparison for different potential approaches and iterative solvers in finite element method based EEG source analysis". In: *Applied Numerical Mathematics* 59.8, pp. 1970–1988. ISSN: 0168-9274. DOI: 10.1016/j.apnum.2009.02.006.

Lew, Seok et al. (2009b). "Accuracy and run-time comparison for different potential approaches and iterative solvers in finite element method based EEG source analysis". In: *Applied Numerical Mathematics* 59.8, pp. 1970–1988. ISSN: 0168-9274.

Li, Jing et al. (2007). "Effects of holes on EEG forward solutions using a realistic geometry head model". In: *Journal of neural engineering* 4.3, p. 197. ISSN: 1741-2552.

Liu, Z. et al. (2019). "MRI Abnormalities Predominate in the Bottom Part of the Sulcus with Type II Focal Cortical Dysplasia: A Quantitative Study". In: *AJNR. American journal of neuroradiology* 40.1, pp. 184–190. DOI: 10.3174/ajnr.A5919.

Mahjoory, Keyvan et al. (2017). "Consistency of EEG source localization and connectivity estimates". In: *NeuroImage* 152, pp. 590–601. ISSN: 1053-8119. DOI: 10.1016/j.neuroimage.2017.02.076.

Makarov, Sergey N. et al. (2020). "Boundary element fast multipole method for enhanced modeling of neurophysiological recordings". In: *IEEE transactions on biomedical engineering* 68.1, pp. 308–318.

Medani, Takfarinas et al. (2023). "Brainstorm-DUNEuro: An integrated and user-friendly Finite Element Method for modeling electromagnetic brain activity". In: *NeuroImage* 267, p. 119851. ISSN: 1053-8119. DOI: 10.1016/j.neuroimage.2022.119851.

Michel, Christoph M. and Micah M. Murray (2012). "Towards the utilization of EEG as a brain imaging tool". In: *NeuroImage* 61.2, pp. 371–385. ISSN: 1053-8119. DOI: 10.1016/j.neuroimage.2011.12.039.

Monte-Silva, Katia et al. (2013). "Induction of late LTP-like plasticity in the human motor cortex by repeated non-invasive brain stimulation". In: *Brain stimulation* 6.3, pp. 424–432. ISSN: 1935-861X.

Montes-Restrepo, Victoria et al. (2014). "Influence of skull modeling approaches on EEG source localization". In: *Brain topography* 27, pp. 95–111.

Mosher, J. C., R. M. Leahy, and P. S. Lewis (1999a). "EEG and MEG: forward solutions for inverse methods". In: *IEEE transactions on bio-medical engineering* 46.3, pp. 245–259. ISSN: 0018-9294. DOI: 10.1109/10.748978.

Mosher, John C., Richard M. Leahy, and Paul S. Lewis (1999b). "EEG and MEG: forward solutions for inverse methods". In: *IEEE transactions on biomedical engineering* 46.3, pp. 245–259.

Munck, J. C. de and M. J. Peters (1993). "A fast method to compute the potential in the multisphere model". In: *IEEE transactions on bio-medical engineering* 40.11, pp. 1166–1174. ISSN: 0018-9294. DOI: 10.1109/10.245635.

Munck, J. C. de, Maria J. Peters, et al. (1993). "A fast method to compute the potential in the multisphere model". In: *IEEE Trans. Biomed. Eng* 40.11, pp. 1166–1174.

Munck, J. C. de, Carsten H. Wolters, and Maureen Clerc (2012). "EEG and MEG: forward modeling". In: *Handbook of neural activity measurement* 19, pp. 192–248.

Munck, Jan C. de, Bob W. van Dijk, and HENK Spekreijse (1988). "Mathematical dipoles are adequate to describe realistic generators of human brain activity". In: *IEEE transactions on biomedical engineering* 35.11, pp. 960–966.

Murakami, Shingo and Yoshio Okada (2006a). "Contributions of principal neocortical neurons to magnetoencephalography and electroencephalography signals". In: *The Journal of physiology* 575.3, pp. 925–936.

— (2006b). "Contributions of principal neocortical neurons to magnetoencephalography and electroencephalography signals". In: *The Journal of physiology* 575.3, pp. 925–936.

Nakamura, Akinori et al. (1998). "Somatosensory homunculus as drawn by MEG". In: *NeuroImage* 7.4, pp. 377–386. ISSN: 1053-8119.

Nédélec, Jean-Claude (2001). *Acoustic and electromagnetic equations: integral representations for harmonic problems*. Vol. 144. Springer.

Neugebauer, Frank et al. (2022). "Validating EEG, MEG and Combined MEG and EEG Beamforming for an Estimation of the Epileptogenic Zone in Focal Cortical Dysplasia". In: *Brain Sciences* 12.1, p. 114.

Nielsen, Jesper D. et al. (2018). "Automatic skull segmentation from MR images for realistic volume conductor models of the head: Assessment of the state-of-the-art". In: *NeuroImage* 174, pp. 587–598. ISSN: 1053-8119.

Nitsche, Joachim (1971). *Über ein Variationsprinzip zur Lösung von Dirichlet-Problemen bei Verwendung von Teilräumen, die keinen Randbedingungen unterworfen sind*. DOI: 10.1007/BF02995904.

Nomenclature, Standard Electrode Position (1991). "American electroencephalographic society guidelines for". In: *Journal of clinical Neurophysiology* 8.2, pp. 200–202.

Nüßing, Andreas (2018). "Fitted and unfitted finite element methods for solving the EEG forward problem". PhD thesis. Universität Münster.

Nüßing, Andreas et al. (2016). "The unfitted discontinuous Galerkin method for solving the EEG forward problem". In: *IEEE transactions on biomedical engineering* 63.12, pp. 2564–2575.

Oostenveld, R. and P. Praamstra (2001). "The five percent electrode system for high-resolution EEG and ERP measurements". In: *Clinical neurophysiology : official journal of the International Federation of Clinical Neurophysiology* 112.4, pp. 713–719. ISSN: 1388-2457. DOI: 10.1016/s1388-2457(00)00527-7.

Oostenveld, Robert et al. (2011). "FieldTrip: open source software for advanced analysis of MEG, EEG, and invasive electrophysiological data". In: *Computational intelligence and neuroscience* 2011.

Otsu, Nobuyuki (1979). "A threshold selection method from gray-level histograms". In: *IEEE transactions on systems, man, and cybernetics* 9.1, pp. 62–66. ISSN: 0018-9472.

Palmini, Andre (2006). "The concept of the epileptogenic zone: a modern look at Penfield and Jasper's views on the role of interictal spikes". In: *Epileptic disorders* 8, S10–S15. ISSN: 1294-9361.

Perona, Pietro and Jitendra Malik (1990). "Scale-space and edge detection using anisotropic diffusion". In: *IEEE Transactions on pattern analysis and machine intelligence* 12.7, pp. 629–639. ISSN: 0162-8828.

Piastra, Maria Carla et al. (2018). "The discontinuous Galerkin finite element method for solving the MEG and the combined MEG/EEG forward problem". In: *Frontiers in Neuroscience* 12, p. 30. ISSN: 1662-453X.

Piastra, Maria Carla et al. (2021). "A comprehensive study on electroencephalography and magnetoencephalography sensitivity to cortical and subcortical sources". In: *Human brain mapping* 42.4, pp. 978–992.

Preuß, Janosch (2018). "Higher order unfitted isoparametric space-time FEM on moving domains". In: *Master's thesis, University of Gottingen*.

Puce, Aina and Matti S. Hämäläinen (2017). "A Review of Issues Related to Data Acquisition and Analysis in EEG/MEG Studies". In: *Brain Sciences* 7.6. DOI: 10.3390/brainsci7060058.

R Core Team, R. (2013). "R: A language and environment for statistical computing". In.

Radecke, Jan-Ole et al. (2023). "Normative tDCS over V5 and FEF reveals practice-induced modulation of extraretinal smooth pursuit mechanisms, but no specific stimulation effect". In: *Scientific reports* 13.1, p. 21380. DOI: 10.1038/s41598-023-48313-z.

Rahman, Asif et al. (2013). "Cellular effects of acute direct current stimulation: somatic and synaptic terminal effects". In: *The Journal of physiology* 591.10, pp. 2563–2578.

Rampp, Stefan et al. (2019). "Magnetoencephalography for epileptic focus localization in a series of 1000 cases". In: *Brain* 142.10, pp. 3059–3071.

Rezaei, Atena et al. (2021). "Reconstructing subcortical and cortical somatosensory activity via the RAMUS inverse source analysis technique using median nerve SEP data". In: *NeuroImage* 245, p. 118726. ISSN: 1053-8119. DOI: 10.1016/j.neuroimage.2021.118726.

Rolls, Edmund T. et al. (2020). "Automated anatomical labelling atlas 3". In: *NeuroImage* 206, p. 116189. ISSN: 1053-8119. DOI: 10.1016/j.neuroimage.2019.116189.

Rosenow, F. and H. Lüders (2001). "Presurgical evaluation of epilepsy". In: *Brain : a journal of neurology* 124.Pt 9, pp. 1683–1700. ISSN: 0006-8950. DOI: 10.1093/brain/124.9.1683.

Rush, S. and D. A. Driscoll (1969). "EEG electrode sensitivity–an application of reciprocity". In: *IEEE transactions on bio-medical engineering* 16.1, pp. 15–22. ISSN: 0018-9294. DOI: 10.1109/tbme.1969.4502598.

Salvetti, Arthur and Bogdan M. Wilamowski (2008). "A brain-computer interface for recognizing brain activity". In: *2008 Conference on Human System Interactions*, pp. 714–719.

Sarnthein, Johannes et al. (2022). "Evaluation of a new cortical strip electrode for intraoperative somatosensory monitoring during perirolandic brain surgery". In: *Clinical Neurophysiology* 142, pp. 44–51. ISSN: 1388-2457. DOI: 10.1016/j.clinph.2022.07.497. URL: https://www.sciencedirect.com/science/article/pii/S1388245722008240.

Sarvas, Jukka (1987). "Basic mathematical and electromagnetic concepts of the biomagnetic inverse problem". In: *Physics in Medicine & Biology* 32.1, p. 11.

Saturnino, Guilherme B. et al. (2019). "SimNIBS 2.1: a comprehensive pipeline for individualized electric field modelling for transcranial brain stimulation". In: *Brain and human body modeling: computational human modeling at EMBC 2018*, pp. 3–25.

Scherg, M. and H. Buchner (1993). "Somatosensory evoked potentials and magnetic fields: separation of multiple source activities". In: *Physiological measurement* 14 Suppl 4A, A35–9. ISSN: 0967-3334. DOI: 10.1088/0967-3334/14/4a/006.

Schrader, S. et al. (2020). "A novel method for calibrating head models to account for variability in conductivity and its evaluation in a sphere model". In: *Physics in Medicine and Biology* 65.24, p. 245043. DOI: 10.1088/1361-6560/abc5aa.

Schrader, Sophie (2022). *Calibrating Finite Element Head Models Using EEG/MEG to Account for Variability in Conductivity*. Westfälische Wilhelms-Universität Münster.

Schrader, Sophie et al. (2021). "DUNEuro—A software toolbox for forward modeling in bioelectromagnetism". In: *PloS one* 16.6, e0252431.

Shewchuk, Jonathan (2002). "What is a good linear finite element? interpolation, conditioning, anisotropy, and quality measures (preprint)". In: *University of California at Berkeley* 2002.

Spencer, David C. et al. (2016). "Circadian and ultradian patterns of epileptiform discharges differ by seizure-onset location during long-term ambulatory intracranial monitoring". In: *Epilepsia* 57.9, pp. 1495–1502. ISSN: 0013-9580. DOI: 10.1111/epi.13455.

Sticko, Simon (2018). *High Order Cut Finite Element Methods for Wave Equations*. Vol. 1656. Digital Comprehensive Summaries of Uppsala Dissertations from the Faculty of Science and Technology. Uppsala: Acta Universitatis Upsaliensis. ISBN: 978-91-513-0300-0.

Sudbrack-Oliveira, Pedro et al. (2021). "Transcranial direct current stimulation (tDCS) in the management of epilepsy: A systematic review". In: *Seizure* 86, pp. 85–95. DOI: 10.1016/j.seizure.2021.01.020.

Tassi, Laura et al. (2010). "Type I focal cortical dysplasia: surgical outcome is related to histopathology". In: *Epileptic disorders : international epilepsy journal with videotape* 12.3, pp. 181–191. ISSN: 1294-9361. DOI: 10.1684/epd.2010.0327.

Thair, Hayley et al. (2017). "Transcranial direct current stimulation (tDCS): a beginner's guide for design and implementation". In: *Frontiers in Neuroscience* 11, p. 641. ISSN: 1662-453X.

Thielscher, Axel, Andre Antunes, and Guilherme B. Saturnino (2015). "Field modeling for transcranial magnetic stimulation: A useful tool to understand the physiological effects of TMS?" In: *Annual International Conference of the IEEE Engineering in Medicine and Biology Society. IEEE Engineering in Medicine and Biology Society. Annual International Conference* 2015, pp. 222–225. DOI: 10.1109/EMBC.2015.7318340.

Thio, Brandon J. and Warren M. Grill (2023). "Relative contributions of different neural sources to the EEG". In: *NeuroImage* 275, p. 120179. ISSN: 1053-8119.

Tikhonov, Andreĭ Nikolaevich and VIAK Arsenin (1977). "Solutions of ill-posed problems". In: *(No Title)*.

Vallaghé, Sylvain and Théodore Papadopoulo (2010). "A trilinear immersed finite element method for solving the EEG forward problem". In: *SIAM J. Sci. Comp., accepted for publication*.

Vallaghé, Sylvain, Théodore Papadopoulo, and Maureen Clerc (2009). "The adjoint method for general EEG and MEG sensor-based lead field equations". In: *Physics in Medicine and Biology* 54.1, pp. 135–147. DOI: 10.1088/0031-9155/54/1/009.

van den Broek, Sebastianus Petrus et al. (1998). "Volume conduction effects in EEG and MEG". In: *Electroencephalography and clinical Neurophysiology* 106.6, pp. 522–534.

Vanrumste, Bart et al. (2000). "Dipole location errors in electroencephalogram source analysis due to volume conductor model errors". In: *Medical and Biological Engineering and Computing* 38, pp. 528–534. ISSN: 0140-0118.

Veersema, Tim J. et al. (2019). "Long-term seizure outcome after epilepsy surgery in patients with mild malformation of cortical development and focal cortical dysplasia". In: *Epilepsia open* 4.1, pp. 170–175. ISSN: 2470-9239. DOI: 10.1002/epi4.12289.

Vorwerk, Johannes (2016). *New finite element methods to solve the EEG/MEG forward problem*. Westfälische Wilhelms-Universität Münster.

Vorwerk, Johannes et al. (2012). "Comparison of boundary element and finite element approaches to the EEG forward problem". In: *Biomedical Engineering/Biomedizinische Technik* 57.SI-1-Track-O, pp. 795–798. ISSN: 1862-278X.

Vorwerk, Johannes et al. (2014). "A guideline for head volume conductor modeling in EEG and MEG". In: *NeuroImage* 100, pp. 590–607. ISSN: 1053-8119.

Vorwerk, Johannes et al. (2019). "The multipole approach for EEG forward modeling using the finite element method". In: *NeuroImage* 201, p. 116039. ISSN: 1053-8119.

Wagner, S. et al. (2016). "Using reciprocity for relating the simulation of transcranial current stimulation to the EEG forward problem". In: *NeuroImage* 140, pp. 163–173. ISSN: 1053-8119. DOI: 10.1016/j.neuroimage.2016.04.005.

Wang, Li et al. (2011). "Automatic segmentation of neonatal images using convex optimization and coupled level sets". In: *NeuroImage* 58.3, pp. 805–817. ISSN: 1053-8119. DOI: 10.1016/j.neuroimage.2011.06.064.

Wang, Yun et al. (2018). "A simplified morphological classification scheme for pyramidal cells in six layers of primary somatosensory cortex of juvenile rats". In: *IBRO reports* 5, pp. 74–90. ISSN: 2451-8301.

Wehner, Tim et al. (2021). "Factors influencing the detection of treatable epileptogenic lesions on MRI. A randomized prospective study". In: *Neurological research and practice* 3.1, p. 41. DOI: 10.1186/s42466-021-00142-z.

Whitaker, Ross T. (2000). "Reducing aliasing artifacts in iso-surfaces of binary volumes". In: *Proceedings of the 2000 IEEE symposium on Volume visualization*, pp. 23–32.

Windhoff, Mirko, Alexander Opitz, and Axel Thielscher (2013). "Electric field calculations in brain stimulation based on finite elements: an optimized processing pipeline for the

generation and usage of accurate individual head models". In: *Human brain mapping* 34.4, pp. 923–935. DOI: 10.1002/hbm.21479.

Wolters, C. H. et al. (2002). "A parallel algebraic multigrid solver for finite element method based source localization in the human brain". In: *Computing and Visualization in Science* 5.3, pp. 165–177. ISSN: 14329360. DOI: 10.1007/s00791-002-0098-0.

Wolters, Carsten, Lars Grasedyck, and Wolfgang Hackbusch (2004). "Efficient Computation of lead field bases and influence matrix for the FEM-based EEG and MEG inverse problem". In: *Inverse Problems* 20, pp. 1099–1116. DOI: 10.1088/0266-5611/20/4/007.

Wolters, Carsten H. et al. (2007). "Geometry-adapted hexahedral meshes improve accuracy of finite-element-method-based EEG source analysis". In: *IEEE transactions on biomedical engineering* 54.8, pp. 1446–1453.

Wolters, Carsten H. et al. (2008). "Numerical mathematics of the subtraction method for the modeling of a current dipole in EEG source reconstruction using finite element head models". In: *SIAM Journal on Scientific Computing* 30.1, pp. 24–45.

Wolters, Carsten Hermann et al. (1999). "Comparing regularized and non-regularized nonlinear dipole fit methods: a study in a simulated sulcus structure". In: *Brain topography* 12, pp. 3–18.

Woods, A. J. et al. (2016). "A technical guide to tDCS, and related non-invasive brain stimulation tools". In: *Clinical neurophysiology : official journal of the International Federation of Clinical Neurophysiology* 127.2, pp. 1031–1048. ISSN: 1388-2457. DOI: 10.1016/j.clinph.2015.11.012.

Yang, Dalin, Yong-Il Shin, and Keum-Shik Hong (2021). "Systemic Review on Transcranial Electrical Stimulation Parameters and EEG/fNIRS Features for Brain Diseases". In: *Frontiers in Neuroscience* 15, p. 629323. ISSN: 1662-453X. DOI: 10.3389/fnins.2021.629323.

Yoo, Terry S. et al. (2002). "Engineering and algorithm design for an image processing API: a technical report on ITK-the insight toolkit". In: *Medicine Meets Virtual Reality 02/10*. IOS press, pp. 586–592.

Akademischer Lebenslauf

Name:	Tim-René Erdbrügger
geboren am:	am 30.03.1994 in Bielefeld
Staatsangehörigkeit:	deutsch
Hochschulreife (Abitur):	am 03.07.2013 in Bünde
Studium:	Volkswirtschaftslehre 01.10.2013 bis 30.09.2014 an der Universität Münster
Studium:	Mathematik 01.10.2014 bis 31.03.2021 an der Universität Münster
Abschlüsse:	Bachelor of Science: 09.10.2017 Master of Science: 02.03.2021
Promotion:	seit 01.04.2021, Institut für Angewandte Mathematik, bei Prof. Dr. Christian Engwer und Prof. Dr. Carsten H. Wolters (vom Fachbereich Medizin)
Beschäftigung:	Wiss. Mitarbeiter am Institut für Biomagnetismus und Biosignalanalyse, UKM Münster 01.04.2021 - 30.09.2024